ON GRAVITATIONAL WAVE MODELING: NUMERICAL RELATIVITY DATA ANALYSIS, THE EXCITATION OF KERR QUASINORMAL MODES, AND THE UNSUPERVISED MACHINE LEARNING OF WAVEFORM MORPHOLOGY

A Thesis
Presented to
The Academic Faculty

by

Lionel London

In Partial Fulfillment
of the Requirements for the Degree
Doctor of Philosophy in the
School of Physics

Georgia Institute of Technology
August 2015

ON GRAVITATIONAL WAVE MODELING: NUMERICAL RELATIVITY DATA ANALYSIS, THE EXCITATION OF KERR QUASINORMAL MODES, AND THE UNSUPERVISED MACHINE LEARNING OF WAVEFORM MORPHOLOGY

Approved by:

Tamara Bogdanovic, Committee Chair
School of Physics
Georgia Institute of Technology

Deirdre Shoemaker, Advisor
School of Physics
Georgia Institute of Technology

Pablo Laguna
School of Physics
Georgia Institute of Technology

Nepomuk Otte
School of Physics
Georgia Institute of Technology

Julia Kubanek
School of Biology and School of Chemistry & Biochemistry
Georgia Institute of Technology

Date Approved: TBD

To science, bravery, angst, humility and resilience.

ACKNOWLEDGEMENTS

The existence of this thesis has been supported, indispensably, by:

Deborah and Lionelle London

Deirdre Shoemaker and Pablo Laguna

Julia Kubanek and Paul Goldbart

Contents

List of Tables

List of Figures

PREFACE

The expectation that light waves are the only way to gather information about the distant universe dominated scientific thought, without serious alternative, until Einstein's 1916 proposal that gravitational waves are generated by the dynamics of massive objects [12]. Now, after nearly a century of speculation, theoretical development, observational support, and finally, tremendous experimental preparation, there are good reasons to believe that we will soon directly detect gravitational waves. Perhaps the most prominent of these good reasons is the ongoing increase in sensitivity of the Laser Interferometer Gravitational Wave Observatory (LIGO), which will be able to detect gravitational wave sources such as colliding neutron star binaries, neutron star black hole binaries and, the focus of this thesis, black hole binarys.

With expectation for detection increasingly mounting, the community of gravitational wave physicists is eager to inform basic astronomy questions: *What do likely signals look like? Where is the sky location of the signal's source? What class of objects does the signal come from? What are the system's physical parameters, and can we learn about how those parameters change in time?* Concurrently, pinned to each of these observational questions, are requisite theoretical ones: *Do we understand the physics of likely sources well enough to generate ideal, template signals? What are the underlying physical principles that determine who much information is in a gravitational wave signal? Is it possible to test extensions of current general relativistic theory with detected signals? Conversely, is it possible to identify new physics, given what we already accept to be true?*

Likely, the most practical questions reside at the interface between gravitational wave theory and experiment: *What are the most effective formulaic perspectives for constructing template signals? What is the maximum information that may be learned from gravitational wave signals in post-detection analyses? And, in the case of parameter estimation, is it possible to generate template signals in a manner that is both physically accurate, and very*

computationally efficient?

There are surely more questions being asked. However, it is qualitatively accurate that most data analysis questions depend significantly on our ability to effectively model potential gravitational wave signals. It is within this central context that the author's thesis work on *gravitational wave modeling* has emerged.

Gravitational Wave Modeling. Gravitational wave modeling is motivated by the fact that *prior* knowledge of signal morphology empowers us to detect gravitational waves, even when experimental noise is much much larger than the observed signal amplitude (Section 3.2.2). Therefore, the broad goal of gravitational wave modeling is to characterize, either analytically, or semi–analytically, the spatiotemporal morphology of gravitational radiation for different physical systems. The larger utility of such models is that they enable:

1. The ability to construct maps between waveform morphology and physical quantities that constrain the structure and dynamics of the waveform's source (*e.g.* the final mass and spin of a black hole resulting from the merger of two compact objects).

2. Our ability to determine which class of physical systems a gravitational wave signal is likely to belong.

The purpose of this thesis is to summarize the author's initial contributions to the above topics. Central focus will be placed on the modeling of gravitational waves from binary black hole systems.

SUMMARY

Part (I) establishes a basic foundation in General Relativity and gravitational waves. Chapter (1) gives a brief introduction to the basic concepts of General Relativity that lead to Einstein's equations and consequently, to gravitational waves. Chapter (2) expands upon gravitational wave theory by narrowing our focus to the gravitational radiation of compact object coalescence. Specifically, Section (2.1) discusses the interface between Newtonian gravity and General Relativity in the regime where the binary's constituents are very far apart and moving slowly. Section (2.2) expands upon this discussion by introducing Post-Newtonian theory and its description of gravitational wave *inspiral*. Section (2.3) picks up in the strong field gravity regime of *merger*, where the Post-Newtonian approximations fail. Here we review the role of Numerical Relativity in evaluating Einstein's equations in non perturbative regimes, and establish its very significant but limited role in effort to detect gravitational radiation from astrophysical sources. In Section (2.4) we briefly introduce the final pertutbative regime of compact object coalescence: where there were two objects there is now one, remnant objects whose gravitational radiation *rings down* like struck bell.

Part (II) describes the interface between Part (I)'s gravitational wave thoery, and current efforts to detect astrophysical gravitational radiation. Chapter (3) introduces the author's applied programming interface for the post analysis of Numerical Relativity simulation, and overviews its role in Georgia Tech's Numerical-Relativity-Data-Analysis activities. Chapter (4) builds upon prior discussions of Numerical Relativity and its interface with experiment to motivate gravitational wave modeling. Here, we will define precisely what we mean by "modeling", and give two pertinent examples.

With a sufficient foundation in place, Part (III) iterates through this thesis' core results. Chapter (5) presents on the author's contributions to the modeling of black hole Quasi-Normal Modes (QNMs), whereby a close interface between Numerical Relativity and

black hole black hole perturbation theory enabled the first robust phenomenological models for QNM excitement, as well as the first systematic analysis of QNM overtones, and the first extraction of evidence for non-linear QNM resulting from binary black hole mergers. This work is also the first to propose that the direction of black hole recoil may be determined observationally through detection of more than one QNM. Chapter (6) highlights the need for robust models of gravitational waves from precessing binaries (*i.e.* "precessing templates"). Examples are given in therms of the author's contribution to reference [13]. Chapter (7) briefly discusses ongoing work, of potentially high impact, regarding the author's development of an unsupervised machine learning scheme at the interface of Numerical Relativity and gravitational wave modeling.

Finally, Chapter (8) offers both a brief summary of the previous chapters, and a short discussion of the author's future directions.

LIST OF CONTRIBUTIONS

1. **Lionel London**, James Healy, Deirdre Shoemaker, "Modeling Ringdown: Beyond the Fundamental Quasi-Normal Modes," Phys. Rev. D 90, 124032 (2014).

2. The LIGO Scientific Collaboration, the Virgo Collaboration, the NINJA-2 Collaboration, "The NINJA-2 project: Detecting and characterizing gravitational waveforms modelled using numerical binary black hole simulations," Class. Quantum Grav. 31 115004, 2014.

3. Ian Hinder, Alessandra Buonanno, Michael Boyle, ..., **Lionel London**, *et. al.*, "Error-analysis and comparison to analytical models of numerical waveforms produced by the NRAR Collaboration," Class. Quantum Grav. 31 (2014) 025012.

4. R. O'Shaughnessy, **L. London**, J. Healy, D. Shoemaker, "Precession during merger 1: Strong polarization changes are observationally accessible features of strong-field gravity during binary black hole merger," Physical Review D, vol. 87, 044038, 2012.

5. R. O'Shaughnessy, J. Healy, **L. London**, Z. Meeks, D. Shoemaker, "Is J enough? Comparison of gravitational waves emitted along the total angular momentum direction with other preferred orientations," Physical Review D, vol. 85, Issue 8, 2012.

6. P Ajith, Michael Boyle, Duncan A Brown, Bernd Bruegmann, Luisa T Buchman, Laura Cadonati, Manuela Campanelli, Tony Chu, Zachariah B Etienne, Stephen Fairhurst, Mark Hannam, James Healy1, Ian Hinder, Sascha Husa, Lawrence E Kidder, Badri Krishnan, Pablo Laguna, Yuk Tung Liu, **Lionel London**, et al, "The NINJA-2 catalog of hybrid post-Newtonian/numerical-relativity waveforms for non-precessing black-hole binaries," Classical and Quantum Gravity vol. 29, 124001, 2012.

7. S. Fischetti, J. Healy, L. Cadonati, **L. London**, S. Mohapatra and D. Shoemaker, "Exploring Use of Numerical Relativity Waveforms in Burst Analysis of Precessing Black Hole Mergers," Physical Review D vol. 83, 044019, 2011.

8. J. Clark, L. Cadonati, J. Healy, S. Heng, J. Logue, N. Mangini, **L. London**, L. Pekowsky, D. Shoemaker, "Investigating Binary Black Hole Mergers with Principal Component Analysis," Proceedings of 3rd Session of the Sant Cugat Forum on Astrophysics, 2014.

ON GRAVITATIONAL WAVE MODELING: NUMERICAL RELATIVITY DATA ANALYSIS, THE EXCITATION OF KERR QUASINORMAL MODES, AND THE UNSUPERVISED MACHINE LEARNING OF WAVEFORM MORPHOLOGY

PART I

Preliminaries

by

Lionel London

Chapter I

GRAVITY AND GRAVITATIONAL WAVES

In this introductory chapter we will review this thesis' core maths and physics topics. Section (1.1) gives a brief conceptual and mathematical overview of General Relativity, and introduces the fundamental physics concepts that underpin the results of this thesis. Section (1.2) briefly examines the theory of gravitational waves, and bears particular attention to gravitational wave polarization and its relevance for gravitational wave detection.

While this chapter does not intend to give a linear exposition of General Relativity that culminates in gravitational wave theory, one may find such an exposition in reference [14]. Instead, we will attempt to conceptually motivate gravitational wave theory in parallel with the relevant mathematical principles. In other words, an attempt will be made to construct the fundamental ideas succinctly and without assuming that the reader is already inducted. We begin by reviewing central concepts of relativity, and then quickly slanting towards the topic of gravitational waves.

1.1 General Relativity

Space & Time. Of General Relativity's central concepts, the notion of space-time is perhaps the most foundational. But more than a simple concatenation of our three spatial dimensions, $\Delta x^a = (\Delta x^{(1)}, \Delta x^{(2)}, \Delta x^{(3)}) = (\Delta x, \Delta y, \Delta z)$, with time, $\Delta x^{(0)} = c\Delta t$, to specify a point within a smooth 4 dimensional space, $\Delta x^\mu = (\Delta x^{(0)}, \Delta x^{(1)}, \Delta x^{(2)}, \Delta x^{(2)})$, the marriage of space and time stems from the notion of *invariant* observables – quantities whose measured values are independent of the observer's motion. At the level of Special Relativity, the invariance of the speed of light, c, when measured by different, non-accelerating[1] (*i.e.*

[1]Specifically: no relative acceleration between observers.

inertial) observers demands the invariance of the space-time interval

$$\begin{aligned} c^2\Delta s^2 &= -(c\Delta x^{(0)})^2 + (\Delta x^{(1)})^2 + (\Delta x^{(1)})^2 + (\Delta x^{(3)})^2 \\ &= \eta_{\alpha\beta}\, x^\alpha\, x^\beta \ . \end{aligned} \tag{1}$$

Here, in the second line, repeated indeces represent sums (*i.e.* contractions), and $\eta_{\alpha\beta}$, the flat-space *metric*, encapsulates the prefactors, 1 and -1, in the first line[2].

Curvature and Gravity. Equation (1)'s limitation is that it is not realistic: the conceptual constraint that observers are not accelerating is a *special* rather than *general* view of relativity.

Aside on the Equivalence Principle. General observers, from telecommunication satellites to gravitational wave detectors, not only accelerate, but are also unable to distinguish between uniform acceleration, such as that due to the acceleration of a jet engine, and the force of gravity. This is due to the subtly peculiar fact that all macroscopic objects within a gravitational field, that have the same initial velocity, follow identical trajectories (Not considering air resistance), regardless of composition (*e.g.* mass, charge, spin, particle type, etc.).

Importantly, the generalization of observers can be made mathematically tractable: In much the same way that surface of the Earth is locally flat, any smooth non-uniform gravitational field is locally uniform, with the related gravitational acceleration taking on a value that is "locally" constant. As a consequence, observational frames that are free falling in the locally constant field are inertial, and the framework of Special Relativity applies. Put another way, the constancy of Equation (1)'s prefactors means that $\eta_{\alpha\beta}$ describes a flat geometry in which parallel space-time trajectories always remain intuitively straight, regardless of the size of Δs. However, in General Relativity, this property of *parallelism* only holds

[2]For those who are interested in keeping up with the index notion, it may be helpful to note that $\eta^{\mu\nu}V_\mu = V^\nu$, and $\eta^{\mu\nu}\eta_{\alpha\beta} = \eta^{\mu\nu}\eta_{\mu\beta} = \mathrm{diag}(1,1,1,1)$. It may also be useful to note that information that travels at c is described by $\Delta s = 0$

infinitesimally, with Δs^2 becoming $\mathrm{d}s^2$, and where

$$\mathrm{d}s^2 \;=\; g_{\alpha\beta}(x)\, x^\alpha\, x^\beta \;. \quad [\text{with c=1}] \tag{2}$$

Here, $g_{\alpha\beta}$ is the general spate-time metric, and just as in Special Relativity, the spacetime interval, $\mathrm{d}s$, is a central physical observable: *the distance along a rod of two nearby points is* $|\mathrm{d}s|$*, while the time elapsed on clock that experiences two nearly simultaneous events is*[3] $|-\mathrm{d}s|$.

At this point, in order to properly handle the mathematics, one must invoke Reimannian geometry, with it's Connection, $\Gamma^\rho_{\mu\nu}$ (which depends uniquely on $g_{\mu\nu}$ and its first derivatives) as well as the Reimann tensor, $R^\rho{}_{\sigma\mu\nu}$ (which depends on $g_{\mu\nu}$ and its second derivatives[4]). For example, the trajectory of free falling particles is locally straight, but must generally conform to the geodesic equation, $\frac{d^2x^\alpha}{d\lambda} + \Gamma^\alpha_{\beta\gamma}\frac{dx^\beta}{d\lambda}\frac{dx^\gamma}{d\lambda} \;=\; 0$. Moreover, $R^\rho{}_{\sigma\mu\nu}$, and in particular, its contractions ($R_{\mu\nu} = R^\lambda{}_{\mu\lambda\nu}$ and $R = g^{\mu\nu}R_{\mu\nu}$), encapsulate the *curvature* of space-time. Of particular importance is the relative acceleration, A^μ, between two free falling particles that are separated by S^σ, and move with velocities[5] U^ν and U'^ν

$$A^\mu = R^\mu{}_{\nu\rho\sigma}U^\nu U^\rho S^\sigma \;. \tag{3}$$

Roughly put, Equation (3) generalizes Newton's force–free condition $\partial_t^2\vec{x} = 0$ by describing the nontrivial *forcing* effect of space-time curvature.

Gravitation. On one hand, the concept of local flatness and global curvature enables us to translate our flat space-time physical laws, into their curved space-time generalizations: *Given a physical law in an inertial reference frame, write down its Reimannian tonsorial form, and then verify that the generalized law remains true in curved space-time*[6]. On the other hand, the equivalence principle allows us to identify gravitational fields with space-time geometry: *locally,* $g_{\mu\nu}$ *can be thought of as depending on either* x^α*, or some*

[3]This is consistent with the sign convention used in Equation (1).

[4]Importantly, $R^\rho_{\sigma\mu\nu}$ and $\Gamma^\rho_{\mu\nu}$ are nonlinear objects on $g_{\mu\nu}$, meaning that they depend on products of $g_{\mu\nu}$ and its derivatives.

[5]In Equation (3) information about U'^ν contained within $R^\mu_{\nu\rho\sigma}$.

[6]There are many adjacent ways of going about this, such as the principle of least action, and the spin -2 gauge theory approach

gravitational potential $\phi(x)$. It is by unifying these ideas that General Relativity renders the connection between space-time geometry, and the dynamics of matter and energy. In particular, if we consider Newton's gravitational law for the gravitational potential,

$$\nabla^2\phi \;=\; 4\pi G\rho\,, \tag{4}$$

(where ϕ is the gravitational field potential, G is the gravitational constant and ρ is density of mass), then the above program leads to the conclusion that

$$R_{\mu\nu} - \frac{1}{2}Rg_{\mu\nu} = 8\pi G T_{\mu\nu}\,. \quad \text{[Einstein's equations]} \tag{5}$$

We may first note that, just as Equation (4) enables us to solve for ϕ (and thereby the force of gravity) under problem specific boundary conditions, Equation (5) enables us to solve for the metric, $g_{\mu\nu}$.

An Aside on Black Holes. It is common to imagine that an observer in one region of space may communicate with an observer in another. More generally, it might appear from our day to day experience that an object in one region may be free, given enough effort, to move to any other region of space. However, according to Equation (5), this is not general true. In particular, there are solutions of Equation (5) that have closed surfaces of space through which information may enter, but not exit. These closed surfaces are called *event horizons*, and space–time regions contained within event horizons are called classical *black holes*. For example, the Kerr black hole solution to Einstein's equations (*i.e.* a spinning black hole) is of particular interest to gravitational wave astronomy, and will be discussed in Chapter (5). It is also noteworthy that black holes have observer dependent "apparent horizons". Apparent horizons are surfaces that bound regions of space-time where light rays that are directed outwards move outwards, and light rays that are directed outward yet moving inward. In Numerical Relativity (Section 2.3), they are of practical use for determining the properties of black holes are on the computational grid.

We should also note that the right hand side of Equation (4), which holds information about the distribution of matter, is generalized to $8\pi G T_{\mu\nu}$, where information about the distribution of *both* matter and energy is encapsulated in the *energy–momentum tensor*, $T_{\mu\nu}$. Similarly, the left hand side of Equation (5) may be thought of as a generalization of Equation (4)'s left hand side, where ∇^2 is generalized by $R_{\mu\nu}$ and R. However, an important point of contrast is that Equation (4)'s left hand side contains only spatial derivatives (there is no embedded concept of space-time), while Equation (5)'s differential operations are on the unified space and time[7]. This last point heralds the existence of gravitational waves.

1.2 Gravitational Waves

We will proceed in this section much as in the last: by focusing on only the most pertinent math details in tandem with the conceptual foundations. For this reason, unfortunately, meaningful details will be left aside[8]. That is, through what is intended as brisk overview, we currently lend our attention to *waves in space-time*.

On Waves and Radiation. First, a point of clarification: while all forms of radiation are waves, not all waves are radiation. That is, by definition, radiation is a class of wave that carries energy *infinitely far away* from a physical source (*e.g.* a circular antenna, or a system two black holes). But how can this be? And why is it not that all emission carries energy infinitely far away from a radiating source? These question may be efficiently answered by noting two ideas: Firstly, for the emission to be physical, its amplitude observed at a distance r from the source must tend to zero as $r/(\text{the scale of the source}) \to \infty$. This implies that the *slowest decaying* component of the emission must scale as r^{-n}, where $n > 0$. Secondly, what is observable is the ability of the emission to affect patches of area at r; this makes the total energy of the emission on shells of area $4\pi r^2$ a meaningful, if not fundamental measure. Moreover, if $\psi(r, \theta, \phi) \sim r^{-n}$ is the emission[9] at r, then it's energy

[7] One might also notice that the argument for constructing Equation (5) ensures that Equation (4) is recovered in the weak field (flat space) limit.

[8] However, the author would like to refer the reader to reference [15] for a more complete motivation and description of gravitational waves.

[9] Here, θ and ϕ are angles of orientation relative to the source.

density scales[10] as $\psi^2 \sim r^{-2n}$. As a result, the total energy emitted through a shell of radius r must scale as $r^2\psi^2 \sim r^2(1-n)$. Concurrently, for the emission to be physical, $r^2\psi^2$ must not increase as r increases, for this would imply that energy is spontaneously being added to the emission throughout space, making the emission more measurable are larger distances. This leaves $2(1-n) \geq 0$ as our only option for physical systems. Moreover, this means that $n = 1$, or equivalently, $\psi(r, \theta, \phi) \sim \frac{1}{r}$, must describe the scaling of the slowest decaying emission. *This* is radiation. Its energy is invariant on spherical shells about the source. All other emission, having $n > 1$, decays faster and therefore cannot be observed far away, thus making the $1/r$ emission the most practical for long range observation.

Weak Field Gravity & Gravitational Plane Waves. As we work to consider gravitational radiation in basic detail in Chapter (2), the discussion above motivates the following *perturbative* view of the flat space-time metric:

$$g_{\mu\nu} = \eta_{\mu\nu} + h_{\mu\nu} \ . \tag{6}$$

That is, we wish to consider space-time dynamics on the flat space metric, $\eta_{\mu\nu}$, plus a small perturbation $h_{\mu\nu}$. Our specific aim, at least for the moment, is to contemplate general relativistic effects when space-time is approximately flat, such as in the case of a gravitational wave detector, far away from the wave source. Canonically, $h_{\mu\nu}$ is used to denote small deviations from flat space-time and, as one contemplates the mathematics, only quantities proportional to the first power in $h_{\mu\nu}$ are retained. Concurrently, to construct this weak-field picture or General Relativity, it is noted that the equivalence of physical laws in different reference frames demands that coordinate transformations of the form $x^\alpha \rightarrow x'^\alpha = x^\alpha + \xi^\alpha(x)$, correspond to $g_{\mu\nu}(x) \rightarrow g'_{\mu\nu} = \frac{\partial x^\lambda}{\partial x'^\mu}\frac{\partial x^\kappa}{\partial x'^\mu} g_{\lambda\kappa}(x)$. This *gauge* symmetry of General Relativity enables the significant simplification of the mathematics. In particular, the following discussion concedes the *transverse–traceless* (TT) gauge, where $\xi^\alpha(x)$ is chosen such that $h^{0\mu}, \ h^a{}_a = 0$, and $\partial^b h_{ab} = 0$.

[10]This is an argument that makes use of dimensional analysis, and the notion that the emission travels along r.

In particular, when the above points are used to re-develop Einstein's equations, Equation (6) recasts Equation (5) as

$$\Box h_{\mu\nu} = -16\pi G T_{\mu\nu} \; . \tag{7}$$

Here, $\Box$ is commonly referred to as the *wave operator*,

$$\Box \; = \; \eta^{\mu\nu}\partial_\mu\partial_\mu \; = \; -\partial_t^2 + \nabla^2 \; . \tag{8}$$

The last equality in Equation (8) has been written to accentuate that $\Box$ acts on both temporal and spatial dimensions (*i.e.* ∂_t^2 and ∇^2 respectively). Given the appropriate physical boundary conditions, this operator is recognized in a broad scope of physical phenomena, such as in electromagnetic theory and fluid mechanics, as describing spatial correlations that vary in time – waves. But let's be more specific.

All cases in this thesis pertain to Equation (5) in vacuum, where $T_{\mu\nu} = 0$. This means that we are interested in solutions of

$$\left(-\partial_t + \nabla^2\right) h_{\mu\nu} = 0 \; . \tag{9}$$

One of the simplest of such solutions is

$$h_{\mu\nu} = H_{\mu\nu} \exp(ik_\alpha x^\alpha) \; . \tag{10}$$

Note that Equation (10) is written as a complex exponential only for convenience – the physical form of this class of solutions is a real valued, linear combination of sines and cosines[11].

Applying Equation (9) to Equation (10) yields that $k^\alpha k_\alpha = \eta_{\mu\nu} k^{mu} k^\nu = 0$ (*i.e.* under Einstein's General Relativity, gravitational waves travel at the speed of light). Moreover, as we are working in a background metric where x^α may be identified as $x^\alpha = (t, x, y, z)$, it follows that $k^\alpha = (\omega, \vec{k})$, where ω is the wave's frequency, and $\vec{k} = (k_x, k_y, k_z)$ points in the direction that the wave travels. In particular, if we consider a wave traveling in the z–direction, then the resulting $A_{\mu\nu}$ is *traceless*, and only has components that are *transverse*

[11] via Euler's formula, $\exp(ix) = \cos(x) + i\sin(x)$

to k^α.

$$H_{\mu\nu} = \begin{pmatrix} 0 & 0 & 0 & 0 \\ 0 & H_{xx} & H_{xy} & 0 \\ 0 & H_{xy} & -H_{xx} & 0 \\ 0 & 0 & 0 & 0 \end{pmatrix} . \tag{11}$$

By inspection of Equation (10), it is visible that, mathematically, $h_{\mu\nu}(x^\alpha = 0) = H_{\mu\nu}$. However, the physical significance of $H_{\mu\nu}$ may be illustrated by considering the effect of our wave on two free particles with separation vector $S^\sigma = (0, S^{(1)}, S^{(2)}, 0)$ (i.e. the particles are only separated along the x–y plane). Here, geodesic deviation, Equation (3), gives *quasi*–linear differential equations for which the particle separation, $S^\sigma(t)$, must satisfy. In particular, we are to consider approximate solutions of $A^\mu = \partial_t^2 S^\mu = \frac{1}{2} S^\alpha \partial_t^2 \, h^\mu_\alpha$. The individual significance of H_{xx} is illuminated by considering the case where $H_{xy} = 0$. This yields

$$\partial_t^2 S^{(1)} = \frac{1}{2} S^{(1)} \partial_t^2 (H_{xx} \cos(\omega t)) \, , \quad \text{and} \quad \partial_t^2 S^{(2)} = -\frac{1}{2} S^{(2)} \partial_t^2 (H_{xx} \cos(\omega t)) \, , \tag{12}$$

which have lowest order solutions[12] given by

$$S^{(1)} \approx (1 + \frac{1}{2} H_{xx} \cos(\omega t) S^{(1)}|_{t=0} \, , \quad \text{and} \quad S^{(2)} \approx (1 - \frac{1}{2} H_{xx} \cos(\omega t) S^{(2)}|_{t=0} \, . \tag{13}$$

Therefore, as each individual particle follows a geodesic[13], the displacement between those geodesics is affected by the gravitational wave. For $S^{(1)}$, the factor of $[1 + \frac{1}{2} H_{xx} \cos(\omega t)]$ means that the x–displacement of the test particles grows when $\cos(\omega t) > 0$, and shrinks when $\cos(\omega t) < 0$. Similarly, for $S^{(2)}$, the factor of $[1 - \frac{1}{2} H_{xx} \cos(\omega t)]$ means that the y–displacement of the test particles shrinks when $\cos(\omega t) > 0$, and grows when $\cos(\omega t) < 0$. This alternating, vertical/horizontal growing and shrinking traces a *plus* pattern in t (*e.g.* Figure 1). Repeating the game above, but with $H_{xx} = 0$, demonstrates that H_{xy} corresponds to a *cross* pattern (e.g. warping at 45° rather than along the x and y axes).

[12] The approximation treats $S^{(1)}$ and $S^{(2)}$ on the right hand side of Equation (12) as constants given by $S^{(1)}|_{t=0}$ and $S^{(2)}|_{t=0}$. For the cross polarization, an eigenvector representation of the solution is useful.

[13] This is lightly discussed in Section (1.1). See [15] or [16] for a proper discussion.

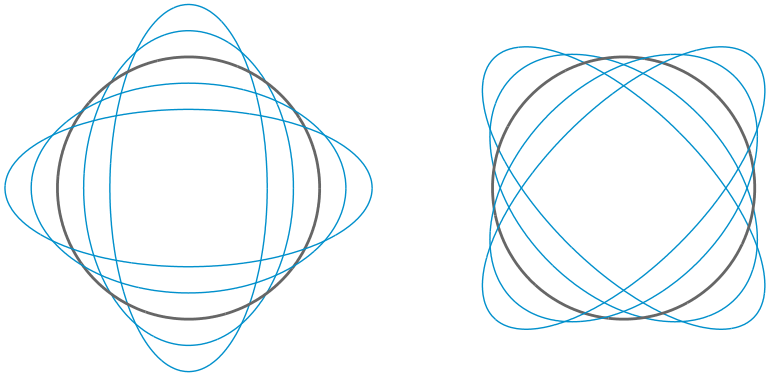

Figure 1: The approximate effect of *plus* (left) and *cross* (right) gravitational wave polarizations on a ring of test particles.

For these reasons, H_{xx} is identified with the wave's "plus–polarization", and H_{xy} is identified with the wave's "cross–polarization", and Equation (10) is often compactly rewritten as

$$\boxed{h_{ab} = \begin{pmatrix} h_+ & h_\times \\ h_\times & -h_+ \end{pmatrix} = \begin{pmatrix} H_{xx} & H_{xy} \\ H_{xy} & -H_{xx} \end{pmatrix} \exp(ik_\alpha x^\alpha) \, .} \tag{14}$$

Equation (14) is the principle result of this section: *it demonstrates that gravitational waves affect spacetime in a manner that is transverse to their propigation direction, and consistent with two polarizations (plus and cross).*

Aside on Gravitational Wave Interferometry. It is important to note that gravitational wave detectors such as LIGO and Virgo[14], which track the passage of light back and forth between mirrors, are primed to measure the geodesic deviation[15] incurred in flight. In particular, they are schematically similar to a Fabry-Perot Michelson Interferometer, Figure (2), where laser light of wavelength λ is split into two directions, towards arms of unperturbed length L. Along each arm, mirrors are placed such that the typical photon travels a total distance on the order of $10^2 L$

[14]Located in Italy, Virgo is a gravitational wave detector that is a part of the European Gravitational Wave Observatory.

[15]Equivalently, it can be said that they aim to measure the integrated proper distance (Equation 2) between the two mirrors.

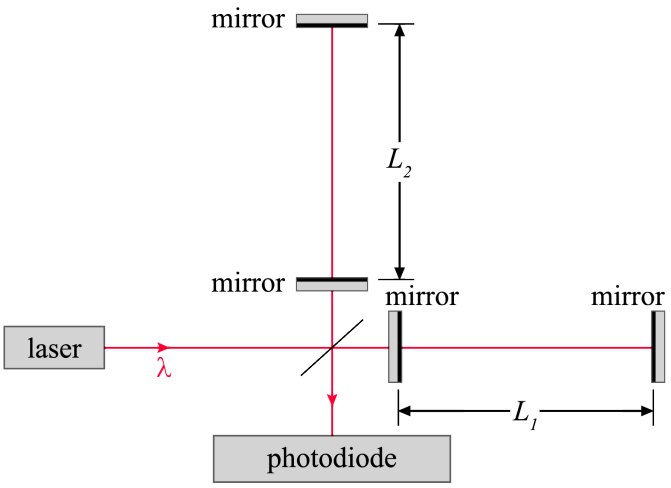

Figure 2: A schematic for an interferometric gravitational wave detector.

before heading back towards the beam splitter, where it is directed towards a photodiode which converts the optical signal into an electrical one. The configuration is such that, if there is no gravitational wave, the returning light waves cancel each other out perfectly, resulting in no signal. However, in the presence of gravitational radiation, where the deviation between arm lengths is $\delta L = L_2 - L_1$, Equation (13) suggests that the observable phase shift, $\delta\phi$, will be proportional to the detected strain, $h^{\rm det}(t)$, and will scale as

$$\delta\phi \;\sim\; 2\,(10^2)\,\frac{2\pi}{\lambda}\,\delta L \;\sim\; 200\frac{2\pi L}{\lambda}\,h^{\rm det}(t)\;.$$

Ideally, if L_1 and L_2 lie along the x and y axes of Equation (10), then only the h_+ polarization will be detected with

$$h^{det}(t) = \frac{\delta L}{L} = h_+(t)\ [17].$$

However, as LIGO is a network of detectors, each with their own multipolar antenna pattern, the detected strain will generally be of the form

$$h^{det}(t) = F_+ h_+(t) + F_\times h_\times(t)\;,$$

where F_+ and $F_\times$ encapsulate information about a single detector's antenna pattern.

1.3 Chapter Summary

We have now touched upon basic gravitational wave theory: gravitational waves travel at the speed of light, and correspond to tidal forces in directions transverse to their propagation. We have noted that gravitational waves can be detected via the effect of their weak tidal forces on test masses, and that the waves that are most likely to be detected correspond to radiation. However, we have yet to connect gravitational wave theory with the equally central topic of the *gravitational radiation* produced by massive astrophysical systems – in particular, binary black holes, for which there is good hope for detection [18, 19, 20, 21].

Chapter II

THE GRAVITATIONAL RADIATION OF COMPACT BINARIES

Thus far, we have motivated Einstein's theory of gravity, and we have shown that it supports plane wave solutions in the weak field limit (Equations 10-14). Now, we are primed to review the class of gravitational waves that are at the center of this thesis: *the gravitational radiation generated by two compact objects in a slowly decaying, quasi-circular orbit, that leads to relativistic, strong-field merger, and ultimately ringdown.* Our interest in this type gravitational radiation is primarily motivated by its expected relevance to gravitational wave detection, whereby the detection of multiple binary black hole systems per year is expected in the advanced detector era [18]. To pursue this interest, we must break from the perspective of Section (1.2), and contemplate the production of gravitational waves in the presence of matter and/or curvature, where $T_{\mu\nu} \neq 0$.

Specifically, we will incrementally contemplate the dynamics of two compact objects (*e.g.* two black holes) orbiting each other in a quasi-circular fashion: First, when the objects are far from each other, and moving slowly with respect to the speed of light, we will consider the Newtonian regime (Section 2.1). Second, we will consider the more astrophysically relevant Post–Newtonian regime, where velocity and curvature are coupled (Section 2.2). Third, as the Post–Newtonian approximations are incapable of capturing the full non-linearity of General Relativity, we will review the approach of Numerical Relativity (Section 2.3). Lastly, we will briefly introduce gravitational ringdown. These topics inform us about the data from which this thesis' results are derived and discussed.

2.1 The Quasi–Newtonian Limit

The goal of this section is to quickly discuss gravitational waves from compact binaries near the Newtonian limit. This topic is foundational for the Post-Newtonian description of gravitational radiation, which in tern, significantly informs Numerical Relativity's efforts to

calculate gravitational radiation.

We begin by imagining the effect of gravity on two compact objects separated by a distance d that is large enough for general relativistic effects to be small. In particular, we will consider d to be large compared to the dynamical length scale of the system[1] given by $2GM/c^2$, where M is the total system mass. This is equivalent to the condition that

$$\frac{GM}{dc^2} \ll 1 \, . \tag{15}$$

Moreover, we are to imagine that the objects orbit the location of their center of mass, in a manner that is *almost* perfectly circular. Figure (3)'s left panel illustrates this configuration for the case of a binary black hole system. Here, the Newtonian gravitational force between the objects must be negated by the outward "centrifugal" force, yielding

$$\frac{\mu v^2}{(d/2)} = G\frac{M\mu}{d^2} \, . \tag{16}$$

Here, μ is the system's reduced mass, $\mu = \frac{m_1 m_2}{M}$, with $M = m_1 + m_2$.

In congress, Equations (15-16) communicate that we are considering a limit familiar to Special Relativity: each object's velocity is small relative to the speed of light,

$$\frac{GM}{dc^2} = \frac{v^2}{c^2} \ll 1 \, . \tag{17}$$

It is therefore reasonable to expect that, for very large d, the dynamics are approximately Newtonian, but with general relativistic deviations described by the addition of successive terms, weighted by increasing powers of v/c. Per the title of this subsection, the author considers this regime to be *quasi*–Newtonian. To consider this point further, and to eventually contemplate more general gravitational wave emission by compact binaries, we must review the consequences of the weak field Einstein's equations where $T_{\mu\nu} \neq 0$.

Weak Field Sources. In the presence of matter, curvature, or both, we must consider Einstein's equations(Equation 5) with $T_{\mu\nu} \neq 0$. It is simplifying to start in the Lorentz gauge, rather than the TT gauge of Section (1.2). Specifically, we are to work with

$$\bar{h}_{\mu\nu} = h_{\mu\nu} - \frac{1}{2}\eta_{\mu\nu}h \, , \tag{18}$$

[1]Here GM/c^2 may be derived from dimensional analysis; whilie the factor of two is added here to be consistent with the Schwarzschild radius, $2GM/c^2$.

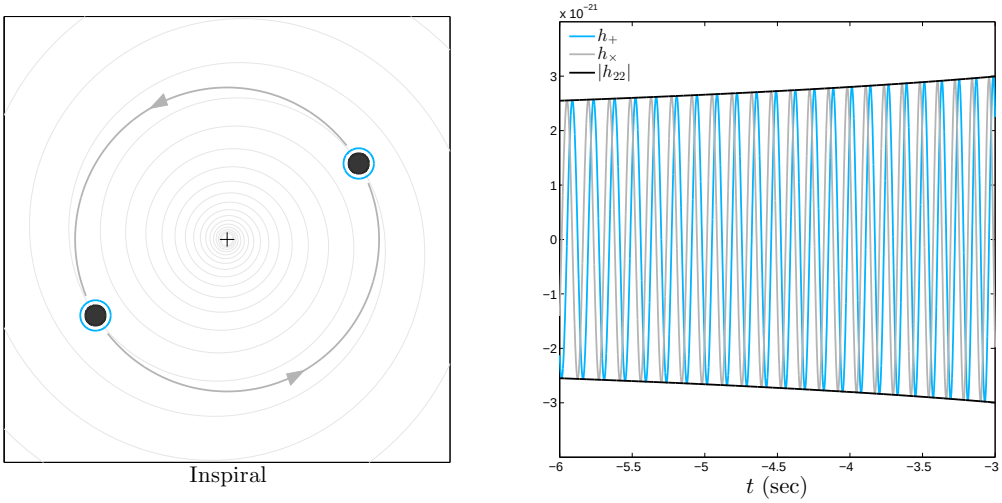

Figure 3: Black Hole inspiral for a 1:1 mass ratio, initially nonspinning black hole binary having initial total mass of 100 $M_\odot$, and observed at $r = 100$ Mpc. *Left*: A qualitative schematic of the binary black hole configuration. The black hole's apparent horizon is shown by the blue curve. *Right*: Here we see the analogous gravitational wave emission in physical units. Specifically, we are shown a period of late merger, where the gravitational wave amplitude increases noticeably in time. This waveform was calculated using the Taylor-T4 Post Newtonian approximant [1].

along with the Lorentz gauge[2] condition that $\partial^\mu \bar{h}_{\mu\nu} = 0$. This, as well as the linearization of Einstein's equations via Equation (6), yields

$$\Box \bar{h}_{\mu\nu} = -\frac{16\pi}{c^4} T_{\mu\nu} \ . \tag{19}$$

In Equation (19), I have broken from the $c = 1$ convention in order to connect with our previous discussion.

In seeking solutions to Equation (19), it is noted that in this limit the source is too far away to affect space-time curvature at the observer's location, hence the flat background metric $\eta_{\mu\nu}$. Concurrently, this means that $T_{\mu\nu}$ is determined only by the content of the physical system, and does not depend dynamically on $\bar{h}_{\mu\nu}$. Therefore, in this limit, we may treat $T_{\mu\nu}$ as a completely known quantity. This point allows us to seek an integral solution to Equation (19), whereby $\bar{h}_{\mu\nu}$ is equated to some linear operation on $T_{\mu\nu}$. In particular, it

[2]Note that we may always project $\bar{h}_{\mu\nu}$ into the TT gauge when desired. See Eq. 1.36 of reference [15].

is noted that given some $G(x-x')$, such that

$$\Box_x G(x-x') = \delta^4(x-x') \ , \tag{20}$$

solutions of Equation (19) can be written as

$$\bar{h}_{\mu\nu}(x) = -\frac{16\pi G}{c^4} \int G(x-x')\, T_{\mu\nu}(x') \mathrm{d}^4x' \ . \tag{21}$$

Here, the 4–vector x'^{μ} (written as x' when in a function argument) is located in the source, while x^{μ} (written as x when in a function argument) is collated with the observer.

Physically, this approach is equivalent to considering the source to be made up of point particles, and thereby holding that the total solution be an integral over solutions on each particle[3]. In the context of the binary black hole problem, each black hole is treated as a pint particle in this limit.

To proceed, $G(x-x')$ is determined by holding $\bar{h}_{\mu\nu}$ to be zero at infinity, along with the property that $\int \delta^4(x-x')\mathrm{d}^4x' = 1$. Moreover, $G(x-x')$ is further constrained by the notion that the radiation propagates in a causal, time increasing manner. Together, these ideas yield[4]

$$G(x-x') = \frac{-1}{4\pi|\mathbf{x}-\mathbf{x}'|}\delta(x^0_{\mathrm{ret}} - x'^0) \ , \tag{22}$$

where $\mathbf{x} = (x^{(1)}, x^{(3)}, x^{(3)})$, $x'^0 = ct'$, $x^0_{\mathrm{ret}} = ct_{\mathrm{ret}}$ and $t_{\mathrm{ret}} = t - \frac{|\mathbf{x}-\mathbf{x}'|}{c}$. Here, t is the time the wave is observed, and t_{ret} is the time the wave began to propagate away from the source.

Together, Equations (21-22) give

$$\bar{h}_{\mu\nu}(t,\mathbf{x}) = \frac{4G}{c^4} \int \frac{1}{|\mathbf{x}-\mathbf{x}'|}\, T_{\mu\nu}(t_{\mathrm{ret}}, \mathbf{x}')\, \mathrm{d}^3x' \ . \tag{23}$$

In the Radiation Zone. We now touch base with Section (1.2)'s very conceptually driven discussion of radiation. Specifically, with Equation (23) in hand, it is now clear that the gravitational wave emission, $\bar{h}_{\mu\nu}$, depends on $\frac{1}{|\mathbf{x}-\mathbf{x}'|}$. Moreover, all likely gravitational wave observations will take place far away from the source, meaning that if spatial length

[3] In Equation (22), $G(x-x')$ is dubbed the *Green's Function*, after British mathematician George Green, who developed the method in the 1830s after his father's death, and a subsequent bequeathal of a small fortune, which allowed Green to devote himself to maths rather than milling.

[4] See page 340 of reference [22] for a full treatment.

scale of the source is d, where $d \gtrsim |\mathbf{x}'|$, then the observer is at a distance $r = |\mathbf{x}|$, where $r \gg d$. Consequently, a good approximation for $\frac{1}{|\mathbf{x}-\mathbf{x}'|}$ can be gleamed from it's Taylor series expansion:

$$\begin{aligned} \frac{1}{|\mathbf{x}-\mathbf{x}'|} &= e^{-\mathbf{x}'\cdot\nabla}\frac{1}{|\mathbf{x}|} = e^{-\mathbf{x}'\cdot(\hat{x}\partial_r)}\ \frac{1}{r} \\ &= \sum_{k=0}^{\infty}\frac{(-\mathbf{x}'\cdot\hat{x}\partial_r)^k}{k!}\frac{1}{r}\ \approx\ \frac{1}{r}+\frac{\mathbf{x}\cdot\mathbf{x}'}{r^3}\ . \end{aligned} \tag{24}$$

Following Section (1.2), we are only interested in the radiation term, given by $1/r$, and we disregard higher order terms, like $\frac{\mathbf{x}\cdot\mathbf{x}'}{r^3}$, as they do not contribute significantly to the radiated energy at very large distances. Our broad aim is to use $r \gg d$ to *unpack* the amount of information needed about the source in order to solve Equation (23) to some *leading-order* accuracy. To this end, applying Equation (24) to Equation (23) gives

$$\bar{h}_{\mu\nu}(t,\mathbf{x}) = \frac{4G}{c^4}\frac{1}{r}\int T_{\mu\nu}(t_{\text{ret}},\mathbf{x}')\,\mathrm{d}^3x'\ . \tag{25}$$

Recalling that $t_{\text{ret}} = t - \frac{|\mathbf{x}-\mathbf{x}'|}{c}$, it is clear that $r \gg d$ enables another expansion about the source, and therefore another opportunity to rewrite Equation (23) in its most dominant term.

The Multipole Moment Expansion. It was remarked in the last paragraph that $t_{\text{ret}} = t - \frac{|\mathbf{x}-\mathbf{x}'|}{c}$ implies that an expansion of Equation (23) is appropriate in the radiation zone. Specifically,

$$|\mathbf{x}-\mathbf{x}'| \approx r - \hat{x}\cdot\mathbf{x}' \tag{26}$$

gives that

$$t_{\text{ret}} = \left(t-\frac{r}{c}\right)+\frac{\hat{x}\cdot\mathbf{x}'}{c}\ . \tag{27}$$

Here, there is no preference for approximating $|\mathbf{x}-\mathbf{x}'|$ with only r, as there is no corresponding radiative measurement for $|\mathbf{x}-\mathbf{x}'|$. Therefore, keeping the linear term in the series expansion (i.e. $\hat{x}\cdot\mathbf{x}'$), enables a "next to leading order" expansion of $T_{\mu\nu}(t_{\text{ret}},\mathbf{x}')$ about

$t_{\rm ret} = t - \frac{r}{c}$,

$$\begin{aligned} T_{\mu\nu}(t_{\rm ret}, \mathbf{x}') &= T_{\mu\nu}(\Big(t - \frac{r}{c}\Big) + \frac{\hat{x}\cdot\mathbf{x}'}{c}, \mathbf{x}') \\ &= \sum_{k=0}^{\infty} \frac{1}{k!}\left(\frac{\hat{x}\cdot\mathbf{x}'}{c}\partial_\tau\right)^k T_{\mu\nu}(\tau, \mathbf{x}')|_{\tau=t-r/c} \\ &= T_{\mu\nu}(t - \frac{r}{c}, \mathbf{x}') + \frac{x'^i\hat{x}_i}{c}\partial_\tau T_{\mu\nu}|_{\tau=t-r/c} + \frac{1}{2c^2}x'^i x'^i\hat{x}^j\hat{x}^j\partial_\tau^2 T_{\mu\nu}|_{\tau=t-r/c} + \ldots . \end{aligned} \tag{28}$$

While Equation (28) does yield an appropriate unpacking of Equation (25)'s right hand side, it is physically illuminating to consider the $T_{\mu\nu}(t_{\rm ret}, \mathbf{x}')$ to be the Fourier transform of its frequency domain counterpart,

$$T_{\mu\nu}(\tau, \mathbf{x}') = \int \tilde{T}_{\mu\nu}(\omega, \mathbf{k})\, e^{-i\omega\tau + i\mathbf{k}\cdot\mathbf{x}')}\, \frac{\mathrm{d}\omega\, \mathrm{d}^3k}{(2\pi)^4} . \tag{29}$$

Specifically, letting $\tau = t - \frac{r}{c} + \frac{\mathbf{x}'\cdot\hat{x}}{c}$, gives

$$T_{\mu\nu}\left(t - \frac{r}{c} + \frac{\mathbf{x}'\cdot\hat{x}}{c}, \mathbf{x}'\right) = \int \tilde{T}_{\mu\nu}(\omega, \mathbf{k})\, e^{-i\omega(t - r/c + \mathbf{x}'\cdot\hat{x}/c) + i\mathbf{k}\cdot\mathbf{x}'}\, \frac{\mathrm{d}\omega\, \mathrm{d}^3k}{(2\pi)^4} . \tag{30}$$

Here, it is noted that exponential has an explicit dependence on $\omega\mathbf{x}'\cdot\hat{x}$, which has units of velocity. This allows us to identify the exponential's Taylor series expansion[5], and thereby reframe the terms in Equation (28). Specifically, we have that

$$e^{-i\omega(t-r/c+\mathbf{x}'\cdot\hat{x}/c)} = e^{-i\omega(t-r/c)} \times \{1 - i\frac{\omega}{c}x'^i\hat{x}^i + \frac{1}{2}(-i\frac{\omega}{c})^2 x'^i x'^i\hat{x}^j\hat{x}_j + \ldots\} , \tag{31}$$

which is an expansion in powers of velocity (i.e. at frequency ω) divided by the speed of light. Formally, when plugged into Equation (25), this *velocity expansion* is equivalent to Equation (31). Moreover, it inspires identification of each term in Equation (31) with a multipole moment – one of s set of orientation dependent functions. Of particular importance is the leading order, "quadrapole" term in Equation (31). It is identified with the mass quadrapole moment[6], given by

$$\begin{aligned} \partial_t^2 M_{ij}(t - r/c) &= 2\int T_{ij}(t - r/c, \mathbf{x}')\, \mathrm{d}^3x' \\ &= 2\partial_t^2 \int x'_i x'_j\, T^{00}(t - r/c, \mathbf{x}')\, \mathrm{d}^3x' . \end{aligned} \tag{32}$$

[5]Note that the indices in Equation (31)'s right hand side label terms in the standard Euclidean dot product, not that given by Equation (2).

[6]In Equation (32), the double time derivative is motivated by considering mass–eneergy conservation (*i.e.* $\partial_\sigma T^{\sigma\mu} = 0$).

The second line writes the definition of M_{ij} explicitly. Applying Equation (32) to our current expression for the gravitational wave strain, $\bar{h}_{\mu\nu}$ (Equation 25), gives the appropriately named "quadrapole forumla",

$$\bar{h}_{\mu\nu} \approx \frac{1}{r}\frac{2G}{c^4}\partial_t^2 M_{\mu\nu}(t - r/c) \, . \tag{33}$$

In the preponderance of physically meaningful cases, Equation (33) represents the lowest order, most dominant contribution to the solution of Equation (19).

The Case of Compact Binaries. Finally, Equation (33) enables the qualitative evaluation of the gravitational radiation due to compact binaries when their separation length is large (*i.e.* $\frac{GM}{dc^2} \ll 1$). To see this, Equation (32) says that we must first determine for the system T^{00}: Under the current scheme of approximations, $T^{00} \approx c^2\rho$, where ρ is the mass density of the source (*i.e.* Equation 4). As we are considering d to be large, it is fair to imagine that ρ is comprised of delta functions at the location of each object. Let's further simplify the situation by imposing that the object have the same mass, $m_1 = m_2 = M$. Now, to write down T^{00}, we turn back to the discussion at the beginning of this section, in particular Equation (16), where it was noted that circular motion corresponds to the condition

$$\frac{v^2}{(d/2)} = G\frac{M}{d^2} \, .$$

Equivalently, we have that each object moves with speed $v = \sqrt{GM/2d}$, which corresponds to an angular velocity $\Omega = \sqrt{2GM/d^3}$. Therefore, if we label the objects with a and b, the trajectory that object–a takes is given by

$$x_a^{(1)} = (d/2)\cos(\Omega t), \quad x_a^{(2)} = (d/2)\sin(\Omega t) \, .$$

Similarly, for object b, we have that

$$x_b^{(1)} = -(d/2)\cos(\Omega t), \quad x_b^{(2)} = -(d/2)\sin(\Omega t) \, .$$

Concurrently, imposing that the spatial integral over ρ results in $2M$ gives

$$\begin{aligned} T^{00}(t) =& c^2 M\, \delta(x^{(3)}) \, [\, \delta(x^{(1)} - R\cos(\Omega t))\delta(x^{(2)} - R\cos(\Omega t)) \\ &+ \, \delta(x^{(1)} + R\cos(\Omega t))\delta(x^{(2)} + R\cos(\Omega t)) \,] \, . \end{aligned} \tag{34}$$

The resulting strain waveform is

$$\bar{h}_{ij}(t, r, \theta = 0, \phi = 0) = \frac{1}{r}\frac{2GM}{c^4}\Omega^2 d^2 \begin{pmatrix} -\cos(2\Omega t_r) & -\sin(2\Omega t_r) \\ -\sin(2\Omega t_r) & \cos(2\Omega t_r) \end{pmatrix} . \tag{35}$$

As before, we have chosen an observational frame that limits excitation to the x–y plane; therefore, as written above, $\bar{h}_{ij} = h_{ij}$ (*i.e.* it is in the TT gauge). Generally, if the wave travels at an angle θ relative to the observer's z–axis, and at an angle ϕ, relative to the observer's x–axis, then we must *project* into the TT gauge according to $h_{ij} = \Lambda_{ij,kl}\bar{h}_{kl}$, where

$$\Lambda_{ij,kl}(\hat{n}) = P_{ik}P_{jl} - \frac{1}{2}P_{ij}P_{kl} , \tag{36}$$

and $P_{ij}(\hat{n}) = \delta_{ij} - n_i n_j$. With the above choice of orientation, $n = (\sin\theta\sin\phi, \sin\theta\cos\phi, \cos\theta)$. Working through the algebra, while keeping in mind Equation (14), the projection results in[7]

$$h_+(r, \theta, \phi, t) = \frac{1}{r}\frac{GM}{2c^4}d^2\Omega^2\left(\frac{1 + \cos^2\theta}{2}\right)\cos(2\Omega t_r) , \tag{37}$$
$$h_\times(r, \theta, \phi, t) = \frac{1}{r}\frac{GM}{2c^4}d^2\Omega^2\cos(\theta)\sin(2\Omega t_r) .$$

Equation (37) contains the very rudimentary features of the gravitational radiation of compact binaries: the waveform is time oscilatory, with an amplitude that depends inversely with the distance from the source, as well as the observer's orientation relative to the binary's orbital plane. However, while Equation (37) is simply put, it is only pertinent to gravitational wave detection, and thereby gravitational wave modeling, when the condition that d is large holds – the weak field limit. But by construction, this is the regime where the morphology of the radiation is the most regular, and simultaneously, the least powerful in time. Even more so, the approximations used above essentially *turn off* essential features of gravitational radiation, such as the coupling between velocity and curvature, and the dynamical relationship between the source's trajectories and the emitted gravitational waves. The fully *Post*–Newtonian formalism has been developed to confront these limitations, at least, prior to the regime where strong field effects truly begin to dominate.

[7]Equation (37) is often referred to as the "restricted" Post-Newtonian waveform.

2.2 The Post–Newtonian Limit

Unlike in the last section, here I will spare the reader a hearty construction of the main ideas. This will largely be aided by my having already presented the key foundational concepts: *gravitational wave strain, and the multipole expansion of gravitational radiation.* Thusly, my goal in this section to introduce the motive behind the Post-Newtonian expansion of Einstein's equations, as well as a description of how the machinery is relevant to this thesis. The description here roughly follows the Blanchet–Damour approach as outlined in reference [23].

Motivations for Post-Newtonian. As described in Section (2.1), only the very rudimentary nature of the gravitational radiation from compact objects can be captured in the Newtonian limit. There are crucial physical features missing from Section (2.1)'s considerations, such as radiation–reaction, and the entire host nonlinear effects. As these elements ultimately impact the observed gravitational radiation in the late and final stages of coalescence, there is a practical need to go beyond the quadrapole formula's leading order description (Equation 35).

More on Multipoles. For gravitationally bound systems that deviate from the weak field limit (Equation 15), Equation (28) should be considered beyond the leading order quadrapole term. Examination of the next–to–leading order terms reveals tensor objects of positive symmetry under the permutation of indices[8] (the "mass octopole" moments), as well as objects of mixed symmetry (the "current quadrapole moment")[9]. Extending this consideration to higher terms allows the identification of general order mass–type moments, $\mathcal{U}_L$, and current–type moments, $\mathcal{V}_L$. Here, we will use a multi–index notation, where $L = i_1 \cdots i_l$ for a multi-index composed of l multipolar spatial indices $i_1, \cdots, i_l$ (ranging from 1 to 3). Additionally, $L-1 = i_1 \cdots i_{l-1}$, $aL-2 = a i_1 \cdots i_{l-2}$, and $\hat{r}_L = \hat{r}_{i_1} \cdots \hat{r}_{i_l}$ is the product

[8]Symmetry under permutation of the indices: *e.g.* $M^{ij} = +M^{ji}$ rather than $M^{ij} = -M^{ji}$ (anti-symmetry), or some *mixture*, $M^{ij} = A^{ji} + B^{ji}$.

[9]Here, it is "current quadrapole" as it relates to the lowest order angular momentum density, while the "mass octopole" is second order by mass density.

of l spacial vectors $\hat{r}_i$. Furthermore, in terms such as $A_L B_L$, a summation over all indices is implied [23]. Under this extended expansion, and its new notation, the gravitational wave strain takes the form

$$h_{ij} = \frac{4G}{c^2 r}\,\mathcal{P}_{ij}{}^{kl}(\hat{r}) \sum_{l=2}^{+\infty} \frac{1}{c^l l!}\left\{ \hat{r}_{L-2}\,\mathcal{U}_{klL-2}(t_r) - \frac{2l}{c(l+1)}\,\hat{r}_{aL-2}\,\varepsilon_{ab(k}\,\mathcal{V}_{l)bL-2}(t_r) \right\} + \mathcal{O}\left(\frac{1}{r^2}\right). \tag{38}$$

Here, the unit vector pointing from the source to the observer was been written as $\hat{r}$, rather than $\hat{x}$ as was used in the last section. Moreover, we have introduced the projection of the strain from the Lorentz gauge to the TT gauge via $h_{ij} = \mathcal{P}_{ij}{}^{kl}(\hat{r})\,\bar{h}_{kl}$. The other notational elements of Equation (38) are ulterior to its significance here. Instead, it is of basic importance to note that Equation (38) the successive evaluation of Equation (38) allows for a precise description of gravitational radiation, nearly until merger (see reference [23] for an expanded discussion). Moreover, here, it is of key conceptual importance that Equation (38) can be written in terms of spherical–type harmonics, reminiscent of electromagnetic field theory [24].

Spherical Harmonic Multipoles. At this point, readers familiar with electrostatic theory will have noticed that Equation (24) (repeated below) was not used to motivate the multipole moments, as is often done for the electric potential.

$$\frac{1}{|\mathbf{x}-\mathbf{x}'|} = \sum_{k=0}^{\infty} \frac{(-\mathbf{x}'\cdot\hat{r}\partial_r)^k}{k!}\frac{1}{r} \;\approx\; \frac{1}{r} + \frac{\mathbf{x}\cdot\mathbf{x}'}{r^3}$$

For example, $\frac{\mathbf{x}\cdot\mathbf{x}'}{r^3}$ is used to identify the electromagnetic dipole contribution. Per Section (2.1), this is because we are only interested in the radiation term, $1/r$, which leaves $T_{\mu\nu}$ to be expanded in terms of decreasing relevance[10] (Equation 38). But by taking this course, we have perhaps deviated away from one of electromagntic theory's most practical tools, the spherical harmonic multipoles[11], $Y_{lm}(\theta,\phi)$.

[10] This is also the approach taken in electrodynamics.

[11] Specifically, by identifying the $1/|\mathbf{x}-\mathbf{x}'|$ as the moment generating function for the Legendre polynomials, and then using the spherical harmonic addition rule, it may be shown that $\frac{1}{|\mathbf{x}-\mathbf{x}'|} = \frac{1}{r}\sum_{l=0}\sum_{-l\leq m\leq l}\left(\frac{x'}{r}\right)^l \frac{4\pi}{2l+1}\,\bar{Y}_{lm}(\theta',\phi')\,Y_{lm}(\theta,\phi)$. This is but one way of motivating the spherical harmonic decomposition of the electric charge density.

Despite the methdological differences mentioned above, the general utility of the spherical harmonic functions is that they form a basis by which scalar functions may be expanded. In particular, given a scalar function $f(\theta,\phi)$, the orthogonality of the spherical harmonics, $\int_\Omega \bar{Y}_{l'm'}(\theta,\phi)\bar{Y}_{lm}(\theta,\phi)\,\mathrm{d}\Omega \;=\; \delta_{ll'}\delta_{mm'}$, enables $f(\theta,\phi)$ to be written as $f(\theta,\phi) = \sum_{l=0}^{\infty}\sum_{-l\leq m\leq l}\; f_{lm}\,Y_{lm}(\theta,\phi)$, where the *spherical harmonic multipole moments*, f_{lm}, are defined by $f_{lm} \;=\; \int_\Omega \bar{Y}_{lm}\,f(\theta,\phi)\,\mathrm{d}\Omega$. Here, $\bar{Y}_{lm}$ is the complex conjugate of Y_{lm}. The eminent practicality of this result is that it enables a problem independent unpacking (*i.e.* spectral decomposition) of any scalar function on the solid angle[12].

However the *scalar* spherical harmonics cannot be directly applied to the decomposition of the *tensoral* gravitational wave strain. In order to obtain an analogous decomposition upon tensors such as Equation (38)'s $\mathcal{U}_L$ and $\mathcal{V}_L$, the *spherical tensor decomposition* is employed. Specifically, the spherical tensor harmonics, $\mathcal{Y}^{lm}_L$, are defined such that $Y_{lm}(\theta,\phi) = \mathcal{Y}^{lm}_L\hat{r}_L$, where the orientation dependence is encapsulated only within $\hat{r}_L$. Just as the $Y_{lm}(\theta,\phi)$ allow the definition of the scalar multipoles, the spherical tensor harmonics enable the definition of the *spherical tensor components*[13]. That is, for a tensor F_L, its spherical components, F_{lm}, are such that

$$F_{lm} \;=\; F_L\int_\Omega \bar{Y}_{lm}\,\hat{r}_L\,\mathrm{d}\Omega \;=\; F_L\,\bar{\mathcal{Y}}^{lm}_{L'}\int_\Omega \hat{r}_{L'}\,\hat{r}_L\,\mathrm{d}\Omega\,. \tag{39}$$

Of current relevance are the tensor components of Equation (38)'s $\mathcal{U}_L$ and $\mathcal{V}_L$.

In particular, the above formalism allows the construction of the mass and spin spherical component tensors (often referred to as simply the mass and current multiple moments),

$$U_{lm} = \frac{16\pi}{(2l+1)!!}\sqrt{\frac{(l+1)(l+2)}{2l(l-1)}}\mathcal{U}_L\bar{\mathcal{Y}}^{lm}_L \quad \text{and} \quad V_{lm} = \frac{-32\pi l}{(2l+1)!!}\sqrt{\frac{(l+2)}{2l(l+1)(l-1)}}\mathcal{V}_L\bar{\mathcal{Y}}^{lm}_L\,. \tag{40}$$

With these multipole tensors in hand, it may be shown (e.g. in reference [25]) that Equation (38) can be framed in the form of a *spin–weighted* spherical harmonic decomposition.

[12]By the solid angle, the author refers to the spherical polar coordinates: $\Omega = (\theta,\phi)$, where $d\Omega = \sin(\theta)d\theta d\phi$.

[13]Here, the reader should note that this topic is of a sufficiently technical nature to sure not be communicated completely here. For the reader interested in anything beyond the cursory description given currently, the author recommends [17, 15, 25] and [23].

Specifically, the scalar quantity H is defined to encapsulate the plus and cross polarizations

$$H(r,\theta,\phi,t) \;=\; h_{+}(r,\theta,\phi,t) \;- i\, h_{\times}(r,\theta,\phi,t)\;, \tag{41}$$

And its multipole expansion is given by

$$\boxed{H(r,\theta,\phi,t) = \sum_{l=2}^{\infty} \sum_{m=-l}^{l} {}_{-2}Y_{lm}\,(\theta,\phi)\; h_{lm}(t)\;,} \tag{42}$$

where the spherical multipole moments of H are

$$\begin{aligned} h_{lm}(t) &= \frac{G}{\sqrt{2}rc^{l+2}} \left(U_{lm} - \frac{i}{c} V_{lm} \right) \\ &= \int_{\Omega} H(r,\theta,\phi,t)\, {}_{-2}\bar{Y}_{lm}(\theta,\phi)\, \mathrm{d}\Omega \end{aligned} \tag{43}$$

In Equation (42) ${}_{-2}Y_{lm}(\theta,\phi)$, are the spherical harmonics of -2 spin weight [26], which, in the context of gravitational waves, can be shown to result from the transverse nature of gravitational radiation (*e.g.* Section 1.2). The first line of Equation (43) expreses the multipoles in terms of the spherical tensor components discussed above, while the second line follows from the orthogonality of the spin weighted spherical harmonics.

Equation (42) enables the key statement of this section: *when modeling gravitational waveforms, it is not h_+ or $h_\times$ that is typically modeled, but rather the spin -2 spherical harmonic multipoles (a.k.a. "modes"), $h_{lm}(t)$.* Therefore, throughout this thesis, the gravitational wave strain polarizations, as well as their multipoles, h_{lm}, will be the predominant focus. The utility of modeling $h_{lm}(t)$ rather than $h(r,\theta,\phi,t)$ is that it assigns the spatial dependence of the waveform to the spherical harmonics (and $1/r$), and therefore reduces the number of variables needed to model a single waveform. In particular, much of the work discussed in this thesis pertains to the time (or frequency) domain modeling of the most dominant $h_{lm}(t)$. It is also important to note that in the preponderance of likely scenarios, only $l < 6$ multipoles are needed to represent the gravitational wave strain to very high accuracy.

While Equations (42-43) are of the utmost relevance here, in order to actually calculate the Post-Newtonian waveforms (*e.g.* beyond Equation 35), one must solve equations for the gravitational waveforms and the trajectories of each compact object. As the extent of

this topic will not be covered here, the author refers the motivated reader to reference [27]. Even so, it is of use to note that such labors result in analytic expressions for gravitational waveforms. For example, for an observer looking down towards the center of the orbital plane, the first few terms of the dominant, $l = m = 2$ multipole (to 3PN order[14]) is given by

$$h_{22}(t) = -8\sqrt{\frac{\pi}{5}}\frac{G\eta M}{c^2 r}e^{-2i\phi(t)}x\left\{1 - x\left(\frac{107}{42} - \frac{55}{42}\eta\right) + x^{3/2}\left[2\pi + 6i\ln\left(\frac{x}{x_0}\right)\right] ... + \ O(\epsilon^{7/2})\right\} . \tag{44}$$

In Equation (44), the waveform's time dependence is encapsulated in the instantaneous orbital phase, $\phi(t)$, and the frequency parameter $x(t) = \frac{1}{4}\left[\left(\frac{\eta c^3}{5Gm}\right)(t_{\text{coalescence}} - t)\right]^{-1/4}$ [25]. Additionally, η is the symmetric mass ratio given by $m_1 m_2/(m_1 + m_2)^2$. Figure (3)'s right panel illustrates the typical morphology quadrapole radiation when observing the system face on. As will be discussed in Chapter (5), the functional form of Equation (44) (and its related expressions not shown here) yield insight into the class of functions compatible with gravitational waveforms, as well as how the waveforms should scale with system parameters such as the symmetric mass ratio η.

Limitations of the Post–Newtonian Expansion. By construction, the Post-Newtonian formalism is an approximation: best in the weak field limit, where velocities are slow relative to the speed of light, and the dynamics of the system are dominated by length scales much greater than the system's inherent dynamical length (Equation 16). As we are to focus on the gravitational radiation of coalescing binaries, the Post-Newtonian approximation inevitably fails: as gravitational radiation is emitted, the binary system loses energy, and the two compact objects in-spiral towards each other at ever shorter separation, and at increasingly fast orbital speeds. While the Post-Newtonian approximation is capable of describing the radiation up to late inspiral, when the orbital separation is on the order of $5 \cdot 10^2$ times the system's dynamical length scale (Equation 15), it is clear that near merger, a much more robust approach is necessary.

[14] See page 239 of [15].

2.3 Numerical Relativity

Perturbative approaches to solving Einstein's equations inevitably fail to give accurate physical descriptions when applied outside of their valid regions. Therefore, in order to accurately describe relativistic systems in all regimes of gravity, a general method of solving the full Einstein's equations is required. As there is no general analytic approach for solving Einstein's nonlinear equations, computer based *numerical* approaches have prevailed. This so called *Numerical Relativity* is broadly defined by the collective computational frameworks seeking to evaluate Einstein's equations in general regimes.

While Numerical Relativity contains many sub fields[15], of the most studied is the Numerical Relativity of binary black hole coalescence[16]. For example, Figure (4) illustrates the regime of binary black hole coalescence where Numerical Relativity must be used in order to resulve the relevant physics. Figure (4)'s left panel illustrates the two black holes after they have formed a common apparent horizon, and Figure (4)'s right panel illustrates the late inspiral-merger gravitational waveform corresponding to this period.

Towards the modeling of such waveforms, in this chapter we will briefly overview the elements of Numerical Relativity that are most pertinent to evaluation of binary black hole coalescence simulations, and their related post-analysis. Specifically, the operational structure of Numerical Relativity will be reviewed under the framing of Georgia Tech's MAYA Numerical Relativity code, and pertinent limitations will be outlined.

2.3.1 The 3+1 Formalism

In broad terms, a binary black hole simulation is an operation that acts on the binary system's initial conditions (*i.e.* the initial data), applies Einstein's equations under a convenient *formalism*, and then outputs the evolution of both the space–time and the black hole trajectories[17]. But while Einstein's equations, given by Equation (5), are very compactly written, they are not immediately amicable to being solved numerically. First, one must

[15] See reference [28] for a review of subtopics.
[16] For a detailed review, the author refers the reader to reference [29, 30, 31, 32].
[17] See reference [33] for a recent review.

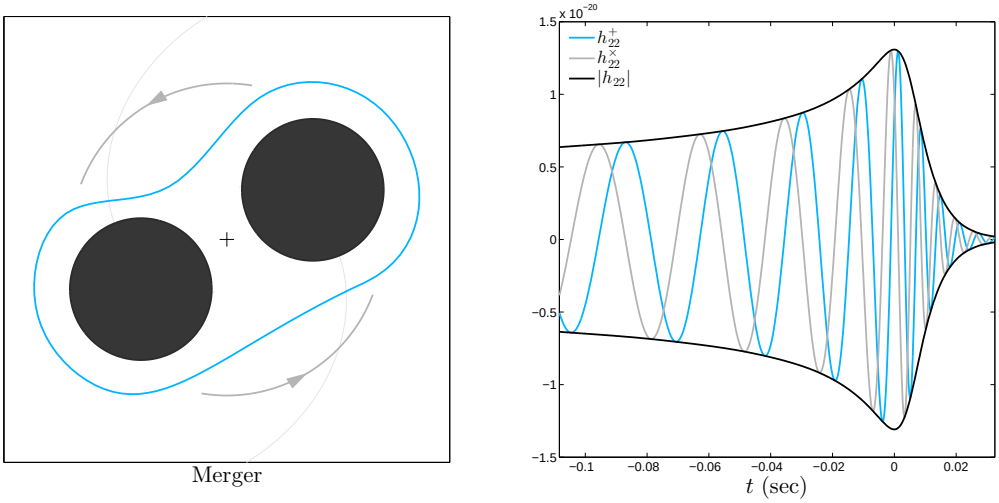

Figure 4: Black Hole merger for a 1:1 mass ratio, initially nonspinning black hole binary having initial total mass of 100 $M_\odot$, and observed at $r = 100$ Mpc. *Left*: A qualitative schematic of the binary black hole configuration. The black hole's apparent horizon is shown by the blue curve. *Right*: Here we see the analogous gravitational wave emission in physical units. This waveform was calculated using the Georgia Tech Maya code [2].

clarify what it means for a physical system to evolve when space and time are coupled. This clarification is most commonly provided by recognizing that a 4–dimensional space may be organized by a *foliation* a 3–dimensional space–like[18] hypersurfaces, *plus* a 1–dimensional time–like[19] dimension. This "3+1" split of General Relativity of enables Equation (5) to be projected (Equation 36) into its components that are parallel, perpendicular and oblique to the space–like hypersurfaces. This split, in addition to physical constraints (*e.g.* conservation of energy and momentum) enables Einstein's equations to be written in a way that can be numerically integrated. The basic way of writing down Einstein's equations in this manner is called the ADM formalism after Richard Arnowitt, Stanley Deser and Charles W. Misner [34]. But, as the ADM formalism is plagued by numerical instabilities, the related but numerically stable BSSN formalism[35] is in common use. In practice, the Georgia Tech Numerical Relativity group executes this formalism via the proprietary "Maya" code, which operates under a version of the Einstein Toolkit applied programming

[18]Equation (1) when $\Delta x^{(0)} = 0$
[19]Equation (1) when $\Delta x^{(1)} = \Delta x^{(2)} = \Delta x^{(3)} = 0$

interface (API), which is itself based upon the Cactus API [2, 4, 5, 6, 7].

2.3.2 Numerical Relativity's Inputs and Outputs

With an effective implementation of the $3 + 1$ formalism in hand, what remains is an "initial value problem". In other words, the physical system is defined by its initial conditions (such as initial positions, velocities, spins, and the dynamically related values of mass and spatial curvature), and the application of Einstein's equationss determines how these conditions evolve in time. However, as these conditions must satisfy both Einstein's equations and the aforementioned physical constraints, the resulting initial data problem is nontrivial, but manageable by applying the appropriate transformations to the space–like hypersurface (See [36] for a topical review).

Inputs. In an operational, but oversimplified way, these initial conditions are tightly constrained by the system's initial parameters, which effectively serve as the "inputs" to a Numerical Relativity simulation[20].

These initial parameters fall into two categories: intrinsic and extrinsic. On one hand, here, we will consider the extrinsic system parameters to be those that do not *uniquely* constrain the dynamics of the system. In the case of binary black holes, the extrinsic parameters are the distance from the observer to the source, r, the initial phase of the gravitational wave signal, $\Delta\phi_0$, as well as the observation period, $t = \Delta t_{\rm ret.} + t_{\rm initial}$. On the other hand, the *intrinsic* parameters uniquely constrain the physical system throughout the evolution of the simulation. For a binary black hole system, the intrinsic parameters include the black hole masses, m_1 and m_2, their momentum vectors, $\vec{P}_1^{\,\rm initial}$ and $\vec{P}_2^{\,\rm initial}$, as well as their spin vectors $\vec{S}_1^{\,\rm initial}$ and $\vec{S}_2^{\,\rm initial}$. As each vector has three components, there are 14 intrinsic parameters that define the type of binary black hole simulation being considered.

However, in practice, only subsets of this space are considered. For example, here, our interest in quasi–circular binaries (with $\vec{P}_1^{\rm initial} = -\vec{P}_2^{\rm initial}$) is prompted by the preferential radiation of orbital eccentricity [18, 19, 20, 21, 36]. Under this *class* of system, the initially

[20] The constraint is not exact as the nonlinearity of Einstein's equations prevents an exact solution.

non–spinning cases, with $\vec{S}_1^{\rm initial} = \vec{S}_2^{\rm initial} = 0$, are of the simplest, as they may be parameterized by only m_1 and m_2. However, as the amplitude of gravitational radiation scales directly with the total mass, $M = m_1 + m_2$, only the system's symmetric mass ratio[21], $\eta = \frac{m_1 m_2}{M^2}$, is need to constrain the gravitational radiation's morphology (e.g. Equation 44). For this reason, at least in the scope of Numerical Relativity, M, as defined by the ADM formalism, may be treated as an effectively extrinsic parameter, and is often set within the code to be unity. Similarly, in–code unit scalings are such that $G = c = 1$.

Importantly, as the initially non–spinning cases demonstrate, different initial "parameter classes" of binary black hole systems may be defined by considering subsets of the larger 14 dimensional parameter space. This point is central to the systematic analysis of Numerical Relativity's outputs, and related applications to data analysis, post experimental detection.

Outputs. The outputs of Numerical Relativity simualtion, in principle, may include every aspect of the numerical evolution; however, here, the most relevant outputs result from the extraction of gravitational radiation. Specifically, the most commonly used method for extracting gravitational radiation derives from the so called Newman–Penrose formalism[37, 38, 39], under which the gravitational wave strain is written in terms of the Weyl scalar, ψ_4, as

$$\boxed{H \;=\; h_+ - i h_\times \;=\; -\int_{-\infty}^{t}\int_{-\infty}^{t'} \psi_4 \, dt'' dt' \; .} \tag{45}$$

In Equation (45), ψ_4 is effectively the output of Numerical Relativity simulation (we shall see shortly that its multipole moments are actually output), and H, or rather $h+$ and $h_\times$, are the physical observables of interest. Furthermore, Equation (45) together with the spin weighted harmonic decomposition given by Equation (42), motivate output of the spin -2 spherical harmonic multipoles of ψ_4 (a.k.a. the ψ_4 "modes"):

$$\boxed{\psi_4(r,\theta,\phi,t) = \frac{1}{r}\sum_{l=2}^{\infty}\sum_{m=-l}^{l} \psi_{lm}(t) \; {}_{-2}Y_{lm}\left(\theta,\phi\right) \; .} \tag{46}$$

[21]The naive mass ratio, m_1/m_2, may also be used for conceptual clarity; however, η is of more practical use due to its appearance in the Post-Newtonian approximation (Equation 44), as well as its invariance under the exchange of m_1 and m_2.

Note that in Equation (46) we have chosen to write the $1/r$ dependence explicitly. In doing so, we highlight the independence of each ψ_{lm} on the *numerical extraction radius* (i.e. the observation distance), r. However, in practice, ψ_{lm}/r is the relevant, lowest level output of binary black hole simulation. Moreover, just as in Equation (43), we have that

$$\psi_{lm}(t) = r \int_{\Omega} \psi_4(r,\theta,\phi,t) \, {}_{-2}\bar{Y}_{lm}(\theta,\phi) \, \mathrm{d}\Omega \, . \tag{47}$$

With the above overview in mind, the utility of Numerical Relativity as a tool for investigating strong field gravity can, in effect, be treated as non–trivial mapping between binary black hole system parameters, and the time dependence of the corresponding gravitational waveforms. It is from this perspective that the post-simulation analysis, and modeling of gravitational waveforms begins. However, concurrently, it is important to note the current limitations of Numerical Relativity.

2.3.3 Numerical Relativity's Limitations

While numerical techniques have been used since the 1970s to investigate black hole solutions to Einstein's equations (*e.g.* [40, 41]), it was only as recently as 2005 that simulations were capable of evolving the general two black holes through merger [42, 43, 44]. Prior to that time, challenges to successful evolution of Einstein's equationss included finding a numerically stable formalism, calculating reasonably accurate initial data, and devising a host of other techniques (such as gauge choices) to promote the stability of simulations in different regimes. Although each of these challenges has been resolved to some large extent, there remain adjacent aspects of Numerical Relativity that limit both its numerical and physical accuracy. The most prominent of these limitations relate to numerical noise, long simulation times, and uncertainty about where and how many simulations to run.

Spurious Radiation. Our inability to generate exact initial conditions results in an unavoidable relaxation period at the beginning of each simulation. During this period, non physical gravitational radiation propagates through the space time until it either leaves the computational grid, or is diminished in amplitude after many interactions over the

computational domain. In the preponderance of scenarios, the timescale over which this non-physical radiation dominates is much smaller than those of interest. For the extracted gravitational waveforms, the result is a period of "spurious" or "junk" radiation at the beginning of each waveform time series. Independently, for all outputs of the simulation, finite resolution effects incur a "noise floor", below which all data is dominated by irregular, non-gaussian fluctuations.

Simulation Time, and Convergence. The ability to stably evolve Einstein's equations is, in part, dependent on the computational grid being sufficiently fine. This is to resolve the relevant scales while simultaneously maintaining physical constraints. However, as Numerical Relativity generally seeks to evolve a vast range of systems across parameter space, there is a tenuous interplay between the input spatiotemporal resolution, and the time required to complete the desired simulation. Naturally, the higher the resolution, the higher the number of computations per iterations, and therefore the longer a simulation will take to complete. Moreover, while there may be range of resolution schemes over which the system evolves stably, stable evolution does not guarantee physical convergence of the result. For these reasons, an often time consuming comparison between simulations of different resolution is needed to verify that the calculated behavior is sufficiently near the "infinite resolution", physical, regime. While, in some cases, running three or more simulations with the same physical parameters, but different resolutions may allow this sort of "convergence testing", in general, computational resources are too scarce to repeat this exercise throughout even the most scant parameter ranges. As a result, when simulating a 1D subset of the parameter space, at least one convergence test is necessary to characterize the related gravitational wave data.

Simulation Placement. Thankfully, the convergence testing discussed in the preceding paragraph does not generally need to be done exhaustively. This is because perturbation theory is most often applicable in regimes of small and/or disparate length scales, while full Numerical Relativity is largely concerned with scenarios of large and similar length

scales. Even so, convergence testing, as well as the resulting conclusion about a simulation's resolution, place real world constraints on how many simulations may be evaluated throughout any region in parameter space. Therefore, as numerical relativists explore increasingly high dimensional cases, time and computational resources limit the rate at which they may evaluate simulations, and thereby model the related waveforms. This poses a optimization problem over where to place Numerical Relativity simulations, and how many to place there. See Chapter (7) for an expanded discussion.

Importantly, despite all of its limitations (Section (2.3.3)), Numerical Relativity remains extremely useful to gravitational wave astronomy: *It's gravitational waveforms have been quality checked across different code implementations, and agree to high precision [45, 46]. In tandem, the physical accuracy of these waveforms has made them a large and significant participant in the build up to detection [45, 47].* Moreover, as the momentum of research points in the direction of improvement, the limitations listed above do provide fertile ground for advances at the intersection of Numerical Relativity and detection oriented data analysis. Under the scope of this thesis, the above intersection will be referred to *Numerical Relativity Data Analysis*. As we will see in the next chapters, gravitational wave modeling is required in order to efficiently interface Numerical Relativity waveforms with detection and post–detection analysis routines.

2.4 Gravitational Ringdown

In Section (2.1), we learned that perturbation techniques can be used in order to characterize the gravitational radiation due to binary black hole coalescence in the regime where the two objects are weakly bound by gravity. In Section (2.2), we learned that, as the distance between the two compact objects shrinks, and the strength of their gravitational attraction grows, this perturbative, Post-Newtonian was no longer capable of accurately describing the key physics. As a result, Numerical Relativity (Section 2.3) needs to be employed to calculate gravitational wave emission in the late inspiral and merger regimes. However, it is important to note here that, in addition to Post-Newtonian's inspiral, there

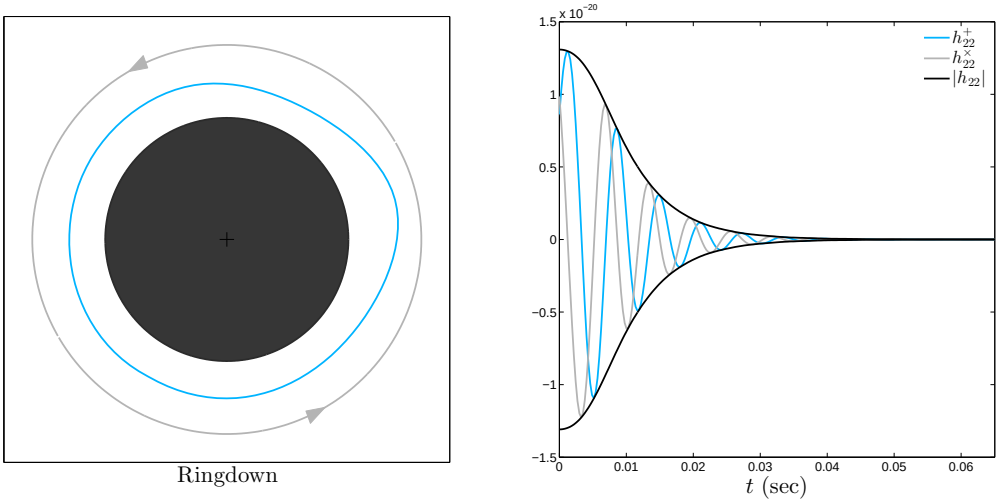

Figure 5: Black Hole "ringdown" for a 1:1 mass ratio, initially nonspinning black hole binary having initial total mass of 100 $M_\odot$, and observed at $r = 100$ Mpc. *Left*: A qualitative schematic of the final black hole configuration *ringdown*. The black hole's apparent horizon is shown by the blue curve. *Right*: The analogous ringdown gravitational wave emission in physical units. The corresponding simulation was performed with the Georgia Tech Maya code[2].

is yet *another* perturbative regime of binary black hole coalescence where analytic solutions are tractable.

In particular,after the two black holes collide, they form a single, perturbed, remnant black hole. Under Equation (5), the dynamics of this black holes distortions result in gravitational radiation that is reminiscent of the *ringing down* of a struck bell. Figure (5) illustrates this regime for a representative, equal mass binary observed along the center normal to its orbital plane. In particular, the right panel illustrates that far to the right of merger, the radiation is exponentially damped. In fact, the theory of perturbed black holes – which was spurred by the seminal work of Vishveshwara [41] and then put on rigorous theoretical footing by Teukolsky [48] – describes gravitational ringdown as a sum of decaying sinusoids.

As will be discussed in detail in Chapter (5), each term in the sum corresponds to a single "quasi-normal mode", and is related to the spherical harmonic multipoles discussed in Sections (2.2-2.3.2). Because these quasi-normal modes are constrained by the final mass and spin of the remnant black hole, this final stage of binary black hole coalescence

offers yet another analytic insight into the properties gravitational radiation from compact binaries. Consequently, as will be expanded upon in Chapter (5) where the author presents his central results, ringdown radiation enables potentially viable methods for extracting physical information from gravitational wave signals.

ON GRAVITATIONAL WAVE MODELING: NUMERICAL RELATIVITY DATA ANALYSIS, THE EXCITATION OF KERR QUASINORMAL MODES, AND THE UNSUPERVISED MACHINE LEARNING OF WAVEFORM MORPHOLOGY

PART II

Data Analysis and Gravitational Wave Modeling

by

Lionel London

Chapter III

NUMERICAL RELATIVITY DATA ANALYSIS

Numerical Relativity Data Analysis (NRDA) refers to the processing of Numerical Relativity data, with the goal of informing detection and post–detection information pipelines. Less broadly, the phrase encapsulates a series of operations that take in simulated gravitational waveforms, and then output *data* and *analysis components* that can then be applied to experiment based analysis. At the lowest level, the *data* output is gravitational wave strain, which must be calculated from ψ_4 according to Equations (45-46). Given the gravitational wave strain, the functional motive of NRDA is to develop *analysis components* that facilitate information extraction in detection scenarios. In this chapter, we will briefly review the transition between *data* and *analysis components* in the context of my contributions to Georgia Tech's NRDA activities [47, 45, 13].

3.1 Tools for Numerical Relativity Data Analysis

The Georgia Tech Numerical Relativity group has amassed more than *1,900* binary black hole simulations. Each represents a point in the effectively 13 dimensional initial parameter space (See Section 2.3). Given such a large collection of Numerical Relativity waveforms embedded within such a highly dimensional space, it is a non-trivial computational exercise to catalog, reference, analyze, and conceptually render data in a way that elucidates the desired science. As a result, each Numerical Relativity group must develop in–house analysis tools that facilitate the answering of ongoing research questions. Here, I outline, in broad strokes, an applied programming interface (API) that I have developed (mostly in MATLAB) for the Georgia Tech Numerical Relativity group's NRDA activities. This *"NRDA–Toolkit"* is foundational to all of this thesis' key results.

3.1.1 The NRDA–Toolkit

The power of any API is arguably derived from its ability to handle abstraction: the representation of general ideas rather than specific jobs. It is under this philosophy that the NRDA–Toolkit is structured to allow a hierarchical flow of information, with very selective attention paid to specific tasks. It is assumed that user's most basic object of interest is the Numerical Relativity simulation, rather than the Numerical Relativity waveform. This underlying principle is key, as it facilitates the simultaneous investigation of physics parameters (initial and final), and waveform morphology. However, in order to fully connect the output of Numerical Relativity to data analysis components, the above *low–level* aspects of the toolkit must be utilized the within NRDA–Toolkit's *high–level* routines.

3.1.1.1 Low–Level Interface

Specifically, at the lowest level, the idea of a simulation is encapsulated within a class[1] whose attributes include a system's initial and final parameters, as well as all bookkeeping information needed to readily access simulation output. A *Simulation Catalog* of such objects is compiled, and then stored for fast referencing. In contrast to an "on the fly loading" approach (the grey dashed line in Figure 6), where the user must keep track of every data directory in use, this catalog based scheme allows users to select simulations based on physical identifiers, without having to keep up with where the simulation is, and how it is stored. While ostensibly trivial, this property significantly simplifies ones ability to simultaneously manage simulation attributes, and waveform data.

For example, Figure (6) outlines the prototypical flow of information that occurs during the analysis of Numerical Relativity data. Boxes A and B follow Section (2.3.2)'s description of Numerical Relativity's inputs, $\boldsymbol{\lambda} = \{\frac{m_1}{m_2},\ \vec{P}_1,\ \vec{P}_2,\ \vec{S}_1,\ \vec{S}_2\}$, and outputs, ψ_{lm}. Boxes C and D represent the connection between cataloging[2] and parameter based searching. In box D, the `options` input is assumed to be a cell array containing the search query. For

[1] Here, I assume that the reader is familiar with object oriented programming.

[2] Note that cataloging need only be done once, prior to the execution of the main workflow.The catalog need only be recompiled of new simulations are added.

example, `Y = sc_search('q',[1 10])` is equivalent to setting `options = {'q',[1 ... 10]}`, as each case will result in the search algorithm returning all simulations with mass ratio, $q = m_1/m_2$, from 1 to 10.

It is important to note that the information held by each unique simulation object, `Y`, is inherited by its derivative objects. In box E, we see the primary example of this hereditary structure in the *standard waveform object*, `y`, which holds various time series information for a specific ψ_{lm} multipole (Equation 47). Specifically, `y` is capable of referencing all of the information describing the simulation it belongs to via the `y.init_info` reference. It is in this way that the NRDA–Toolkit's structure greatly simplifies connections between simulation parameters, $\boldsymbol{\lambda}$, and waveform morphology, ψ_{lm}. Alternatively, one may follow the path of box F, and use the results of the catalog search to investigate relationships between initial binary parameters, and final black hole parameters.

3.1.1.2 High–Level Interface

As in the case of most programming interfaces, the propagation of low–level information mentioned above empowers the user to construct high–level abstractions. Here, the most useful of these abstractions are stored as functions, such as those listed in Figure (6)'s box H. The most important of these functions is `y_strain()`, which calculates of gravitational wave strain via Equation (45). Predominantly, the other functions take strain as an input in some form: time, or frequency domain. One notable exception is `y_recompose()`, which calculates either $rH(t, \theta, \phi)$ (via Equation 42), or $r\psi_4(t, \theta, \phi)$ (via Equation 46). In conjunction, all of these functions facilitate the conversion of the ψ_{lm} into experiment oriented statements, such as signal detectability (via `snr(h)`), or parameter similarity (via `match0(h1,h2)`). The utility and significance of these functions will be expended upon in Section (3.2).

Lastly, of primary interest to this thesis is the intermediate course, signaled by box I, whereby the simulated gravitational waveforms are used to develop models, h_{lm}^{model}, that take in initial parameters, $\boldsymbol{\lambda}$, and output a waveform $h_{lm}(t) = h_{lm}^{\text{model}}(\boldsymbol{\lambda})$. An expanded outline of this topic will given in Chapter (4).

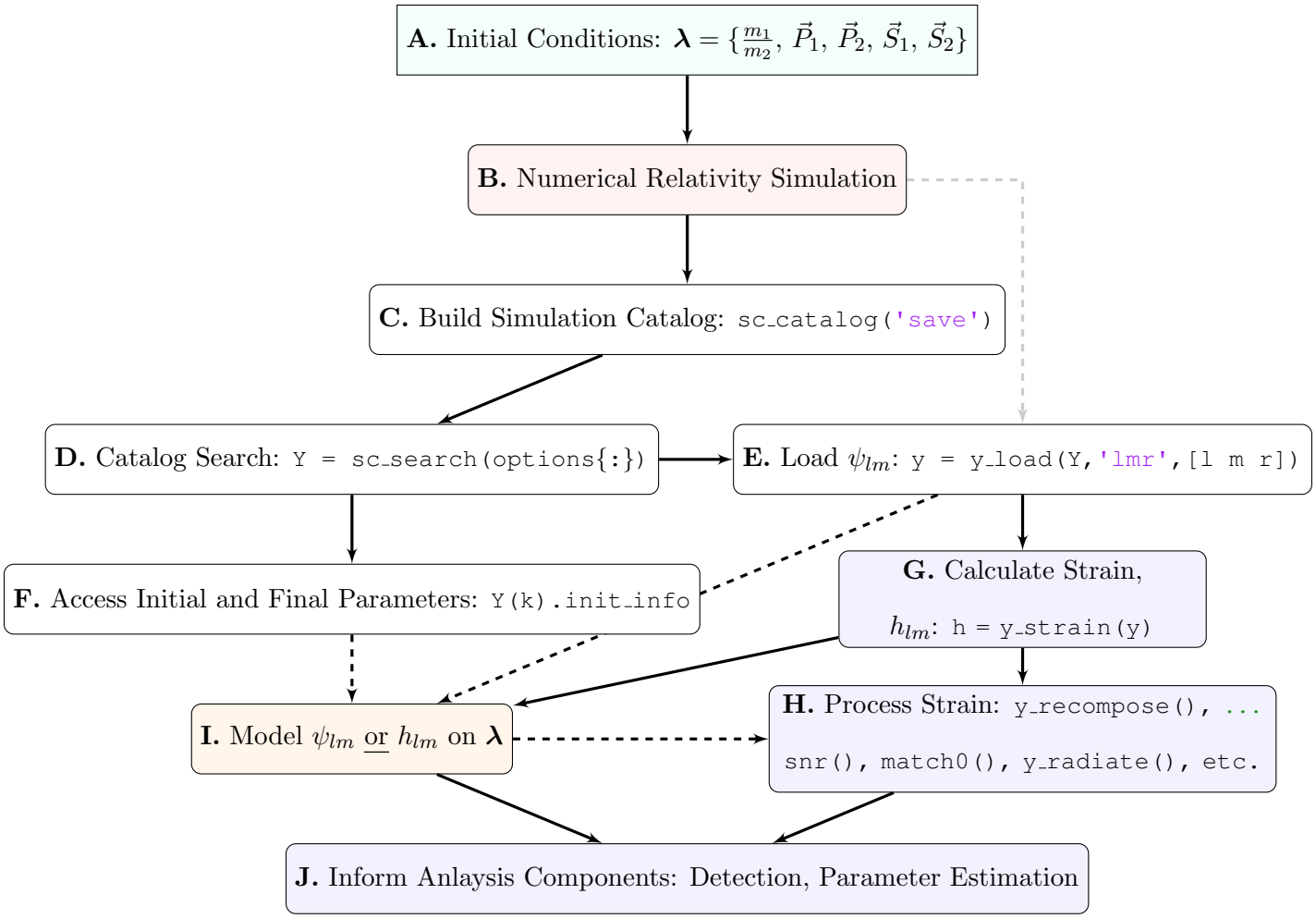

Figure 6: NRDA–Toolkit structure: Dashed lines denote optional paths of information flow. The low level operations are held in white boxes, while the high level operations are in blue boxes. Just as in box B, gravitational waveforms are both processed and created in box I. Box J encapsulates the highest level of abstraction, in which the output of Numerical Relativity simulation is rendered in a manner that informs experiment data analysis.

3.2 Applications

In this section we will review some of the primary high–level components of the NRDA–Toolkit. Particular focus will be placed on calculations of strain, match and signal to noise ratio (SNR), as they are the most pertinent to the results of this thesis. Additional focus

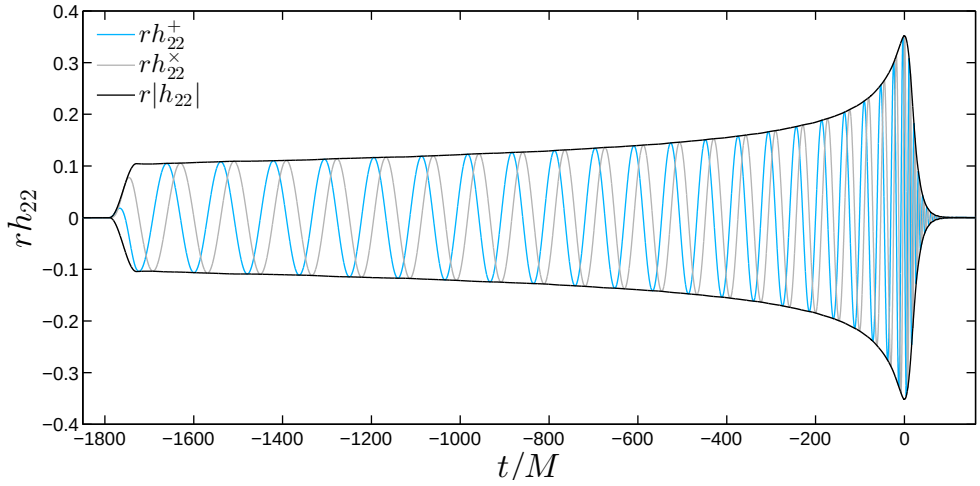

Figure 7: The $l = m = 2$ strain multipole moment for a 2:1 mass ratio, binary with spins that are aligned with the orbital angular momentum, and are of like magnitude $\chi_1 = \chi_2 = |\vec{S}_1|/M^2 = 0.6$ (calculated with the GT Maya Numerical Relativity code [2]).

will be placed on the process of attaching Post-Newtonian waveforms to their Numerical Relativity counterparts (*i.e.* PN-NR Hybridization). Each of these tasks is important for their role in scientific discussions about waveform accuracy, signal detectabilty, and parameter estimation. In particular, the components presented below have been used to contribute to the NINJA and NRAR collaborations [45, 47]. Concurrently, the strain calculation and match calculations are the most pertinent to this documents as whole.

3.2.1 Strain Calculation

As described in Section (1.2), and expanded upon in Section (2.3.2), gravitational wave strain is the primary observable of interest to gravitational wave experiment. However, as Numerical Relativity's primary output is the Weyl scalar ψ_4's spherical multipole moments, at least one intermediate step is required in order to proceed with NRDA. This step is the double time integration of ψ_4 according to Equations (45-47):

$$H \;=\; h_+ - ih_\times \;=\; -\int_{-\infty}^{t}\int_{-\infty}^{t'} \psi_4(t'')\,dt''dt' \;=\; -\frac{1}{r}\sum_{l,m}\int_{-\infty}^{t}\int_{-\infty}^{t'} \psi_{lm}(t'')\,dt''dt'. \qquad (48)$$

As one typically handles ψ_{lm}, the multipoles of strain, h_{lm}, are calculated in practice. If follows from Equation (43) and Equation (48) that

$$h_{lm}(t) \;=\; -\frac{1}{r}\int_{-\infty}^{t}\int_{-\infty}^{t'} \psi_{lm}(t'')\, dt''dt'. \tag{49}$$

The above equation suggests that one need only apply a discrete quadrature procedure, such as the "trapezoidal rule", to evaluate the double integrals. The existence of numerical noise (Section 2.3.3) however, prevents this naive approach from yielding physical results. In particular, while the magnitude of numerical noise if typically $\sim 10^{-5}$ times smaller than the peak amplitude in a numerical waveform, the noise has the quality of not being centered about zero. Therefore, when integrating, one effectively acts upon $\psi_{lm}(t) + \varepsilon(t)$, where $\langle\varepsilon\rangle_t \neq 0$. Consequently, after one time integration, one observes a non-physical linear drift, proportional to $t\,\langle\varepsilon\rangle_t$ and, after two time integrations, a parabolic drift, proportional to $t^2\,\langle\varepsilon\rangle_t$.

In order to circumvent this spurious effect, it was recognized in reference [49] that the most aberrant numerical noise lives at frequencies much lower than those related to the physical data. Put another way, it is this low frequency noise that contributes the most to the non-zero mean of $\varepsilon(t)$, which is given by $\langle\varepsilon\rangle_t$. This observation was coupled with the fact that one may perform time domain integration on the waveform's Fourier transform. Specifically, if Fourier Transform of $\psi_{lm}(t)$ is $\mathcal{F}[\psi_{lm}](\omega) = \int_{-\infty}^{\infty}\exp(i\omega t)\psi_{lm}(t)\mathrm{d}t$, then integration by parts[3] gives

$$\mathcal{F}\left[\int_{-\infty}^{t}\int_{-\infty}^{t'} \psi_{lm}(t'')\, dt''dt'\right](\omega) \;=\; (i\omega)^{-2}\,\mathcal{F}[\psi_{lm}](\omega) \tag{50}$$

Here, the inverse Fourier transform can be used to recover $\int_{-\infty}^{t}\int_{-\infty}^{t'}\psi_{lm}\, dt''dt'$. Consequently, as we wish to overlook the aberrant, low frequency noise, Equation (50) is handled in two pieces. In the first piece, ω is less than some *fixed* value, ω_0, which is the lowest physical frequency expected in the waveform. Here, $(i\omega_0)^{-2}$ is used in Equation (50), rather than $(i\omega)^{-2}$. In the second piece, normal frequency domain integration is applied (i.e. Equation 50 with no alteration). It is important to note that the frequency parameter, ω_0 may

[3]The physical boundary conditions, $\psi_{lm}(-\infty) = \psi_{lm}(\infty) = 0$, are also used.

be easily determined from the inspiral phase of ψ_{lm}. As can be deduced from Equation (44), ω_0 should be approximately equal to the waveform's instantaneous frequency at the start of the simulation. In total, these ideas compose the "Fixed Frequency Integration" method that is implemented in `y_strain()` [49].

To briefly illustrate the utility of `y_strain()`, let us consider the instance where one wishes to calculate the strain of a $q =_{\text{def.}} \frac{m_1}{m_2} = 2$ mass ratio binary, with spins that are aligned with the orbital angular momentum, and are of like magnitude $\chi_1 = \chi_2 = |\vec{S}_1|/M^2 = 0.6$. The MATLAB code for this calculation is given below.

```
% Simple example of y_strain() usage: Find 2:1 mass ratio, spin aligned
% simulation, and then calculate hlm = h+ - i*hx. Units: M_code=G=c=1.
% by llondon2/6'15
close all; clc;
% [A] Find an Numerical Relativity Simuulation
Y = sc_search('q',2,'spin_aligned','chi1_val',0.6,'verbose');
% Multiple simulations are found. Keep the first simulation in the list,
% which is set to be that with the highest resolution.
Y = Y(1);
% [B] Load a single Psi4lm multipole
l = 2; m = 2;    % the spherical harmonic indeces
r = 75;          % r is the extraction radius (units:M_code)
y = y_load(Y,'lmr',[l m r],'verbose');
% [C] Calculate the corresponding strain multipole moment using y_strain.
h = y_strain(y);
% Plot the result.
figure; hold on; plot( h.t_raw, h.Yp_raw ); plot( h.t_raw, h.Yx_raw )
```

The above code corresponds Figure (7), which shows the plus and cross polarizations for the related $h_{22}(t)$. Note that the spurious radiation discussed in Section (2.3.3) has been automatically located and removed. After its calculation, the gravitational wave strain is perhaps most commonly used as an input for the match and/or SNR calculations.

3.2.2 Signal to Noise Ratio and Match

Any realistic detector will have noise. But even for the most current gravitational wave detectors such as Advanced LIGO (Adv. LIGO), this experimental noise is expected to be much larger than the amplitude of likely gravitational wave signals. However, this apparent difficulty does not prevent detection ***if*** the morphology of possible signals is known *a priori* [50, 15, 51, 52, 53]. To motivate this idea, let us briefly consider the somewhat idealized detector output[4], $s(t)$, given by the sum of the gravitational wave strain, $h(t)$, and the noise, $n(t)$. In elaborating on the above statement, we will encounter and give basic example for the primary ideas of this section: *signal to noise ratio* (SNR), and *match*.

We begin by noting that, for sufficiently long observation periods, we are able to consider the output in the frequency domain:

$$\tilde{s}(f) \;=\; \tilde{h}(f) + \tilde{n}(f)\;. \tag{51}$$

With this data in hand, the central analysis task is to *filter* out the desired signal from the noise. The simplest way to approach this goal is to seek some linear operation, $\hat{F}$, such that $||\hat{F}\tilde{s} - \tilde{h}||$ is minimal. A widely used, and well investigated solution to this optimization problem is given by the Wiener filter[5], also known as the *matched filter*, where

$$\begin{aligned} \hat{F}\tilde{s} \;&\underset{\text{def.}}{=}\; \int_{-\infty}^{\infty} \frac{\tilde{s}(f)\,\tilde{g}^{*}(f)}{(1/2)S_n(f)}\,\mathrm{d}f \\ &=\; 4\mathrm{Re}\int_{0}^{\infty} \frac{\tilde{s}(f)\,\tilde{g}^{*}(f)}{S_n(f)}\,\mathrm{d}f\;. \end{aligned} \tag{52}$$

In Equation (52), $\tilde{g}^{*}(f)$ is the complex conjugate of $\tilde{g}(f)$, and $S_n(f)$ is the positive valued power spectral density (PSD) of the noise, defined by twice the fourier transform of $n(t)$'s ensemble averaged[6] auto-correlation function,

$$S_n(f) \underset{\text{def.}}{=} 2\int_{-\infty}^{\infty}\left(\lim_{T\to\infty}\frac{1}{T}\int_{-T}^{T} n(\tau+t)\,n(\tau)\mathrm{d}t\right)e^{2\pi i f\tau}\mathrm{d}\tau\;. \tag{53}$$

[4]Here we assume a flat antenna pattern.

[5]The author refers the motivated reader to reference for a full development of Equation (52) [50, 15, 53].

[6]Here we imagine that one is able to observe infinitely many realizations of the noise, and then compute the average the Fourier transform amplitude of each. If each realization is independent, then, as shown in Equation (53), the ensemble average is the time average.

Note that, in going from the first line of Equation (52), to the second, we have used a property of the Fourier transform on real valued function. Namely, as $s(t) \in \mathcal{R}$, $\tilde{s}(-f) = \tilde{s}^*(f)$. Lastly, in practice, Equation (52) is identified with a scalar inner–product, defined by

$$(a|b) \;=\; \int_{-\infty}^{\infty} \frac{\tilde{a}^*(f)\,\tilde{b}(f)}{S_n(f)}\,\mathrm{d}f \;. \tag{54}$$

Although a formal derivation of Equation (52) is not appropriate here, the strength of the Wiener filter may be seen by the inspection of two cases: $\tilde{g}(f) = \tilde{h}(f)$, and $\tilde{g}(f) \neq \tilde{h}(f)$.

Signal to Noise Ratio. First, if $\tilde{g}(f) = \tilde{h}(f)$, then the integrand of $(h|h)$ is positive for all f, and largest when the PSD of the noise is smallest. Simultaneously, the integrand of $(h|n)$ is not positive for all f, and is thus prone to *deconstructive interference*[7]. Importantly, it is for this reason that information about the gravitational wave signal may be exacted, even when its typical amplitude is much smaller than the noise.

More formally, we may use the above ideas to more carefully consider "signal size to noise size". Specifically, for $\tilde{g}(f) = \tilde{h}(f)$, it may be shown (as in reference [15]) that the weighted average of $\tilde{h}(f)$ (via Equation 52), divided by the root-mean-square value of the noise (also via Equation 52), is equivalent to $\frac{(s|h)}{\sqrt{(h|h)}}$, and gives the appropriate SNR for this problem. In this setting, the SNR is typically written as

$$\rho = \frac{(s|h)}{\sqrt{(h|h)}} \approx \sqrt{(h|h)}\;. \tag{55}$$

The "$\approx$" in Equation (55) becomes an "$=$" when the observation period is long enough for $(h|s) = 0$. Looking back to Equation (52), the placement of $S_n(f)$ in the denominator of Equation (52) is appropriate as it effectively scales information by the noise.

It is important to note, however, that the above discussion overlooks an inherent limitation. In particular, it assumes that, given detector output, $s(t)$, we not only have prior knowledge about the gravitational wave signal, $h(t)$, but that we have *exact* knowledge about it's morphology. This scenario is clearly ideal, as we won't know ahead of time exactly what the signal looks like, or what parameters its astrophysical system has. We can only make educated, model guesses.

[7] Although the noise may be centered about zero, $\hat{F}\tilde{n}$ is not trivially zero for finite observation times.

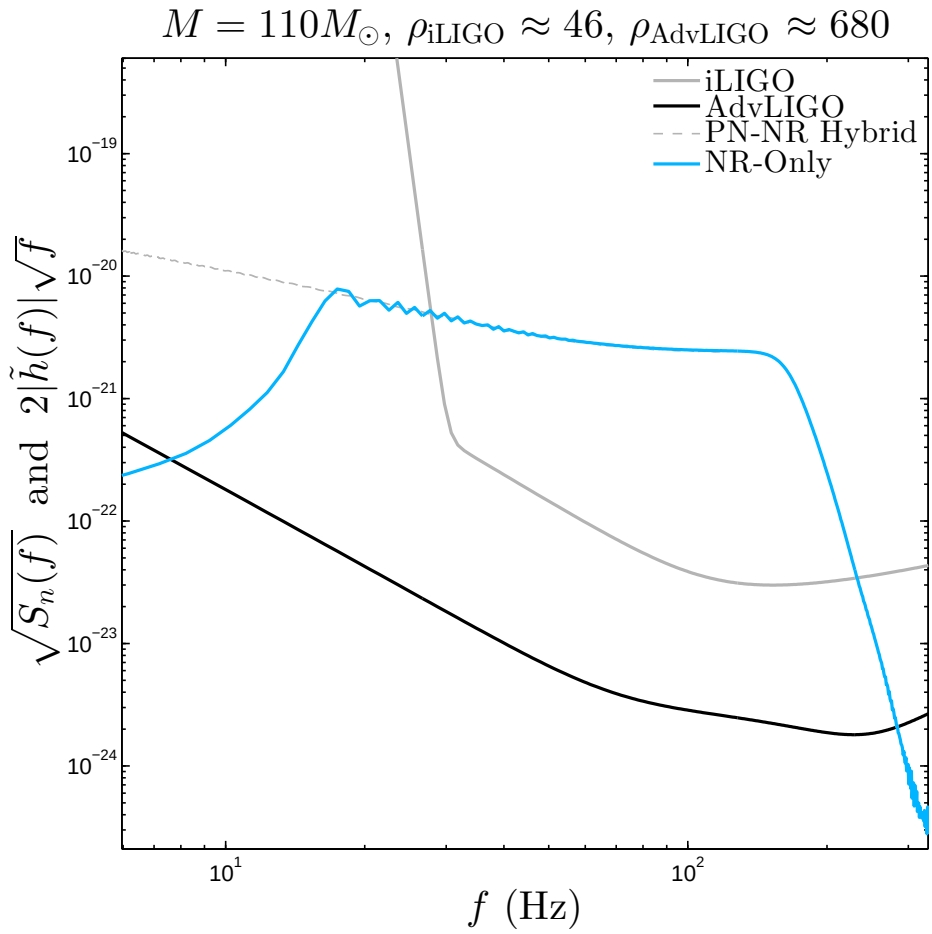

Figure 8: The signal to noise ratio, and "noise curve plot" for a 1:1 mass ratio, nonspinning binary. The Numerical Relativity (NR) waveform was calculated with the GT Maya NR code [2], and the post analysis was performed with the author's NRDA–Toolkit. As discussed in Section (3.2.3), the dip in the NR-Only curve after 20Hz results from the finite initial separation of the binary black holes. This results in a non-physical bias for the value of $\rho_{AdvLIGO}$ which depends on the total mass scaling. One way to overcome this limitation is to carefully attach information from Post-Newtonian (PN), as shown by the PN-NR Hybrid curve.

Match. To briefly touch upon the problem of not knowing the $\tilde{h}(f)$ prior to detection, let us return to our consideration of Equation (52), but now with $\tilde{g}(f) \neq \tilde{h}(f)$. In particular, let's imagine that $\tilde{h}(f)$ is an astrophysical waveform from a binary black hole system of

unknown initial parameters, $\boldsymbol{\lambda}_0$, and that $\tilde{g}(f)$ is a model waveform, or *template*, with trial parameters, $\boldsymbol{\lambda}$. In this setting, we are interested in determining which parameters $\boldsymbol{\lambda}$ maximize $(g|h)$. This goal is simplified by noting that the morphology of the signals is more important than their constant amplitude scaling. With this in mind, the *match* is defined on normalized waveforms (*i.e.* $(u|u) = 1$), and optimized over the extrinsic parameter of time and phase shift (See Section 2.3.2). For ease of reference, and using the notation given in Section (2.3.2), the author chooses to write the match as

$$\mu = \max_{\Delta T, \Delta\phi_0} \frac{(g|s)}{\sqrt{(s|s)\,(g|g)}} \,. \tag{56}$$

In practice, optimization over ΔT and $\Delta\phi_0$ can be performed simply by time-shifting in the frequency domain (*e.g.* via the Fourier transform), and then taking the absolute value of the total result [46]. However, when seeking the optimal[8] template for a given signal, one also needs to optimize over the waveform's intrinsic physical parameters. This optimization poses a computational problem whose complexity increases with the number of parameters being considered[9]. Notably, there is an active area of research with large intersections with gravitational wave modeling, that is devoted to devising ways of speeding up this, and related procedures (*e.g.* [54]).

Together, the SNR and match calculations are based upon Equation (54), and they are implemented in the NRDA–Toolkit as `snr()` and `match0()`, respectively. Despite the above discussion, in order to properly connect the theory oriented output of simulation with our experiment oriented discussion, one must choose a physical orientation of the binary black hole system relative to the detector, put the waveform in physical units, calculate strain, and then consider the match or SNR using a predetermined PSD. In the case of SNR, this process is briefly illustrated by the following MATLAB example.

Example. Here we consider the SNR calculation an equal mass non-spinning system. This system was chosen because it's SNR can be easily referenced externally [46]. While the first part of this example is nearly identical to the previous, `y_strain()` example, the

[8] Here, we mean "optimal" only in the sense of maximizing the match, not, for example, in the sense of identifying the true physical parameters of $\tilde{h}(f)$.

[9] In this setting, total system mass is kept as it determines the waveform's frequency scale; however, observation distance is not counted due to normalization.

key differences are that, here, we set the orientation of the detector relative to the physical system, and then we put the strain in physical units before calculating the SNR values. Figure (8) displays the related "noise curve" plot, along with the calculated values of the SNR for LIGO and the current, Adv. LIGO. The purpose of this plot is to visualize the SNR for a waveform at given observation distance and total mass. Note that, when plotted, both strain and the PSDs are scaled so that they have the same units. Moreover, note that while we have limited our current consideration to the most dominant $l = m = 2$, the example code may easily be modified to include additional multipole moments.

```
% Find 1:1 mass ratio, nonspinning simulation, define its physical
% properties, and then calculate its SNR. May be compared  with
% arxiv:0901.1628v2.
clear; close all; clc;
% ## Calculate strain ##
Y = sc_search('setname','hr-series','q',1,'nonspinning','verbose');
l = 2; m = 2;   % the spherical harmonic indeces
r = 75;         % r is the extraction radius (units:M_code)
y = y_load(Y(1),'lmr',[ l m r ],'verbose');
% [C] Calculate the corresponding strain multipole moment using y_strain.
h = y_strain(y);
% Set the orientation. Always do after strain calculation.
theta = 0; phi = 0; % "face on"
h = y_recompose(h,[theta phi]);
% ## Calcualte the SNR ##
M = 110;         % Total system mass in solar units
D = 100;        % Observation distance (Mpc) -- used for "1/r"
hf = Y_FFT(h);  % Calculate frequency domain waveform
% Convert the simulated strain to physical units
hf_phys = PHYS_Hf(hf,M,D);
% Retrieve the Detectors PSD evaluated on the waveform's frequency range
Sn = Noise(hf_phys.f, 'iligo');
% ## Plot the strain against the detector's PSD with like units ##
figure; hold on;
```

```
25 plot( hf_phys.f, 2*sqrt(hf_phys.f).*hf_phys.POW_RAW )
26 plot( hf_phys.f, sqrt(Sn), 'k' )
27 set(gca,'yscale','log','xscale','log')
28 % ## Calculate the SNR ##
29 rho_iligo = snr(hf_phys,'iligo'); % Initial  LIGO
30 rho_Advligo = snr(hf_phys,'advligo'); % Advanced LIGO
```

3.2.3 PN-NR Hybridization

It is noteworthy that the left hand side of Figure (8)'s NR-Only strain curve dips downward to the left of $f = 10$(Hz). This is a non-physical feature due to the simulation's starting the binary black hole system at a finite separation. Numerical relativists are largely forced to do this as a result of limited computational resources. Put simply, the larger the initial binary separation, the more time is need to evolve the system through merger. One practical consequence of this limitation is that gravitational waveforms from Numerical Relativity can only be used in the preceding analysis for total masses such that the nonphysical dip is "out of band". For example, in Figure (8), the dip occurs in a region where the LIGO's initial PSD[10] is much larger than the values expected by extending $|\tilde{h}|$ towards lower frequencies. While there are ongoing efforts to run longer binary black hole simulations more efficiently (e.g. [55]), one of the most established methods[11] for extending Numerical Relativity waveforms towards the Post-Newtonian regime is referred to as *hybridization*, or, more colloquially, stitching [59]. The immediate appeal of smoothly blending together Post-Newtonian and Numerical Relativity waveforms, is that it results in an a *full* picture of binary black hole dynamics. While this blending can simply be done in a way that optimizes how similar the Post-Newtonian and Numerical Relativity waveforms are in a chosen region of overlap, one must be wary systematic errors resulting from errors

[10] This is the PSD prior to the sensitivity upgrades that were completed in early 2015. The present detector is said to be "Advanced LIGO".

[11] Alternatively, there are "Effective One Body" (EOB) extensions of Post-Newtonian approximants (*e.g.* [56, 57, 58]) which, in practice, compete with hybrid waveforms (and models thereof). While there is no prevailing consensus over which is truly more effective, EOB waveforms are the more established, and widely used due to their relative.

in the Post-Newtonian approximation, the choice of blending region, and the details of the hybridization method [60, 61, 62, 58, 63, 64, 65]. Moreover, although consensus regarding the effectualness and practicality of these hybrib waveforms appears to be evolving within the gravitational wave community, they do represent an interesting tool by which the full dynamics of binary black hole coalescence can be interfaced with data analysis. In what follows, we will briefly review the process of hybridization, per the author's contribution to the NINJA-2 collaboration's seminal paper [50].

Most typically, hybridization uses least-squares fits to determine the extrinsic parameters for the Post-Newtonian waveform [66, 50, 46, 62]. This is accomplished by evaluating

$$\{\vec{u}^*, a^*\} = \underset{\{\vec{u},a\}}{\operatorname{argmin}} \int_{s_2}^{s_1} |a\Upsilon_{\rm PN}(s,\vec{u}) - \Upsilon_{\rm NR}(s,\vec{u}_0)|^2 \, {\rm d}s \tag{57}$$

where Υ represents waveform data relating to strain (*e.g.* $h(t) = h_+(t) - i\,h_\times(t)$, $\arg[h(t)]$ or $\tilde{h}(f)$). If Υ is derived from the time domain, then $s = t$; if Υ is in the frequency domain, then $s = f$. For either case, $[s_1, s_2]$, chosen within the domain of both the Post-Newtonian and Numerical Relativity data sets, defines the integration interval and, in most cases, the blending region. The vector $\vec{u}$ denotes the set of Post-Newtonian–parameters over which the fitting is performed. For example, $\vec{u} = (t_{\rm shift}, \phi_{\rm shift}, \mu)$ corresponds to adjusting time- and phase- shift and the mass ratio of the Post-Newtonian waveform to match the Numerical Relativity waveform. The best-fit parameters are denoted by $\vec{u}^*$ and a^*. The amplitude scaling factor, a, is often fixed to $a = 1$, but may be included in the fitting parameters [50]. Finally, in the limit $s_1 \to s_2$, this procedure reduces to enforcing equality of Υ_{PN} and Υ_{NR} at $s_1 = s_2$, as well as equality of the first derivative.

Explicitly, hybridization may be performed via the following algorithm:

1. Choose $[s_1, s_2]$ within the Post-Newtonian and Numerical Relativity data sets. Ideally, $[s_1, s_2]$ is sufficiently early so that both Post-Newtonian and NR sets should be accurate.

2. Evaluate Eq. Equation (57); apply $\{\vec{u}^*, a^*\}$ to the Post-Newtonian data set, resulting in $\Upsilon^*_{\rm PN}$. Measure error quantities relating to fit.

3. If desired, adjust $[s_1, s_2]$ and iterate (1) and (2), to find a preferred interval $[s_1^*, s_2^*]$.

4. Defining a monotonic function $z(s)$ such that $z(s < s_a) = 0$ and $z(s > s_b) = 1$, the hybrid is given by

$$\Upsilon_{\rm Hyb}(s) = [1 - z(s)]\, \Upsilon^*_{\rm PN} + a^*\, z(s)\, \Upsilon_{\rm NR}\ . \tag{58}$$

   Note that the transition region $[s_a, s_b]$ is generally taken to be a sub-interval of $[s_1^*, s_2^*]$, sometimes consisting of a single point.

For Georgia Tech's contribution to the NINJA-2 collaboration, the author implemented a hybridization routine following reference [46]. Put briefly, it is done in the time domain with $\Upsilon = h_+ - ih_\times$ and $\vec{u} = (t_{\rm shift}, \phi_{\rm shift})$. In the NRDA–Toolkit, `hyb_reg()` determines the blending region based on a given starting frequency and desired width. Then, the function `hyb4()` evaluates Equation (57) over $\{\vec{u}, a\}$. Lastly, Equation (58) is used to construct the final hybrid, with $z(t) = (t - t_1)/(t_2 - t_1)$. As a final comment, it is worthwhile to note that while the effectiveness of the above process has been investigated in detain (*e.g.* [66]), the gravitational wave community currently lacks an in depth understanding of how well it applies to general precessing cases.

3.3 Chapter Summary

In this chapter, we have seen a very brief overview of topics in NRDA that are not only pertinent to the remainder of this thesis, but also reflect the author's contributions to the Georgia Tech Numerical Relativity group's activities. In Section (3.1.1), the author's NRDA–Toolkit was introduced. In Section (3.2.1), an example was given for the calculation of gravitational wave strain from Numerical Relativity's ψ_4. In Section (3.2.2), we introduced the SNR and match, and a brief example was given for the SNR calculation. Finally, in Section (3.2.3), we motivated PN-NR hybridization by pointing out the limitations of short Numerical Relativity waveforms.

Independently, these topics lightly illustrate the practical connections between Numerical Relativity and gravitational wave experiment. But, *together*, they motivate, and form the

foundation of, gravitational wave modeling. In Section (3.2.2) we learned that gravitational wave signals embedded deep within noise may be filtered out *if* we have prior knowledge of what the signal looks like. While Numerical Relativity predominantly outputs the Weyl scalar, ψ_4, the conversion from ψ_4 to strain was demonstrated in Section (3.2.1), thereby illustrating that Numerical Relativity is a means by which gravitational wave signals can be calculated outside of perturbation theory.

However, we saw in Section (3.2.3) an example of how ideal, template waveforms that are the direct output of Numerical Relativity carry all of the shortcomings mentioned in Section (2.3.3). In particular, their duration, as well as our ability to generate them, are limited by computational expense. As a result, while Numerical Relativity is fully capable of generating the most theoretically accurate waveform models, its practical limitations bar it from being a direct resource to many problems in experiment data analysis. For example, in Section (3.2.2), we discussed the optimization of the match over many initial parameters. Even this very rudimentary process can require 10^2 to 10^6 waveforms, and thus cannot be accomplished purely within the realm of Numerical Relativity. Consequently, in order to overcome this and other practical barriers, the community of NRDA has recognized that *phenomenological* models of Numerical Relativity are needed.

Chapter IV

GRAVITATIONAL WAVE MODELING

In Section (2.2) we learned that Post-Newtonian approximations to Einstein's equations yield theoretically accurate models of binary black hole coalescence' gravitational waveforms. But we also learned that, as a perturbative formalism, they are inaccurate during the dynamical, strong-field regimes near binary black hole merger. In Section (2.3) we learned that Numerical Relativity overcomes the limitations of Post-Newtonian, but comes with a host of limitations of it own. In Section (3.2) we learned that Numerical Relativity, despite its limitations, is a fundamental tool for gravitational wave detection because it enables us to dig gravitational wave signals out of noise via matched filtering. However, in Section (3.3) we also recognized that the inherent *tensions* between Numerical Relativity's ability to yield theoretically accurate gravitational wave models, and its inability to do so arbitrarily quickly, results in a need for phenomenological models of Numerical Relativity's waveforms.

These tensions are at the heart of most current research within the NRDA community. They challenge us to develop gravitational waveform models that utilize both perturbation theory and Numerical Relativity (*e.g.* Section 3.2.3 and [55]). Concurrently, they challenge us to seek ever efficient solutions to highly dimensional data analysis problems (*e.g.* Section 3.2.2 and [67, 68]).

In this chapter, our awareness of these challenges brings us to the forefront of gravitational wave modeling. Specifically, we will overview in detail what is mean here by *modeling*, and then discuss two modeling approaches that underly results presented in following chapters. The first approach aims to represent the morphology of gravitational waves with closed form, analytic functions. The second approach takes the perspective of linear modeling, wherein gravitational waveforms are written as sums over waveform basis functions, times initial parameter dependent coefficients. In practice, there is a popular third

approach, which is based upon an Effective-One-Body treatment of binary black hole coalescence. However, this "EOB" approach is will be of auxiliary importance here for reasons that will be discussed in Chapter (7).

4.1 A Formal Perspective on Modeling

It is useful to begin by reviewing the structure of what is meant in this thesis by *modeling*. Specifically, in order to precisely frame the discussion in upcoming chapters, here we will very briefly construct a formal notion of modeling.

In the setting of NRDA, we find ourselves in a very common situation: we have a sparse set of information (Numerical Relativity waveforms), and we wish to use this sparse set to make practical statements about the more densely populated set to which it belongs (here, the continuous space of all gravitational waveforms). As we formalize our discussion of this problem, we will refer to the starting set of Numerical Relativity waveforms as the *training set*,

$$\mathcal{T} = \{h^{\rm NR}_k\}^N_{k=1}\,, \tag{59}$$

where $\mathcal{T}$ has N members. With the goal of connecting waveform morphology with initial binary parameters in mind, it is more useful to label each waveform with an initial parameter set $\boldsymbol{\lambda}_k = \{\vec{S}_1, \vec{S}_2, \vec{P}_1, \vec{P}_2, M, q\}_k \in \boldsymbol{\Lambda} = \{\boldsymbol{\lambda}_k\}^N_{k=1}$, rather than simply with k, as in Equation (59). We therefore have that

$$\mathcal{T} = \{h^{\rm NR}(\boldsymbol{\lambda}_k)\}^N_{k=1}\,. \tag{60}$$

As treated above, $h^{\rm NR}$ is not a waveform, but instead an operation that takes in one initial parameter set and then outputs a waveform. For example, in the frequency domain, $h^{\rm NR}(\boldsymbol{\lambda}) = \tilde{h}(f)$.

In much the same spirit, we will refer to the larger set to which $\mathcal{T}$ belongs as the *field*, $\mathcal{F}$, where $\mathcal{T} \subset \mathcal{F}$. The ability of numerical relativists to change initial binary parameters smoothly means that $\mathcal{T}$ can be identified with a smooth manifold. We may also attach to $\mathcal{F}$ the property that every waveform can be identified uniquely by only one set of initial

conditions, and vise versa. This vastly simplifies our perspective because it means that we will only need to keep track of one $\boldsymbol{\lambda}$ for each h^{NR}.

Now, with this underlying structure established, we may describe the gravitational wave modeling process in precise terms. Given some $\mathcal{T}$, and its corresponding initial parameter family $\boldsymbol{\Lambda}$, we wish to construct a smooth mapping (*i.e.* a *model*), $\hat{h}$, such that $\hat{h}(\boldsymbol{\lambda}_k)$ is approximately equal to $h^{\mathrm{NR}}(\boldsymbol{\lambda}_k)$ for all k, *and* in every small ε-region defined by $|\boldsymbol{\lambda}_k - \boldsymbol{\lambda}| < \varepsilon$. In essence, these conditions signify that the model must not only reproduce the training set, but it must also smoothly interpolate between points in parameter space.

Centrally, the condition that $\hat{h}(\boldsymbol{\lambda}_k)$ is approximately equal to $h^{\mathrm{NR}}(\boldsymbol{\lambda}_k)$ for all k can be satisfied by constructing $\hat{h}$ to depended on a set of model parameters that are *functions*[1] of $\boldsymbol{\lambda}$,

$$\boldsymbol{a}(\boldsymbol{\lambda}) = \{a_k(\boldsymbol{\lambda})\}_{k=1}^{M} \in \mathcal{R}^M \,.$$

In this sense, $\hat{h} \equiv \hat{h}_{\boldsymbol{a}}$, and the condition of similarity between $\hat{h}(\boldsymbol{\lambda}_k)$ and $h^{\mathrm{NR}}(\boldsymbol{\lambda}_k)$ is achieved by evaluating[2]

$$\delta_{\boldsymbol{a}}(\boldsymbol{\lambda}) = \max_k \; ||\hat{h}_{\boldsymbol{a}}(\boldsymbol{\lambda}) - h^{\mathrm{NR}}(\boldsymbol{\lambda}_k)|| \,. \tag{61}$$

and then finding model parameters such that $\delta_{\boldsymbol{a}}(\boldsymbol{\lambda})$ sufficiently approximates a global minimum

$$\boldsymbol{a}(\boldsymbol{\lambda}) = \underset{\boldsymbol{a}'}{\mathrm{argmin}} \; \delta_{\boldsymbol{a}'}(\boldsymbol{\lambda}) \,. \tag{62}$$

Equations (61-62) tells us plainly that the modeling problem is, at heart, an optimization problem in at least M dimensions. However, Equation (62) has one important limitation: *it does not guarantee that* $||\hat{h}_{\boldsymbol{a}}(\boldsymbol{\lambda}) - h^{NR}(\boldsymbol{\lambda})||$ *is small for all* $\boldsymbol{\lambda}$ *of interest.* We will return to this point in Chapter (7), where a machine leaning approach to modeling gravitational waveforms is presented. For now, we can use the framework above to efficiently review the two most pertinent modeling approaches in NRDA: representative modeling, and linear modeling.

[1] This includes constant functions.
[2] Here, $||x(s)||^2 = \int_{-\infty}^{\infty} x^*(s)x(s)\mathrm{d}s$.

4.2 Representative Modeling

Put simply, this approach to gravitational wave modeling aims to use closed form functions (*e.g.* polynomials, sine and cosine), to *represent* gravitational wave strain. This course may be pursued either in the time domain, by modeling $h(t)$, or in the frequency domain, by modeling $\tilde{h}(f)$. Frequency domain modeling is most often of interest, as its results may be readily applied to experiment oriented analysis routines without the need for Fourier transforms (Section 3.2.2).

Therefore, typically, representative modeling seeks $\hat{h}_{\boldsymbol{a}}$ such that $\hat{h}_{\boldsymbol{a}}(\boldsymbol{\lambda}) = \tilde{h}(f)$. Spurred by the fact that $\tilde{h}(f)$ are complex valued, separate amplitude and phase modeling are common:

$$\hat{h}_{\boldsymbol{a}}(\boldsymbol{\lambda}) = \hat{A}_{\boldsymbol{a}}(\boldsymbol{\lambda})\, e^{i\hat{\Phi}_{\boldsymbol{a}}(\boldsymbol{\lambda})}. \tag{63}$$

Concurrently, as there is no known single analytic function that is capable of representing all of inspiral, merger and ringdown, a piecewise approach is very often taken [62, 69, 50, 70].

For example, Santamaria *et al.* [62] seek to model the dominant, $l = m = 2$ multipole, and thereby construct $\hat{\Phi}_{\boldsymbol{a}}(\boldsymbol{\lambda})$ such that

$$\hat{\Phi}_{\boldsymbol{a}}(\boldsymbol{\lambda}) = \psi^{22}_{\mathrm{SPA}}(\boldsymbol{\lambda}) w^{-}_{f_1} + \psi^{22}_{\mathrm{PM}}(\boldsymbol{\lambda}) w^{+}_{f_1} w^{-}_{f_2} + \psi^{22}_{\mathrm{RD}}(\boldsymbol{\lambda}) w^{+}_{f_2} = \Phi_{\mathrm{phen}}(f)\ . \tag{64}$$

In Equation (64), ψ^{22}_{SPA}, ψ^{22}_{PM}, and ψ^{22}_{RD} are models for the inspiral, merger and ringdown portions of the waveform's phase. For example, $\psi^{22}_{\mathrm{PM}}(f) = \frac{1}{\eta}\left(a_1 f^{-5/3} + a_2 f^{-1} + a_3 f^{-1/3} + a_4 + a_5 f^{2/3} + a_6 f\right)$, and $\{a_1, a_2, ...a_6\} \subset \boldsymbol{a}$. Additionally, $w^{\pm}_{f_k}(f)$, are smooth blending functions of the form

$$w^{\pm}_{f_k} = \frac{1}{2}\left[1 \pm \tanh\left(\frac{4(f - f_k)}{d}\right)\right]\ . \tag{65}$$

Furthermore, in Equation (64), f_1 and f_2 are interrelated model parameters, $\{f_1, f_2\} \in \boldsymbol{a}$, with $f_1 = 0.1 f_2$.

Here, it is important to recall that inspiral (Section 2.2) and ringdown (Section 2.4) fall under the purview of their respective perturbation theories. For this reason, models of these regions must be consistent with their perturbation theory's predictions. As a final,

pertinent example, Santamaria *et al.* note the black hole perturbation theory describes gravitational ringdown for the $l = m = 2$ multipole to be given by

$$h_{22}(t) = A_{22}\, e^{it\tilde{\omega}_{22}}, \;\; \text{with} \;\; \tilde{\omega} = \omega_{22} + i/\tau_{22} \; . \tag{66}$$

Equation (66) is informed by perturbation theory's analytic prediction of $\tilde{\omega}_{22}$ [71], which upon considering the Fourier transform of $e^{it\tilde{\omega}_{22}}$, allows the identification of Equation (64)'s f_2 with $\omega_{22}/2\pi$.

In this way, representative gravitational wave modeling most often aims to independently model inspiral, merger and ringdown in a manner consistent with perturbation theory results for inspiral and ringdown. However, the interface between Numerical Relativity and perturbation theory is not always trivial. In particular, for ringdown, perturbation theory predicts that the spin weighted spheroidal harmonics, rather than Numerical Relativity's spin weighted spherical harmonics (Equation 43), are the most natural for representing gravitational wave strain. Specifically, Equation (66) is a spheroidal harmonic multipole moment, not a spherical harmonic multipole moment. Santamaria *et al.* make no distinction between spherical and spheroidal because, for $l = m = 2$, the two harmonics are nearly identical. However, in Chapter (5), we will see that for general l and m much more care is needed.

4.3 Linear Modeling

A fairly recent alternative to representative modeling stems from the application of "linear regression modeling" to gravitational waves [72, 73]. As its name suggests, under linear modeling one images that the gravitational wave strain is equal to a *linear* superposition of *basis waveforms*. Unlike representative modeling, where the modeling domain shape of the waveform is endowed by analytic functions, here each basis waveform represents an independent *feature* within the gravitational wave morphology. Of notable and practical importance is the fact that these features may be ordered in terms of their contribution to the total variance within a training set. In this sense the most important features may be identified, and kept for modeling while disregarding the rest, thus reducing the model's

complexity while making it more computationally efficient. For this reason, linear modeling approaches have flourished in many areas of computational science, including machine learning [72]. Here, we briefly describe the most basic and practical aspects of this topic. The discussion of linear modeling's connection to machine learning will be picked up in Chapter (7).

The linear modeling of gravitational wave strain starts by evoking the spectral theorem: *given set of orthonormal basis functions,* $\{\hat{e}_j\}_{j=0}^{N}$*, one may equate any function in the same space with a linear superposition over the basis.* For the space of gravitational waves spanned by a training set, one typically constructs the basis directly from the training set. For example, in the work of *Blackman et al.* [68], the $\hat{e}_j$ are derived from the training set by the Gram-Schmidt algorithm [74]. Alternatively, the recent work by Clark *et al.* [3] holds $\hat{e}_j$ to be the eigenvectors of $\mathcal{T}$'s covariance matrix[3] (*i.e.* here the $\hat{e}_j$ are the "principal components" of the training set [72]). In either case, given a training set of N linearly independent waveforms, one will generally have N basis waveforms. Upon construction, the basis set allows for the spectral decomposition of each waveform in the training set

$$h^{\mathrm{NR}}(\boldsymbol{\lambda}_k) = \sum_{j=1}^{N} a_j^{\mathrm{NR}}(\boldsymbol{\lambda}_k)\, \hat{e}_j \ , \tag{67}$$

where the coefficients, a_j^{NR}, are given by the standard inner-product

$$\begin{aligned} a_j(\boldsymbol{\lambda}_k) &= \langle \hat{e}_j | h^{\mathrm{NR}}(\boldsymbol{\lambda}_k) \rangle \\ &= \int_{-\infty}^{\infty} \hat{e}(t)^* h^{\mathrm{NR}}(t)\, \mathrm{d}t \\ &= \int_{-\infty}^{\infty} \tilde{\hat{e}}(f)^* \tilde{h}^{\mathrm{NR}}(f)\, \mathrm{d}f \, . \end{aligned} \tag{68}$$

In the second and third lines of Equation (68), we have utilized that $\hat{1} = \int_{-\infty}^{\infty} |f\rangle\langle f| \mathrm{d}f = \int_{-\infty}^{\infty} |t\rangle\langle t| \mathrm{d}t$. In essence, Equation (68) yields a set of discrete points, $a_j^{\mathrm{NR}}(\boldsymbol{\lambda}_k)$.

Centrally, it is upon this set of $a_j^{\mathrm{NR}}(\boldsymbol{\lambda}_k)$ that the model, $\hat{h}_{\boldsymbol{a}}$, is actually constructed. That is, we may identify the basis coefficients a_j^{NR} with the model's parameter functions, a_j (Section 4.1). In practice, the $a_j(\boldsymbol{\lambda})$ are often defined as polynomials fit to $a_j^{\mathrm{NR}}(\boldsymbol{\lambda}_k)$, or

[3] Here, the training set, $\mathcal{T}$, is referenced as a matrix of N columns, and its covariance matrix is given by $\mathcal{T}\mathcal{T}^{\top}/N$.

as spline interpolants between $a_j^{\rm NR}(\boldsymbol{\lambda}_k)$ [54]. In either case, the resulting *full-order* model takes the form

$$\hat{h}_{\boldsymbol{a}}(\boldsymbol{\lambda}) = \sum_{j=1}^{N} a_j(\boldsymbol{\lambda})\, \hat{e}_j \ . \tag{69}$$

Equation (69) refers to the full-order model because is neglects the fact that, for all $\boldsymbol{\lambda}_k$, not all $a_j(\boldsymbol{\lambda}_k)$ contribute significantly. For example, the previously mentioned principal component approach is such that the $a_j(\boldsymbol{\lambda}_k)$ are proportional to the amount of variance within $\mathcal{T}$ that is attributed to $\hat{e}_j$. With this in mind, one may quantify the percentage of variance held within each $\hat{e}_j$ by defining $E(j) = \sum_{j'=1}^{j} \mu_{j'} / (\sum_{j'=N}^{j} \mu_{j'})$, where μ_j are the square roots of $\mathcal{T}$'s covariance matrix eigenvalues[4]. In the case of Figure (9)'s Q-series, only

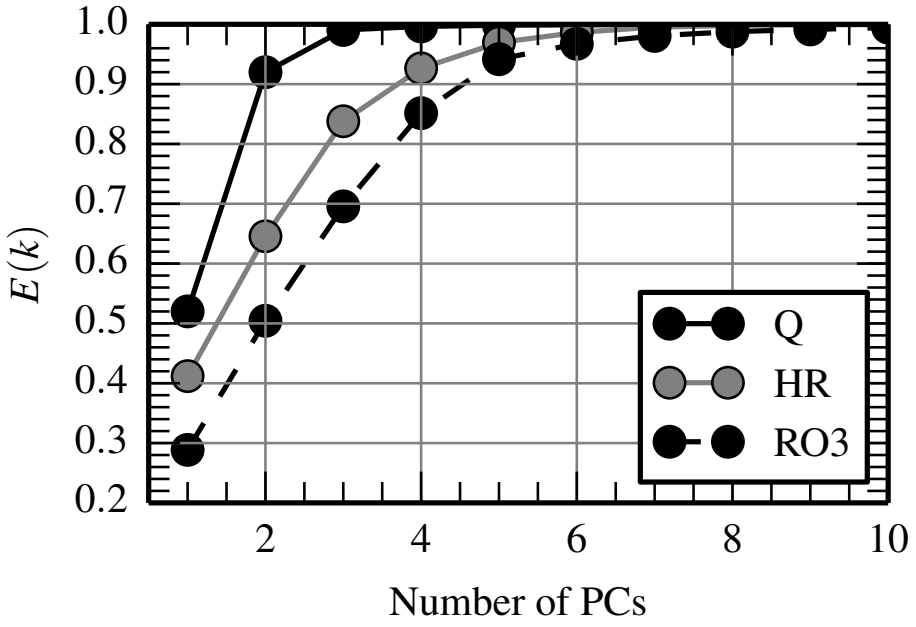

Figure 9: Here we see the number of principle components needed to represent some fraction, $E(k)$, of the variance within the training set [3]. Each curve represents a training set composed of different "initial parameter families". The Q-series is composed of 13 initially nonspinning variable massratio waveforms. The HR-series is composed of 15 initially nonspinning, variable mass ratio, spin-aligned waveforms, and the RO-series is composed of 20 precessing waveforms.

two $\hat{e}_j$, of the initial 13, are needed in order to account for more than 90% is the training set's variance. This implies that only $N' = 2$ of the terms in Equation (69) are actually

[4]This also happens to be a normalized measure of 1 minus the model's representation error

needed in order to accurately reproduce the training set. Put another way, it is possible to "reduce the order" of $\hat{h}_{\boldsymbol{a}}$ over $\boldsymbol{\Lambda}$, by only retaining the first N' terms in Equation (69), giving

$$\hat{h}_{\boldsymbol{a}}(\boldsymbol{\lambda}) = \sum_{j=1}^{N'} a_j(\boldsymbol{\lambda})\, \hat{e}_j \ . \tag{70}$$

For this reason, many classes of linear models are often referred to as *reduced-order* models (ROMs). In regards to the efficiency of data analysis routines, it is natural to imagine that the lower the model's order, the faster its implementations will be [54].

Lastly, while not sufficiently pertinent to expand upon here, it is worth noting that the success of linear modeling relies heavily on the construction of the basis set. For example, when using a training set from Numerical Relativity, one must be very careful to appropriately manage regions where non-physical information are prevalent in the waveform. However, with appropriate care, this difficulty can be overcome [68].

4.4 Chapter Summary

With the formal and specific definition of modeling established in Section (4.1), we now fully prepared to discuss the author's contributions to gravitational wave modeling. In particular, the representative modeling described in Section (4.2) underpins the author's listed contributions to modeling gravitational wave ringdown (Chapter 5). Similarly, the linear modeling of Section (4.3) is the foundation for the author's ongoing work at the intersection of machine learning and Numerical Relativity (Chapter 7).

ON GRAVITATIONAL WAVE MODELING: NUMERICAL RELATIVITY DATA ANALYSIS, THE EXCITATION OF KERR QUASINORMAL MODES, AND THE UNSUPERVISED MACHINE LEARNING OF WAVEFORM MORPHOLOGY

PART III

Topics in Gravitational Wave Modeling

by

Lionel London

Chapter V

MODELING GRAVITATIONAL RINGDOWN

5.1 Chapter Preface

As we approach the era of gravitational wave detection, there is a tremendous effort to understand and predict the rich gravitational wave signals coming from all expected sources of radiation. These predictions are used to construct gravitational wave templates that will enable not only the recognition of gravitational wave signals within noise, but also the extraction of information about the source. It is for these purposes that the development of templates that include the final moments of binary black hole coalescence is important for future gravitational wave detection.

While source populations remain uncertain, binary black hole systems are expected to account for multiple signals per year and, if systems with a total mass of a few hundred times that of our sun or larger are observed, detectors such as Advanced LIGO and the Einstein Telescope are most sensitive to the final stages of binary black hole coalescence [18, 19, 20, 21]. In these final moments the two black holes merge into a perturbed, remnant black hole, whose gravitational radiation *rings down* like a struck bell. Very roughly put, if one were to observe the remnant at an orientation (θ, ϕ) relative to its spin axis, and at a distance r away, then the observable time domain strain of this decaying *ringdown* radiation may be written as the real part of

$$\begin{aligned} h &= -\frac{1}{r} \sum_{l,m,n} A_{lmn}\, S_{lmn}(\theta,\phi)\, \frac{e^{i(\omega_{lmn}+i/\tau_{lmn})\, t}}{(\omega_{lmn}+i/\tau_{lmn})^2} \\ &= h_+ - i\, h_\times \ . \end{aligned} \tag{71}$$

Here, h_+ and $h_\times$ are the real valued plus and cross polarization states. In general, a linear combination of these states will be detected [75, 76].

If provided the remnant black hole's mass and spin, then the perturbation theory of isolated Kerr black holes informs us of Equation (71)'s spatial multipoles and temporal

frequencies: the QNMs that dominate ringdown [77, 40, 78]. However, in order to model astrophysically relevant ringdown signals the output of Numerical Relativity simulation is generally needed to tell us how much each multipolar component is excited for a given initial binary [78, 79].

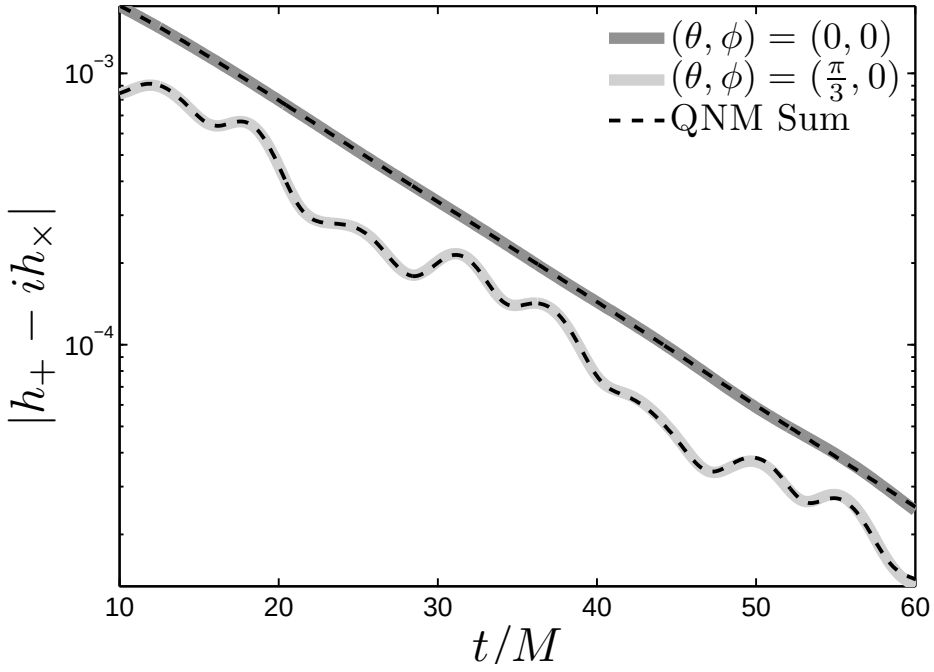

Figure 10: Ringdown for a 2:1 mass-ratio, initially nonspinning black hole binary calculated via the GaTech `MAYA` code [2, 4, 5, 6, 7]. The solid gray lines show the time domain envelope of Numerical Relativity ringdown for two different lines of sight. Here θ and ϕ are polar and azimuthal angles relative to the black holes final spin vector. The dashed black lines show the corresponding model ringdowns (QNM sums) calculated using the results of this chapter: estimation of spheroidal QNM excitations from Numerical Relativity, including and beyond the fundamental overtones.

For this reason, applying perturbation theory to the analysis of Numerical Relativity ringdown has assisted in the creation of inspiral-merger-ringdown templates [80, 81, 82], and revealed novel relationships between the initial binary's configuration and the remnant black hole's parameters [79]. But thus far, technical challenges have limited analysis primarily

to the fundamental (lowest overtone) QNMs, while it has also been acknowledged that a more detailed application of perturbation theory to Numerical Relativity ringdown may be needed [79, 80, 83, 84, 85, 86, 87]. As an example of ringdown's potential complexity, Figure (10) shows the time domain strain envelope of a potential 2:1 mass-ratio ringdown signal of an initially nonspinning black hole binary, observed at two different lines of sight. Here we see that the sum of many QNMs precisely models Numerical Relativity ringdown data. This example case demonstrates that both the intrinsic QNMs of perturbation theory and the observer's extrinsic line of sight contribute to the richness of possible ringdown signals.

In this study we assist in clarifying the extent to which QNMs beyond the fundamentals are pertinent to the physics and modeling of Numerical Relativity ringdown (e.g. Figure 10). We consider the ringdown of 68 initially nonspinning binary black hole simulations of mass-ratios between 1:1 and 1:15. In doing so, we find that QNM excitation is exceptionally well modeled by a Post-Newtonian expansion (Sec.5.4). However, we also find that the excitation amplitudes of some QNMs differ qualitatively from their Post-Newtonian counterparts, suggesting that the imprints of nonlinear merger are more evident in these QNMs than in others (Sec.5.6.1). But first, we present a robust method to estimate multiple QNMs within Numerical Relativity ringdown (Sec.5.3.1). We then apply this method to a series of initially nonspinning Numerical Relativity runs of varying mass-ratio (Sec.5.3.2-5.4.2). Lastly, we consider the results of our analysis (overtones and second order modes) in the context of ringdown-only templates (Sec.5.6.2). Generally, our results may be of use for the construction of merger-ringdown templates.

A complete chapter outline is given in Sec. 5.1.3. A full summary of fitting formulas and coefficients for QNM excitations is given in Appendix A. For convenience, fits for the

most dominant QNM excitation amplitudes in Equation (71) are below:

$$A_{220} = \eta\tilde{\omega}_{220}^2 \, (0.18e^{0.06i} + 0.10e^{-2.21i}\eta + 5.09e^{0.24i}\eta^2) \tag{72}$$

$$A_{221} = \eta^2\tilde{\omega}_{210}^2 \, (0.89e^{-2.94i} + 6.30e^{0.13i}\eta + 19.40e^{2.96i}\eta^2) \tag{73}$$

$$A_{210} = \eta\tilde{\omega}_{210}^2 \, \frac{\mathrm{m}_1 - \mathrm{m}_2}{M} \, (0.20e^{2.42i} + 0.36e^{-2.65i}\eta + 1.03e^{-2.04i}\eta^2) \tag{74}$$

$$A_{330} = \eta\tilde{\omega}_{330}^2 \, \frac{\mathrm{m}_1 - \mathrm{m}_2}{M} \, (0.08e^{-0.12i} + 0.91e^{1.53i}\eta + 5.35e^{-1.13i}\eta^2 + 20.66e^{1.75i}\eta^3) \tag{75}$$

$$A_{320} = \eta\tilde{\omega}_{320}^2 \, (0.07e^{-0.77i} + 0.46e^{1.71i}\eta + 0.78e^{-2.04i}\eta^2 + 2.48e^{-2.55i}\eta^3) \tag{76}$$

$$A_{440} = \eta\tilde{\omega}_{440}^2 \, (0.06e^{0.01i} + 0.78e^{2.59i}\eta + 7.74e^{-0.44i}\eta^2 + 41.32e^{2.73i}\eta^3 + 82.02e^{-0.58i}\eta^4) \, . \tag{77}$$

Here, M is the sum of the initial black hole masses,

$$M = \mathrm{m}_1 + \mathrm{m}_2 \, ,$$

and η is the symmetric mass-ratio,

$$\eta = \frac{\mathrm{m}_1\mathrm{m}_2}{M^2} \, .$$

The amplitudes are scaled relative to 10 M after the peak luminosity in ψ_{22}^{NR} (Sec. 5.1.2),

Note that the QNM frequencies, $\tilde{\omega}_{lmn}$, are complex, and depend on the remnant black hole's parameters: spin magnitude and mass.

$$\tilde{\omega}_{lmn} \equiv \omega_{lmn} + i/\tau_{lmn} \tag{78}$$

In Equation (78), ω_{lmn} is the QNM's central oscillation frequency, and τ_{lmn} the mode's decay time. Each frequency may be conveniently computed using the mapping between η

and remnant black hole parameters given in Eqs. 122 and 121, or Ref. [88], along with the phenomenological fitting formulas[1] for QNM frequencies in Ref. [89].

5.1.1 From QNMs and templates to Numerical Relativity ringdown analysis

Shortly after Vishveshwara's 1970 discovery that perturbed black holes dissipate energy via gravitational ringdown, the study of perturbed black holes began a proliferation that now enables the creation of gravitational wave ringdown templates [41, 90, 91]. In 1971 Teukolsky and Press revealed that ringdown should be well approximated by a sum of eigenfunctions of Teukolsky's master equation which describes first order departures from the Kerr metric [48, 77, 92]. For a black hole of mass M_f and dimensionless spin parameter,

$$j_f = \frac{s_f}{M_f^2} \ ,$$

these eigenfunctions are uniquely determined. Here s_f is the magnitude of the final black hole spin vector. Press later referred to Teukolsky's set of radial, angular, and temporal eigenfunctions as QNMs [92, 90] (Equation 81). QNMs are multipoles with the usual polar and azimuthal indices, ℓ and m. In addition, in loose analogy with acoustic theory, they are also labeled by an *overtone* number, $n = \{0, 1, 2...\}$, where, as n increases, so does the typical QNM decay rate [40]. The $n = 0$ QNMs are traditionally referred to as the *fundamental* modes.

Given that astrophysical black holes are expected to be described by only mass and spin, the work of developing gravitational wave templates that include ringdown is largely equivalent to modeling the excitations of Kerr QNMs for different progenitor binaries [91, 93]. This work has largely focused on the most slowly decaying, fundamental QNMs, which correspond to first order departures from the Kerr metric.

However, it has been suggested that second order QNMs, resulting from *nonlinear* self-coupling of their first order counterparts, may also be pertinent [38, 85, 94, 95, 96, 97]. Although these second order QNMs have largely been studied for Schwarzschild black holes,

[1] Note that here $\tilde{\omega}_{lmn}$ are in units of $1/M$ while [89] reports the unitless $M\,\tilde{\omega}_{lmn}$.

where Regge-Wheeler-Zerilli techniques can be directly applied, formal results for the Kerr case do not appear to exceed [38], wherein the second order contribution's wave equation is derived within the Newman-Penrose formalism.

This result demonstrates that the second order wave equation for Kerr, like its Schwarzschild counterpart, is sourced by a quadratic function of the first order modes. For this reason it is expected that the second order QNMs for Kerr are characteristically similar to those for Schwarzschild [95]. In particular, one might expect to find within Figure (10) damped sinusoids whose frequencies and decay rates are sums of those from two first order modes[2].

From these considerations it is clear that perturbation theory allows for an extremely rich space of possible ringdown signals. But given that the fundamental modes are the slowest damped, it is not immediately clear that modes beyond the fundamentals are pertinent to modeling of Numerical Relativity ringdown. Indeed, the single and two-mode ringdown-only templates of Ref. [91] only consider fundamental QNMs. Similarly, studies that focus on linking QNM excitation with initial binary parameters typically focus only on the fundamental modes [9, 79, 98] and, while work on templates that include both merger and ringdown has found that overtones are required to blend the two regions, a systematic study of overtone excitement is lacking [82, 86, 80, 87]. Moreover, there has been no work published on the detection of nonlinear second order QNMs within Numerical Relativity binary black hole coalescence. Here, we inform these areas by describing QNM excitation for a series of initially nonspinning, unequal mass binary black hole systems.

For the recovery of these initial parameters precise agreement between template and signal is needed. Concurrently, only qualitative agreement is needed for detection purposes [91, 93]. Although a full exploration of detection and parameter estimation is beyond the scope of the current study, we note that the richness of possible signals depends not only on the configuration of the initial binary, but also the orientation of the black hole's final spin vector with respect to the observer's line of sight.

As an example, consider again Figure (10). Here we see that if this idealized signal is

[2]This is analogous to the anharmonic oscillator, in which the second order oscillation frequency is twice the first order one [95].

observed along the remnant black hole's final spin axis, $\theta = 0$, then the envelope of its time domain behavior appears to be dominated by a single exponentially decaying function, or equivalently, a single QNM; however, if observed at a significant angle with respect to the final spin axis, here $\theta = \pi/3$, then many QNMs may visibly contribute. In order to model the complexities of these potential signals, we utilize the intersections between perturbation theory and Numerical Relativity.

5.1.2 Numerical relativity meets perturbation theory

Numerical Relativity waveforms are typically decomposed[3] into spin weighted-2 spherical harmonics, ${}_{-2}Y_{lm}(\theta, \phi)$, such that the Weyl scalar ψ_4 is given by

$$\psi_4(t, \theta, \phi, r) = \frac{1}{r} \sum_{l,m} \psi^{\rm NR}_{lm}(t) \left[{}_{-2}Y_{lm}(\theta, \phi) \right] . \tag{79}$$

For gravitational radiation, the orthogonality of these harmonics in both ℓ and m ensures that this is a true spectral decomposition:

$$\psi^{\rm NR}_{lm}(t) \equiv r \int_\Omega \psi_4(t, \theta, \phi, r) \, {}_{-2}\bar{Y}_{lm}(\theta, \phi) \, {\rm d}\Omega \, . \tag{80}$$

Here ${}_{-2}\bar{Y}_{lm}(\theta, \phi)$ is the complex conjugate of ${}_{-2}Y_{lm}(\theta, \phi)$, and we will focus on $\psi^{\rm NR}_{lm}$, the spherical harmonic multipoles of the Weyl scalar ψ_4. The Weyl scalar ψ_4 is related to the observable strain via two time derivatives, $\psi_4 = -\ddot{h}$ [75].

During ringdown, this choice of multipolar decomposition effectively casts the radiation as that corresponding to a perturbed *nonspinning* black hole [75]. However the remnant of a binary black hole merger is typically a spinning black hole.

For these cases, the perturbation theory of Kerr black holes [99] yields

$$\psi_4(t, \theta, \phi) \approx \frac{1}{r} \sum_{l,m,n} \psi^{\rm PT}_{lmn}(t) \left[{}_{-2}S_{lm}(j_f \tilde{\omega}_{lmn}, \theta, \phi) \right] \tag{81}$$

$$\psi^{\rm PT}_{lmn}(t) \equiv A_{lmn} \, e^{i \tilde{\omega}_{lmn} t} \, , \tag{82}$$

[3] This decomposition is typically done such that the origin is at the initial binary's center of mass. In general, this is not the location of the remnant black hole if there is a nonzero recoil velocity. However, for the systems studied here, the typical distance traveled postmerger, is sufficiently small compared to the waveform extraction radius, making this initial center of mass location a good approximation for the position of the remnant black hole. Nevertheless, as discussed in Sec. 5.5 , this does potentially introduce detailed effects that may not be inherent to the ringdown regime.

where $\tilde{\omega}_{lmn}$ is the complex QNM frequency, ${}_{-2}S_{lm}$ are the spin weighted *spheroidal* harmonics, and A_{lmn} are the complex QNM amplitudes or *excitation coefficients* whose magnitude is contingent on where t is chosen to be zero [90, 100, 101].

For example, if t_* is the time relative to the peak luminosity of $\psi_{22}^{\rm NR}$, and one considers ringdown to include $T_0 \geq 10\ (M)$ after $t_* = 0$, then $t \equiv t_* - 10\ (M)$ [98]. Here we consider t to be in units of the initial binary mass, M, which is canonically set to unity.

Generally, Equation (81) is not an equality as power-law tails, of the form $\psi_{\rm tail} \sim t^{-k}$, are also expected in the postmerger regime [102, 99]. While, in principle, these power-law contributions may be significant near the radiation's peak, a host of numerical studies has shown them to be extremely weak throughout the subsequent QNM regime[4] [99, 78]. In particular, while all power-law functions decay slower than exponentials, they also require excitation coefficients much larger than those of QNMs to contribute significantly to the waveform. Therefore there is a heuristic expectation that the power-law tails eventually dominate the postmerger waveform, but only at very late times [105, 106, 99, 107]. Indeed, recent Numerical Relativity codes that focus on binary black hole coalescence have empirically verified this expectation [86, 78, 87, 98]. Numerical studies that focus specifically on solving Teukolsky's equation do find that power-law tails are physically meaningful, but only at late times, and at amplitudes that are very likely inaccessible to codes that solve Einstein's equations in full [103, 107].

While the current study, in part, seeks to describe ringdown in unprecedented detail, we also find that for the systems considered, power-law decay can be neglected.[5]

For simplicity we have written Equation (81) as a sum over the first order QNM indices only. If written explicitly, the second order QNM terms, being proportional to products of two first order QNMs, would be labeled by six indices, $(l_1, m_1, n_1)(l_2, m_2, n_2)$ [85, 94, 95]. We have also neglected to explicitly write the *conjugate* or *mirror-mode* terms which arise from Teukolsky's azimuthal equation having two linearly independent solutions that, due

[4] In contrast to the current study, which evolves the full Einstein equations, studies that are able to resolve late-time power-law decay evolve Teukolsy's equation (e.g. [103]), which is motivated by first-order departures from the Kerr space-time [104].

[5] This is readily visible in Figure (12)'s lower panel where, if power-law tails did contribute significantly, they would cause a localized feature near zero frequency.

to nonzero black hole spin, are not the complex conjugates of each other [40, 89].

An additional consequence of nonzero black hole spin is that the spheroidal harmonics, while orthogonal in m, are *not* orthogonal in l for the complex QNM frequencies of ringdown[6], making a spectral decomposition of the form of Equation (80) not possible. However, just as the Kerr metric reduces to the Schwarzschild metric for nonspinning black holes, so do the spheroidal harmonics reduce to the sphericals. Substituting Equation (81) into Equation (80) illustrates this point by revealing that the spherical multipoles of Numerical Relativity are each a sum of many spheroidal QNMs where, in the $j \to 0$ limit, only the $l = l'$ term survives

$$\psi^{\rm NR}_{l'm}(t) \approx \sum_{n,l} A_{lmn}\, \sigma_{l'lmn}\, e^{i\tilde{\omega}_{lmn} t} \tag{83}$$

$$\sigma_{l'lmn} \equiv \int_\Omega {}_{-2}S_{lm}(j_f \tilde{\omega}_{lmn}, \theta, \phi)\, {}_{-2}\bar{Y}_{l'm}(\theta, \phi)\, {\rm d}\Omega\,. \tag{84}$$

This was first noted in 1973 by Press and Teukolsky [77] who used standard operator perturbation theory to show that

$$\begin{aligned} {}_{-2}S_{lm} &= {}_{-2}Y_{lm} + j_f\, \tilde{\omega}_{lmn} \sum_{l \neq l'} {}_{-2}Y_{l'm}\, c_{l'lm} \\ &\quad + O(j_f\, \tilde{\omega}_{lmn})^2\,. \end{aligned} \tag{85}$$

Here $c_{l'lm}$ are related to the Clebsch-Gordon coefficients [89, 48].

Equations 83 through 85 motivate two approaches to characterize QNM excitations, A_{lmn}: single-mode and multimode fitting.

Single-mode fitting.— The first category makes the practical assumption that Equation (83) is dominated by the $l = l'$ term, and thereby estimates the QNM amplitudes by fitting a single mode to $\psi^{\rm NR}_{lm}$. Although this *single-mode* approach has been shown to be effective for the first few $l = m$ multipoles [9, 78], in principle, it neglects the presence of overtones and black hole spin [90, 83]. Moreover, because Equation (85) says that the mixing between spherical and spheroidal harmonics becomes more prevalent for higher spins, we

[6] Specifically, we are concerned with spheroidal harmonics with complex frequency and of spin weight $s = -2$, which correspond to exponentially damped time-domain waveforms.[100, 108]

may hypothesize that single-mode fitting incurs residuals that are qualitatively proportional to the remnant black hole's spin. In particular, Figure (11) shows that initially nonspinning, quasicircular binary black hole systems coalesce to form a remnant black holes whose final spin is proportional to the initial binary's symmetric mass-ratio. We would therefore expect single-mode fitting of these systems to perform better for low mass-ratios ($m_1 \ll m_2$), and worse at higher mass-ratios ($m_1 \approx m_2$).

Specifically, while it has been shown that Equation (84)'s $\sigma_{l'lmn}$ can be on the order of 0.10 for moderate values of j_f [100], Equation (83) communicates that the relative values of different A_{lmn} ultimately determine the significance of each QNM term [83].

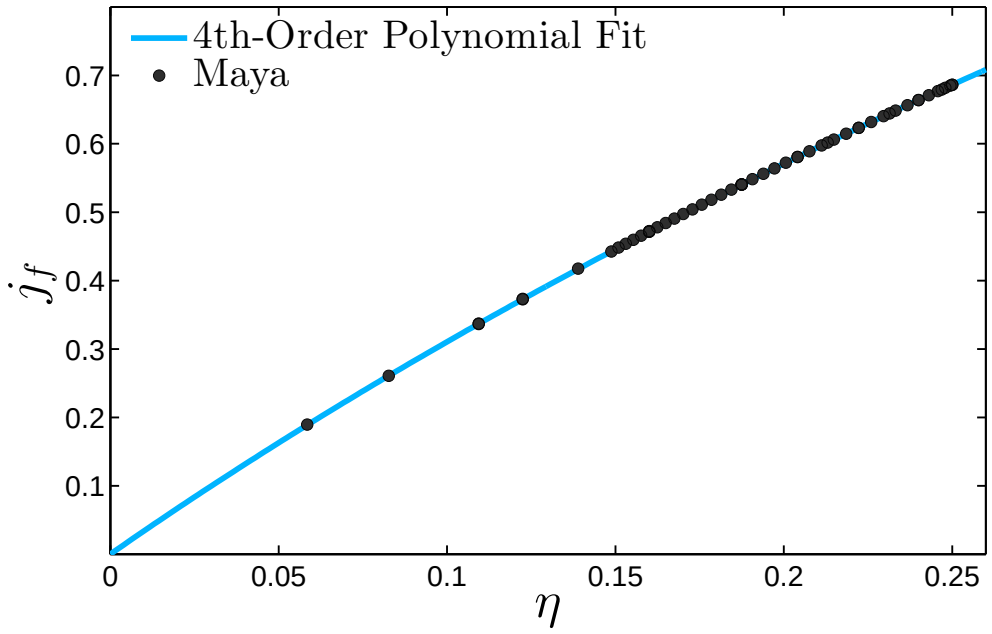

Figure 11: Remnant black hole spin for initially nonspinning systems of varying mass-ratio. The black dots are final spin values calculated using the isolated horizon formalism [8]. The trend is monotonic and well fitted with a fourth order polynomial (Appendix C).

Multimode fitting.— The second category attempts to fit *each* term in Eqn. (83), and therefore requires the simultaneous fitting of multiple QNMs within each spherical multipole. Although this *multimode* approach is more faithful to the fact that the black holes of interest

are spinning, current fitting methods have had limited success [87, 109, 110]. The difficulty is primarily due to complexity: within each $\psi^{\rm NR}_{lm}$, a multimode fitting algorithm must optimize over $\{Re[A_{lmn}]$, $Im[A_{lmn}]$, ω_{lmn}, $\tau_{lmn}\}$ as well as the total number of significant QNMs, N. There are secondary difficulties arising from data accuracy and numerical artifacts. As a result, the multimode approach is a $4\times N$ dimensional optimization problem of combinatoric complexity whose solution must be robust against numerical errors. It is a lot like trying to identify a musical chord by ear.

5.1.3 Structure of the Chapter

In the current study we present a multimode fitting method, and apply it to the Numerical Relativity ringdown of 68 initially nonspinning, unequal mass-ratio binaries with symmetric mass-ratios between $\eta = 0.2500$ and $\eta = 0.0586$.

We report estimates for the QNM excitations of not only fundamental modes, but also for overtones and what appear to be second order modes. We go on to discuss our results in the context of phenomenological ringdown models and future detection scenarios. First, in Sec. 5.2.1 we review the single-mode approach, and report fit residuals. As described in Sec. 5.2.2, for nominal fitting regions, we find that single-mode fitting incurs roughly 1% fitting errors for the best case scenario, and greater 10% error in the worst case scenarios. We also review the systemic dependence of residuals with final black hole spin. In Sec. 5.3.1 we introduce our multimode fitting method, and compare it with other approaches using mock data in noise, then review found QNM amplitudes and residual errors. In Sec. 5.4, we present post-Newtonian inspired fits to the dominant QNM excitations across the range of mass-ratios. In Sec. 5.5 we discuss the limitations of our results, and their consistency with perturbation theory. Finally, in Sec. 5.6, we discuss our results in the contexts of analytic (nonlinear) perturbation theory, and review the significance of our findings to a mock detection scenario.

5.2 Motivations for multimode Fitting

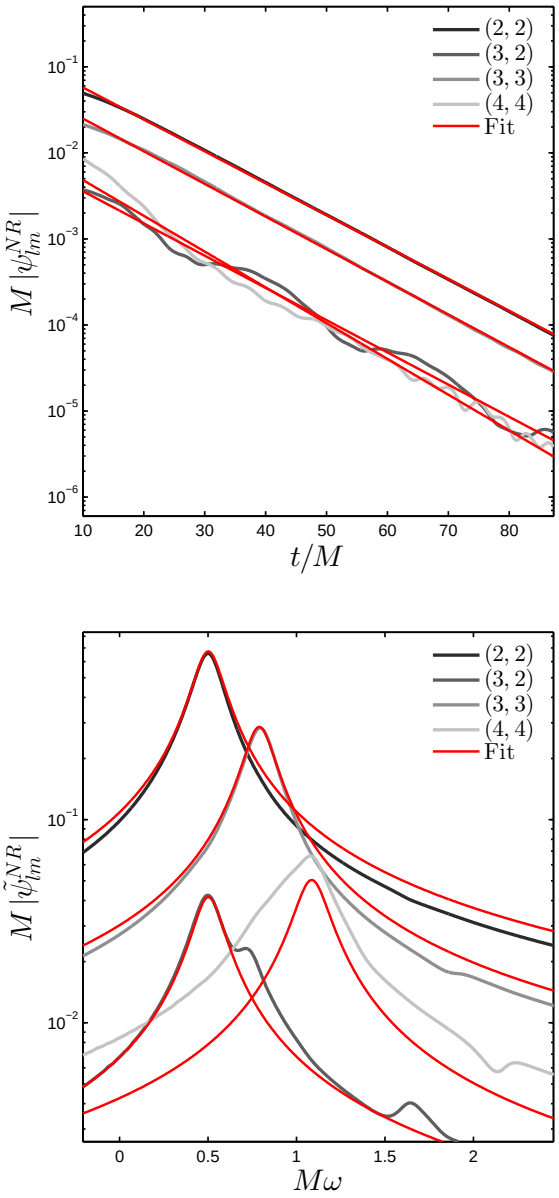

Figure 12: As demonstrated by this set of 2:1 mass-ratio nonspinning waveforms, fitting a single decaying sinusoid to ψ^{NR}_{lm} incurs systematic residuals. **Top Panel:** The time-domain envelopes for $(2,2), (3,3), (3,2), (4,4)$ spherical multipoles and related fits, starting $10M$ after the peak luminosity of ψ^{NR}_{22}. **Bottom Panel:** The frequency-domain envelopes, $|\tilde{\psi}^{\rm NR}_{l,m}|$. All fits correspond to the lowest, $n = 0$, QNMs. While the $(2,2)$ and $(3,3)$ multipole waveforms are best described by a single QNM fit, all fits display visible deviations from the raw data.

Let us first consider the single-mode fitting approach discussed in Sec. 5.1.2. Figure 12 shows single-mode fits for a 2:1 mass-ratio binary. While we can see that in this case the subdominant $\psi^{\rm NR}_{lm}(t)$ are not all simple functions, the dominant multipoles do appear to have exponentially decaying envelopes, and so are well modeled by a single QNM. Indeed, previous studies have found success in treating the dominant multipoles as single QNMs during ringdown [9, 78]. In particular, this approach has led to effective numerical estimates of black hole final spin and mass, as well as the characterizations of fundamental QNM amplitudes with mass-ratio, and initial spin magnitude [111, 98]. It is therefore fair to suppose that more detailed QNM information is not needed in order to capture ringdown's dominant physics. In what follows, we test this heurism by first outlining the single-mode approach, and then investigating the dependence of fit residuals with initial binary parameters (Figure (13)).

5.2.1 Single-mode fits

First, we outline a qualitatively general single-mode fitting procedure to estimate the fundamental ($n = 0$) QNM excitations:

a. Given the set of $\psi^{\rm NR}_{lm}$, we define ringdown to be the region $\{T_0 \leq t \leq T_1\}$ relative to the peak luminosity[7] of $\psi^{\rm NR}_{22}$ [9].

b. To calculate the waveform's phase, $\theta_{lm}(t)$, and envelope, $\Psi_{lm}(t)$, we then consider the standard representation for the fit:

$$\psi^{Fit}_{lm}|_{\{T_0\leq t\leq T_1\}} \;=\; \Psi_{lm}\, e^{i\,\theta_{lm}} \;.$$

c. We then use linear least-squares fitting to model $\theta_{lm}(t)$ and $Log[\,\Psi_{lm}(t)\,]$ as lines in the time domain:

$$\theta_{lm} \;=\; t\,\omega^{Fit}_{lm} + \delta^{Fit}_{lm} \tag{86}$$

$$Log[\,\Psi_{lm}(t)\,] \;=\; -t/\tau^{Fit}_{lm} \;+\; \mathrm{Log}|A^{Fit}_{lm}| \tag{87}$$

[7] As will be discussed in Sec. 5.3.1, we consider multiple fitting regions in order to characterize both the data and fit. In the case of single-mode fitting, fitting regions were chosen to encompass between 86 and 74 (M). For the multimode fitting approach to be discussed in Sec. 5.3.1, each waveform was windowed and padded after the onset of numerical noise to maintain a consistent frequency domain resolution.

where δ_{lm}^{Fit} is the complex phase of A_{lm}^{Fit}.

d. Upon calculating the fit parameters, $\{A_{lm}^{Fit}, \omega_{lm}^{Fit}, \tau_{lm}^{Fit}\}$, we calculate the *fractional root-mean-square error*,

$$\varepsilon_{lm} \equiv \left| \frac{\langle\, (\,\psi_{lm}^{\rm NR} - \psi_{lm}^{Fit}\,)^2\,\rangle}{\langle\, \psi_{lm}^{\rm NR\,2}\,\rangle} \right|^{1/2} . \tag{88}$$

Here ε_{lm} is typically much less than 1 for good fits, and of order 1 or greater for poor fits. More carefully, as discussed in Sec.5.2.3, ε_{lm} is susceptible to being biased by numerical noise. In the worst case scenario, where noise dominates the data to be fit, $\varepsilon_{lm} \approx 1$ may correspond to a minimum residual with respect to fit parameters.

Typical single-mode fits are shown in Figure (12) for a $2:1$ mass-ratio binary, with the fitting region starting $T_0 = 10\,M$ after the peak luminosity in $\psi_{22}^{\rm NR}$. Here, as well as throughout this chapter, the Fourier transform of waveforms, $\psi(t)$, will be denoted as $\tilde{\psi}(\omega)$. Note that the $l = m$ multipoles are well fit, with associated errors $\varepsilon_{lm} \approx 0.08$. However, a notable exception is the $l = m = 4$ multipole with ε_{44} and order of magnitude higher at ≈ 0.65.

Moreover, as has been found in previous studies, we also find that the $l \neq m$ multipoles are generally not well fit by a single QNM. For example, the $(l, m) = (3, 2)$ multipole, $\psi_{32}^{\rm NR}$, is known to have a significant contribution from the $(l, m, n) = (2, 2, 0)$ term in Equation (83) [83, 87, 78, 112]. This may be recognized in the lower panel of Figure (12), where $\psi_{32}^{\rm NR}$ is seen have its dominant peak not at $\psi_{32}^{\rm PT}$'s central frequency[8] of $M\omega = 0.73$, but at $M\omega = 0.50$, directly under the peak of $|\tilde{\psi}_{22}^{\rm NR}|$.

In what follows we discuss the residual error of the single-mode approach. In particular, we ask if the errors are dominated by numerical artifacts (e.g. resolution related errors [111]), or if the errors are dominated by the effects of nonzero black hole spin.

5.2.2 Single-mode fits: Results and residuals

To investigate the residuals incurred by single-mode fitting, we consider 36 initially nonspinning, unequal mass binaries with η between 0.2500 and 0.0586. The left panel

[8]The central frequency is given by the real part of the QNM frequency.

of Figure (13) shows typical fit excitation amplitudes, $|A_{lm}^{Fit}|$, and the right panel shows the corresponding residual errors (Equation (88)). The left panel of Figure (13) shows that QNM excitation appears regular with symmetric mass-ratio with the $n = 0$ mode dominating. The fitting model proposed in Ref. [9] is also plotted. The lower left panel of Figure (13) indicates that the $(\ell, m, n) = (4, 4, 0)$ has a significant local minimum at $\eta \approx 0.22$ ($m_1/m_2 \approx 2$) for the resolution in η considered here. The $(\ell, m, n) = (3, 2, 0)$ QNM has been found to exhibit a similar local minimum [83].

Turning to the right panel of Figure (13), the $(\ell, m, n) = (2, 2, 0)$ and $(3, 3, 0)$ cases show monotonically decreasing trends. This trend may be due to the difference between spherical and spheroidal harmonics, which is proportional to final black hole spin (Equation 85), and is therefore also proportional to symmetric mass-ratio (Figure 11); thus, single-mode fitting may incur systematic errors that decrease with η.

While the ε_{21} and ε_{44} estimates display a more complicated behavior, their overall decrease with η suggests that these cases may be significantly affected not only by QNMs beyond the fundamentals, but also by other sources of errors.

5.2.3 Sources of error

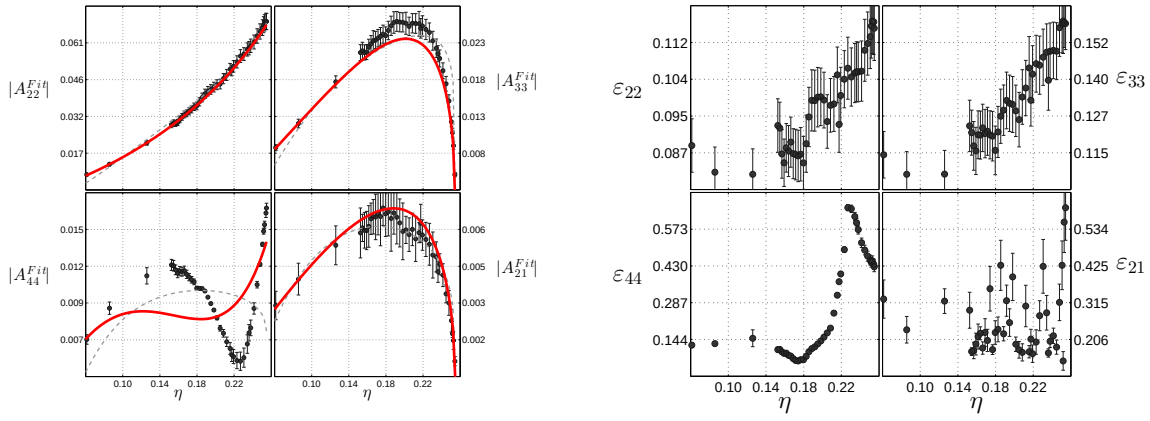

Figure 13: Here we see the fundamental QNM excitations estimated by single-mode fitting. Left: The black dots are the excitation amplitudes estimated from fitting. For reference, the dashed grey lines are phenomenological fits from Kamaretsos *et. al.* [9], and the solid red lines are phenomenological fits from the more recent study by Meidam *et. al.*[10]. The error bars were calculated as described in Sec. 5.3.1- f. The right set of panels shows the related fractional residual errors calculated via Equation (88).

To contrast how much of each ε_{lm} is attributed to nonfundamental QNMs rather than other factors, we briefly review the primary numerical sources of error: finite resolution and extraction radius. In aggregate, we find that the overall effect of these errors contributes to a noise floor that, at $\sim 10^{-6}$ $(1/rM)$, is typically 2 orders of magnitude lower than the relative fit errors shown in the right panel of Figure (13). As a general consequence, ε_{lm} is increasingly biased by numerical noise as $|\psi_{lm}^{\mathrm{NR}}|$ approaches the noise floor. This is most evident for ε_{44}, which displays a pronounced increase as $|A_{44}^{Fit}|$ sweeps through its local minimum.

For the waveforms used here, the simulation grid is structured so that there is a central grid of maximal resolution within peripheral grids whose resolution decreases by a factor of 2 at each outward extension. The result is an inherent tension between the finite extraction

radius, and the finest grid resolution (see Sec. 5.5.3 for an expanded discussion of finite extraction radius and related gauge effects.). In effect, this means that $\psi^{\rm NR}_{lm}$ up to $\ell = m = 5$ are resolved spatially, with ~ 7 points oscillation cycle, and temporally with ~ 42 points per cycle[9]. In particular, we find that duplication of Figure (13) at $\eta = \{0.25, 0.19, 0.16\}$ is consistent with resolutions {0.62,1.125,1.25} times that of the values quoted above, and, therefore, the right panel of Figure (13) is not dominated by resolution effects.

Our post-merger data contain low amplitude, high frequency oscillations that contribute at most 5% to our estimates of residual error, ε_{lm}, and appear to be an effect of discretization. This high frequency contribution is visible in Figure (12) as low amplitude features to the right of each central frequency. While the high frequency of these oscillations means that their contribution to the mean residual difference is small, the magnitude of these oscillations is also marginal across multipoles, and appears at comparable power at the same positive and negative frequency. As seen in Figure (12), this frequency varies from multipole to multipole. Despite their pervasiveness, these features are too high to be pertinent QNM frequencies [Eq. 84], and are likely artifacts due to our simulation's containing nonzero power at frequencies beyond the resolvable limit. Comparison with public `NINJA` waveforms [45] reveals that these features show up inconsistently across NR implementations, which suggests that they are both spurious effects due to discretization, and independent of the dominant physics at play[10].

As a result, we conclude that the fit errors in Figure (13) are not dominated by numerical artifacts, but instead primarily due to choice of representation: the spherical representation of Equation (79), versus the spheroidal representation of Equation (81). Kelly *et al* recently came to a similar conclusion by considering only the $(\ell, m) = (3, 2)$ spherical multipole.

[9] These figures were calculated using the $\ell = m = 5$ QNM frequency for an equal mass nonspinning binary black hole coalescence. In the same case, we find that there are ~ 111 points temporally and ~ 14 points spatially within the typical amplitude decay rate. Because QNM frequency decreases as final spin decreases, these numbers increase as the initial binary becomes more unequal (e.g. Figure (11)).

[10] Importantly, as will be discussed in Sec. 5.3.1, they are also well localized in the frequency domain, which allows us to effectively filter them out during multimode fitting.

5.3 Multimode Fitting: From Spherical to Spheroidal

As discussed in the previous section, the single-mode fitting of spherical multipoles, $\psi_{lm}^{\rm NR}$, results in relatively significant residual errors (greater than 5%) that are systematic in final black hole spin. This spin-systematic behavior verifies the hypothesis encapsulated by Equation (83): Numerical Relativity ringdown is not a single QNM, but a sum of QNMs. We are therefore motivated to pursue a multimode fitting approach to describe QNM excitations for different mass-ratios. In particular, we will seek to extract spheroidal information from the spherical harmonic multipoles of Numerical Relativity waveforms.

By noting that the general fitting problem is multilinear in the set of decaying sinusoids given by perturbation theory (Equation 83), we present a method based upon ordinary linear least-squares fitting (OLS) to estimate spheroidal QNM amplitudes within each spherical multipole. We find that this particular choice of fitting routine (e.g. the least-squares approach used here) is not as important as its surrounding algorithm which aims to significantly reduce the problem's complexity. This is, in part, accomplished by utilizing a standard *greedy* algorithm in addition to OLS fitting. We refer to our approach as the *greedy-OLS* method.

For reference, we test our method with artificial data within artificial numerical noise to present a brief comparison between our *greedy-OLS* method and the modified Prony method [109, 113] in Sec.5.3.2. We then present estimates of the QNM excitations due to initially nonspinning black hole binaries of variable mass ratio.

5.3.1 Multimode fitting method

We have developed and implemented the following fitting procedure to estimate QNM amplitudes:

a. Given the set of $\psi_{lm}^{\rm NR}$, we define ringdown to be the region $\{T_0 \leq t \leq T_1\}$ relative to the peak luminosity of $\psi_{22}^{\rm NR}$ [79]. Because the following procedure involves taking the discrete Fourier transform, each ringdown waveform is appropriately windowed at the noise floor, and padded to ensure consistent frequency domain resolution.

b. Following Equation (83), we assert that Numerical Relativity ringdown, $\psi^{\rm NR}_{l'm}$, may be well approximated by sum of QNMs. As our numerical waveforms are of limited accuracy, we consider this sum to be finite:

$$\begin{aligned} \psi^{Fit}_{\rm j}(t) \;&=\; \sum_{k}^{N} A^{Fit}_{k}\, \sigma_{k\rm j}\, e^{i\tilde{\omega}_k t} \\ &\approx\; \psi^{\rm NR}_{l'm} \end{aligned} \tag{89}$$

where

$$\rm j \;\longleftrightarrow\; \{l', m\} \tag{90}$$

and

$$k \;\longleftrightarrow\; \{l, m, n\}. \tag{91}$$

While Equation (89)'s A^{Fit}_k is the estimate QNM amplitude, for notational simplicity we will henceforth refer to it as A_k. Moreover, the above summation is only over $\{l, l', n\}$, as m is fixed by Equation (83).

Here, the apparent horizon may be used to estimate the black hole's final mass and spin, M_f and $j_f = \frac{s_f}{M_f^2}$ [8]. Alternatively, one may estimate the final black hole mass and spin by optimizing the multimode fit of a single $\psi^{\rm NR}_{lm}$, as each QNM frequency is determined by M_f and j_f (Appendix C). Specifically, the dependence of the QNM frequencies on M_f and j_f may be utilized by either direct calculation (e.g. [40]), as used here, or by phenomenological fit (e.g. [89])[11].

c. In the language of least-squares fitting, we seek to cast Equation (89) in the form of a set of *normal equations*:

$$\alpha_{\rm ij} \;=\; \sum_{k}^{N} \mu_{\rm i}{}_k\, \beta_{k\rm j} \tag{92}$$

or equivalently,

$$\vec{\alpha}_{\rm j} \;=\; \hat{\mu}\, \vec{\beta}_{\rm j}\ . \tag{93}$$

[11] We find these two approaches to nominally agree to within 1% of each other (Appendix C).

To do so, we choose to make the following series of definitions:

$$\beta_{k\mathrm{j}} \equiv A_k \, \sigma_{k\mathrm{j}} \tag{94}$$

$$\alpha_{\mathrm{ij}} \equiv \frac{1}{\tilde{\omega}_{\mathrm{i}}} \int_{T_0}^{T_1} e^{-i\omega_{\mathrm{i}} t} \cdot \psi_{\mathrm{j}}^{\mathrm{NR}}(t) \, \mathrm{d}t \tag{95}$$

$$\mu_{\mathrm{i}k} \equiv \frac{1}{\tilde{\omega}_{\mathrm{i}}} \int_{T_0}^{T_1} e^{-i\omega_{\mathrm{i}} t} \cdot e^{i\tilde{\omega}_k t} \, \mathrm{d}t \tag{96}$$

where $\mathrm{i} \leftrightarrow \{l, m, n\}$ and $\hat{\mu}$ is an $N \times N$ complex valued matrix. The consistency of Eqs. (94)-(96) with Equation (92) is evident upon plugging Equation (89) into Equation (95).

If $\hat{\mu}$ is nonsingular, then the complex fitting amplitudes are given by

$$\vec{\beta}_{\mathrm{j}} \;=\; \hat{\mu}^{-1} \, \vec{\alpha}_{\mathrm{j}} \; . \tag{97}$$

Recalling that Equation (94) defines $\vec{\beta}_{\mathrm{j}}$ in terms of the complex QNM amplitudes, we equivalently have that estimates for the spheroidal coefficients in Equation (89) are given by the kth element of $\vec{\beta}_{\mathrm{j}}$

$$A_k \, \sigma_{k\mathrm{j}} \;=\; (\vec{\beta}_{\mathrm{j}})_k \;=\; (\hat{\mu}_N^{-1} \, \vec{\alpha}_{\mathrm{j}})_k \; .$$

In effect, Eqs. (94)-(96) entail taking the Fourier transform of the ringdown waveform, and performing semianalytic, linear least-squares fitting in the basis of damped sinusoids allowed by perturbation theory.

This approach imposes that ψ_{lm}^{NR} be composed of the QNM frequencies of perturbation theory rather than treating them as fitting parameters, and therefore, the total dimensionality of the fitting problem is reduced from $4 \times N$ to $2 \times N$: $\{\, Re[\beta_{k\mathrm{j}}],\, Im[\beta_{k\mathrm{j}}],\, N\}$. However, since Equation (97) allows for the simultaneous determination of $\beta_{k\mathrm{j}}$'s real and imaginary parts, the problem has effectively been reduced to $1 \times N$ dimensions. But note that the problem is not truly linear in N, as the fit must be optimized over all likely combinations of QNMs allowed by perturbation theory (Equation 83).

d. To manage this last optimization, we first limit the set of allowed QNMs to those whose $\sigma_{l'lmn}$ is above $5 \cdot 10^{-3}$ (Equation 84). This choice is practically equivalent to only allowing l to differ from l' by at most 2, and simultaneously limits the largest allowed

fitting frequency to be well below that of the non-QNM features discussed in Sec. 5.2.3. We then use a *greedy* [12] algorithm to estimate the optimal set of N QNMs for each $\psi_{lm}^{\rm NR}$. We choose to guide the greedy process by using Equation (88) averaged over different overlapping fitting regions [13].

e. Once the optimal set of QNMs has been found, we estimate the spheroidal QNM amplitudes from Eq. 94),

$$A_k = \frac{\beta_{k\rm j}}{\sigma_{k\rm j}} \,. \tag{98}$$

f. To quantify the effect[14] of T_0 on A_k, we perform the above process for $T_0 = \{6, 7, 8, ..11, 12\}(M)$ and then rescale each $A_k|_{T_0}$ using the corresponding QNM decay rate such that A_k is relative to $T_0 = 10(M)$. The resulting set, $\{A_k\}_{T_0}$, describes how much each recovered A_k agrees with our assumption that the choice of fitting regions corresponds to QNM dominated ringdown. For example, in the ideal case, where the fitting region contains only QNMs, every element $\{A_k\}_{T_0}$ would have the same value.

Throughout this chapter, we describe the fitting region dependence of our results using error bars of width $\frac{1}{2}\text{Range}(\{A_k\}_{T_0})$, where $\text{Range}(\{x_k\}) = \max(\{x_k\}) - \min(\{x_k\})$. In Figure (13), a scaling factor of $\frac{1}{6}$ is used. Error bars for nonamplitude quantities have been calculated in a similar fashion. We choose to represent the error bars according to the range of values because the data of interest are inherently systematic, not random (Appendix B).

Now, for reference, we proceed by touching base with an alternative multimode approach of interest [109, 115], the modified Prony method [113].

[12] Our greedy algorithm builds a list of N QNMs by starting with $N = 1$, and adding only QNMs to $\hat{\mu}_N$ that reduce the fit error (Equation 88). This process continues iteratively until the addition of at most two QNMs does not better the fit significantly, or causes the fit to become worse. A broader description of greedy algorithms may be found in [114].

[13] In particular, we average ϵ_{lm} over 15 fitting regions whose starting time is equally spaced between T_0 and $T_0 + 20(M)$. Each ϵ_{lm} is calculated by evaluating Equation (97) and Equation (88) on the sub-region.

[14] Please see Sec. 5.5.1 for a somewhat expanded discussion.

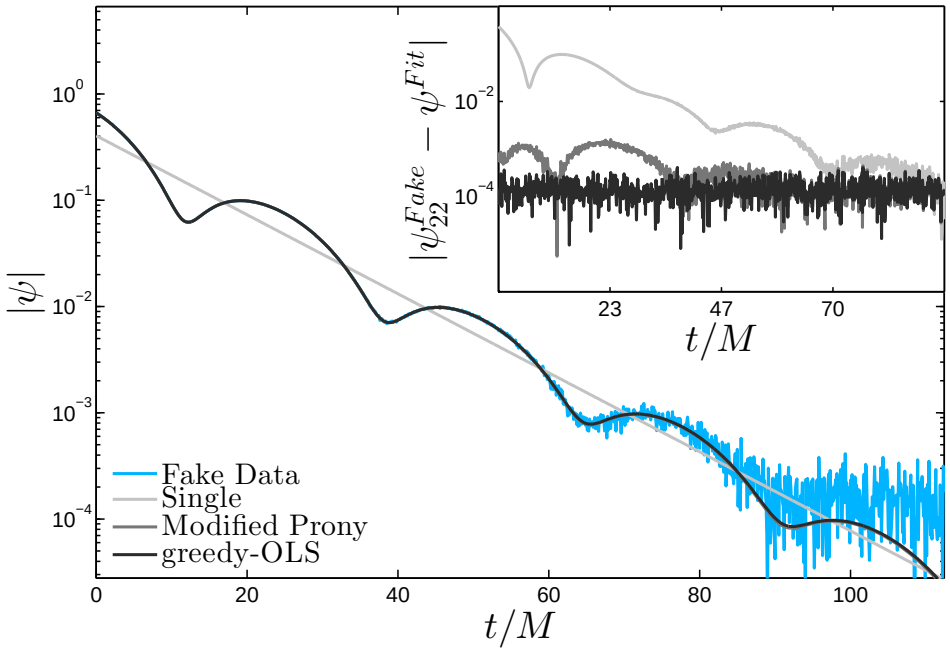

Figure 14: Time domain comparison of different fitting methods for artificial multimode data.

5.3.2 Multimode fits

Before using the *greedy-OLS* algorithm developed in the preceding Sec., we compare it with a popular method for recovering damped sinusoids within noise that linearizes the fitting problem by framing each QNM as the root of a complex polynomial. If the number of data points is greater than the number of modes, this approach is called the modified Prony algorithm [113, 109]. In this Sec. we consider test data to demonstrate what we find to be the typical advantages of approaches like the the *greedy-OLS* algorithm. In particular, we ask: given fake data, ψ_{22}^{Fake}, of known QNM composition, which algorithm returns the input QNMs and achieves the best fit?

To portray a typical answer to this question, we construct ψ_{22}^{Fake} to be composed of the $(\ell, m, n) = \{(2,2,0), (3,2,0), (2,2,1)\}$ QNMs with the addition of Gaussian noise[109] that is 10^{-5} times smaller than the largest component amplitude. As the modified Prony algorithm treats QNM frequency and decay time as free parameters, we label each output

Table 1: Recovered QNMs and errors when applying different fitting methods to artificial ringdown data composed of the $(\ell, m, n) = \{(2,2,0), (3,2,0), (2,2,1)\}$ QNMs within Gaussian noise. Residual errors were calculated using Equation (88).

Method	Recovered QNMs (l, m, n)	ε
Single (Sec.5.2.1)	(2,2,0)	6.00×10^{-1}
Modified Prony[113, 116]	(2,2,0),(3,2,0)	4.49×10^{-3}
Greedy-OLS (Sec.5.3.1)	(2,2,0),(3,2,0),(2,2,1)	1.19×10^{-3}

frequency by its nearest QNM frequency.

Figure 14 compares the output of the *greedy-OLS* method to the results of the modified Prony algorithm [113] and the single-mode fitting algorithm described in Sec.5.2.1. Table 1 lists the recovered QNMs and corresponding residual errors (Equation (88)). While both the modified Prony and *greedy-OLS* methods produce qualitatively precise fits, the inset of Figure (14) shows that the Prony method incurs a noticeably higher residual error. Turning to Table 1, we see that this larger residual error corresponds to the Prony method's not capturing the $(\ell, m, n) = (2, 2, 1)$ overtone. This missing mode illuminates two related disadvantages of Prony methods when applied to QNM analysis:

a. The treatment of QNM frequency (Equation (78)) as a free parameter increases the difficulty in assigning output frequencies to those predicted by perturbation theory.

b. The method's output frequencies are susceptible to spurious deviations from the structure predicted by black hole perturbation theory. This aspect of the algorithm complicates the process of estimating black hole final mass and spin [89].

For these reasons, throughout the sections that follow, we favor the *greedy-OLS* algorithm. However, we must also note that any fitting algorithm that uses prior information from perturbation theory to perform multimode fitting may be just as effective. For example, we find that using the Levenberg-Marquardt algorithm[117], in place of Equation (97), is just as potent at estimating the QNM terms in Equation (89), but only if fitting frequencies are limited to those predicted by perturbation theory.

Now, with some confidence in the *greedy-OLS* method's faithfulness to the QNM content

of ringdown data, let us consider two applications to Numerical Relativity ringdown. Figure 15 shows results for the $l = m = 2$ (top row) and $l = m = 4$ (bottom row) spherical multipoles of a 2:1 mass-ratio initially nonspinning binary black hole system. The four dots in Figure (15)'s top left panel are the recovered QNMs for $\psi_{22}^{\rm NR}$, indicating that $\psi_{22}^{\rm NR}$ is dominated by four QNMs.

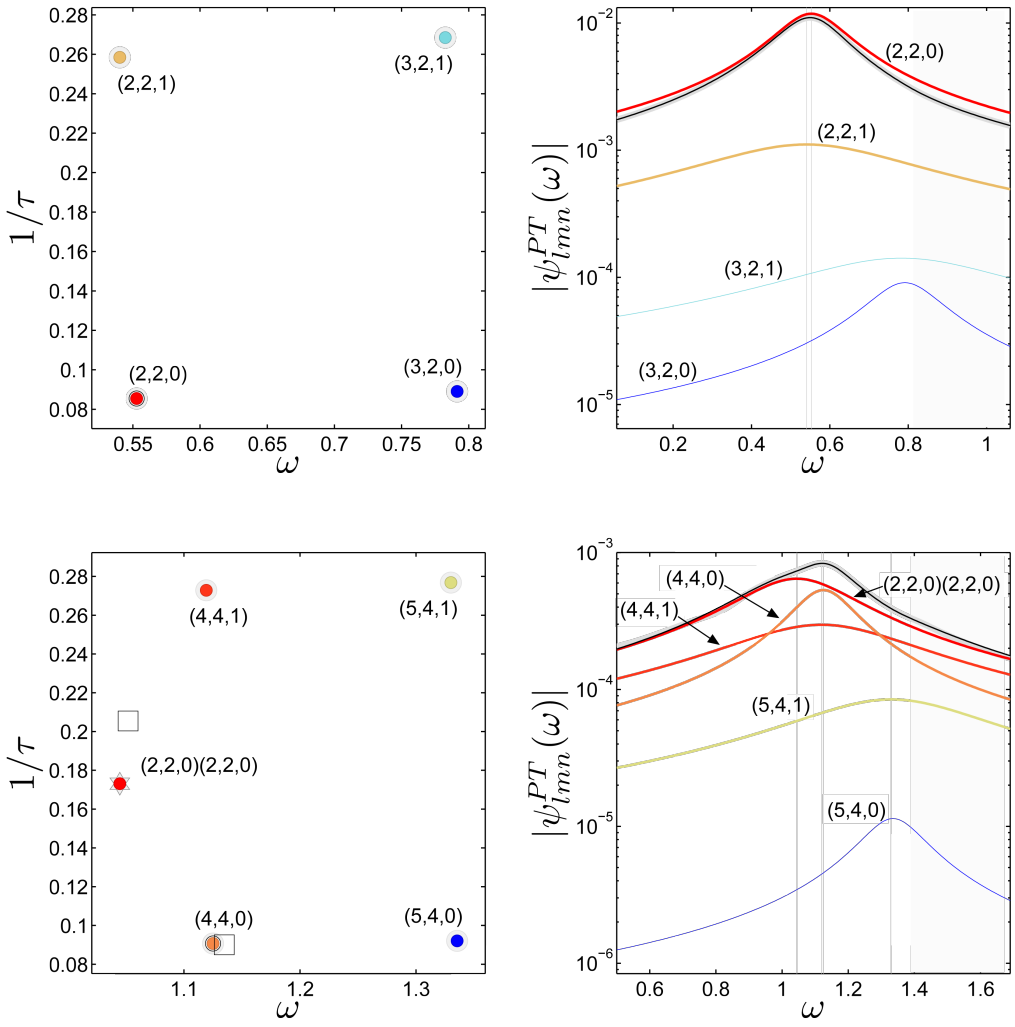

Figure 15: Top Panels: multimode fitting results for $\psi_{22}^{\rm NR}$. Bottom Panels: multimode fitting results for $\psi_{44}^{\rm NR}$. Left: QNMs recovered, plotted in central frequency and decay time. Each point is labeled with its QNM index in (ℓ, m, n) format. Right: Frequency domain envelopes of component QNMs (color), Numerical Relativity data (grey), and total fit (black). Within each right panel, the shaded region denotes the frequency cut-off. Points in the left panels correspond to curves in the right panels of the same color and QNM label. For reference, we have overlayed the results of the modified Prony method in Figure (15)'s lower left panel.

Similarly, $\psi_{44}^{\rm NR}$ appears to be dominated by five QNM terms. As expected from single-mode fitting, the fundamental modes generally dominate. However, multimode fitting reveals overtones, and in the case of $\psi_{44}^{\rm NR}$, an apparent second order QNM. For reference, we have overlayed the results of the modified Prony method in Figure (15)'s lower left panel.

Importantly, like our test case (Table 1), the residual errors for these cases are ~ 10 times smaller than single-mode fitting. We find this to be generally true for initially nonspinning binary black hole systems of symmetric mass-ratio between 0.2500 and 0.0586. In the following section, we use these cases to peer into the new information captured by multimode fitting. We model the mapping between initial binary mass-ratio and QNM excitation.

5.4 Mapping QNM Excitation with Symmetric mass-ratio

We apply the *greedy-OLS* algorithm to the ringdown of quasicircular initially nonspinning binary black hole systems of symmetric mass-ratio between 0.2500 and 0.0586. The result is a map between η and A_{lmn}. Just as in the case of inspiral, with its reflective symmetry about the orbital plane, we find that $|A_{lmn}| = |A_{l-mn}|$ for all systems considered; therefore, we only focus on the $m > 0$ multipoles.

By applying the *greedy-OLS* algorithm to our Numerical Relativity ringdown, we are able to catalog the mass-ratio dependence of overtones and apparent second order QNM. We find that, for the initially nonspinning systems studied here, the *mirror modes* are not significantly excited.[15] While many well-resolved QNMs are recovered, for practicality, we only focus on those needed to represent ψ_4 ringdown up to marginal accuracy. We consider these to be QNMs found within the dominant $l = m$ and $l = m + 1$ spherical multipoles (e.g. $\psi_{lm}^{\rm NR}$), where $l \leq 4$ [9, 112, 118]. We go on to present a robust phenomenological model for the mapping between η and A_{lmn}. We start by touching base with current models for $A_{lmn}(\eta)$.

The phenomenological models proposed by [9] are shown in Figure (13). This class of model is derived from the *single-mode* fitting approach mentioned in Sec.5.2, and only

[15] We will discuss in Sec. 5.5 that imposing these modes detracts from the consistency of our results with perturbation theory

handles $|A_{lmn}|$ while leaving its complex phase to be matched to the phase of $\psi^{\rm NR}_{lm}$ after merger [16]. While the model functions used in [9] capture the qualitative behavior of the first few fundamental QNMs, the current study's increased resolution in mass-ratio reveals clear systematic deviations from Numerical Relativity results (Figure (13), left panel). Most prominently, the local minimum in $|A_{440}|$ is not captured by

$$|A_{440}| \,=\, a\,|\tilde{\omega}_{440}|^2 \left(\frac{\rm m_1}{\rm m_2}\right)^{\frac{3}{4}} \, e^{-\,b\,\frac{\rm m_1}{\rm m_2}}\,.$$

The more recent work of [83] focuses on the $(l, m, n) = (3, 2, 0)$ mode, and proposes a qualitatively precise model for $|A_{320}(\eta)|$,

$$|A_{320}| \,=\, \sqrt{(a - b\,e^{-\lambda/\eta})^2 + c^2}\,, \tag{99}$$

where a, b, c, and λ are real valued constants. Despite the success of this map[17], it is not immediately clear why this functional form works so well, and how its effectiveness may be extended to the other QNMs.

Ultimately, a thorough analytic study of QNM excitation, akin to [101], may be needed to *derive* the mapping between η and A_{lmn}. While such a pursuit is beyond the current study, a connection between $A_{lmn}(\eta)$ and known physics is appropriate.

To approach this problem, we maintain that QNM excitations are, like their Post-Newtonian counterparts, best described by an expansion in the initial binary's parameters. Here we expand upon [93] by considering a beyond leading order summation in symmetric mass-ratio.

[16] On the other hand, a multimode representation of each $\psi^{\rm NR}_{l'm}$ (Equation (83)) requires information about both $|A_{lmn}|$ and its complex phase

[17] Please see Figure (10) of [83].

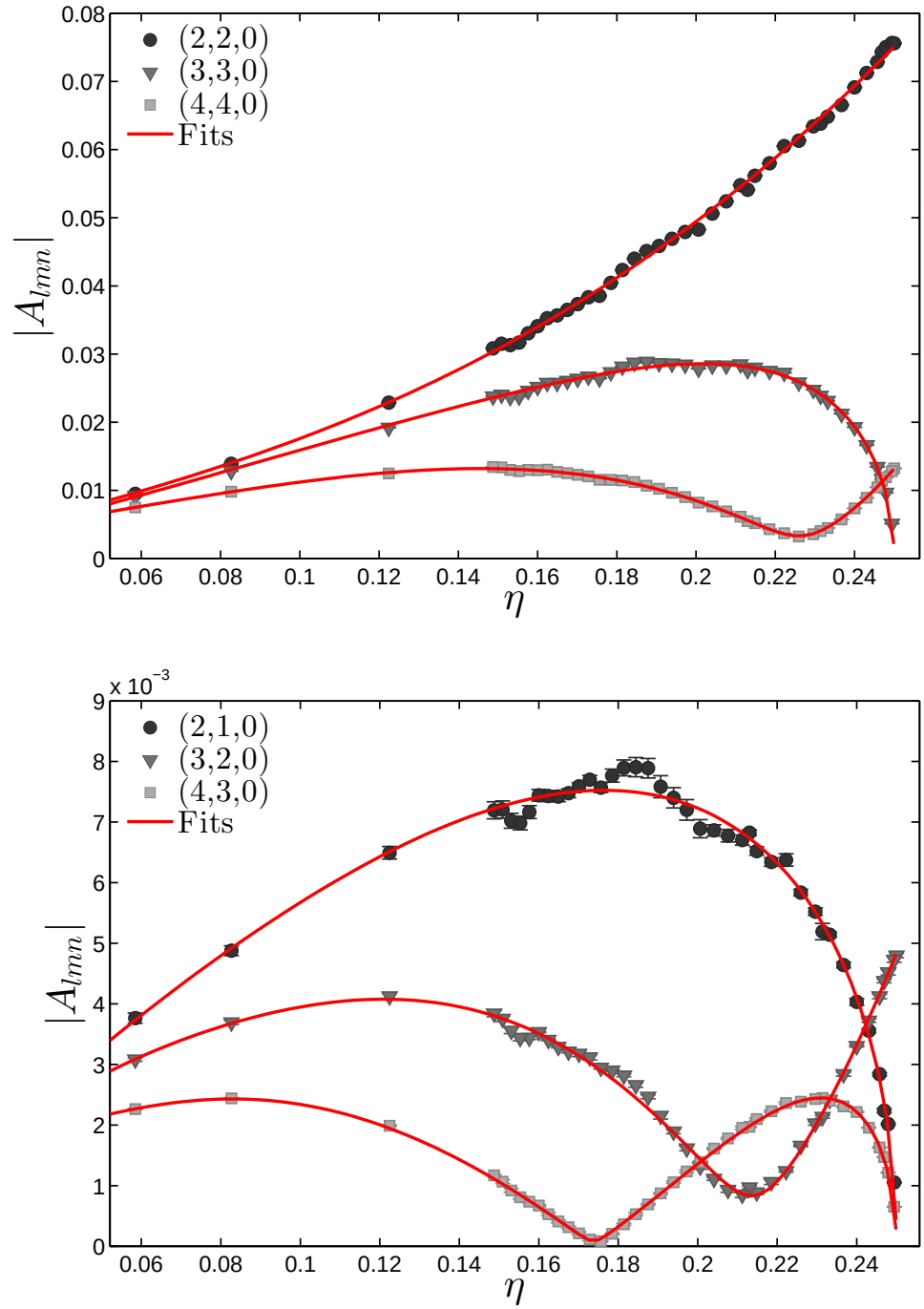

Figure 16: Select fundamental Quasinormal Mode amplitudes. The error bars were calculated as described in Sec. 5.3.1- f.

First, we note that the relevant[18] Post-Newtonian *strain* multipole moments may be written in the form

$$h_{lm} \;=\; \eta\, e^{-im\phi(t)}\; \delta_m(\mathrm{m}_1, \mathrm{m}_2) \sum_{u=0} b_u\, \eta^u \tag{100}$$

where

$$\delta_m(\mathrm{m}_1, \mathrm{m}_2) \;\equiv\; \frac{|\mathrm{m}_1 + (-1)^m \mathrm{m}_2|}{\mathrm{m}_1 + \mathrm{m}_2} \tag{101}$$

and ϕ is the time dependent part of the waveform's complex phase [119, 25]. In seeking to generalize Equation (100) to ψ_4 QNM excitations, we may begin by expecting that during ringdown, $\phi(t)$ becomes $\phi_{lmn} = \tilde{\omega}_{lmn} t + \mathit{constants}$ (we revisit this idea in Sec. 5.4.1). Furthermore, since ψ_4 and strain are related through two time derivatives, the ψ_4 ringdown analogue of Equation (100) would pick up a factor of

$$\tilde{\omega}^2_{lmn} = |\tilde{\omega}^2_{lmn}| e^{-\varphi_{lmn}} \; .$$

Lastly, rather than Equation (100)'s overall scaling by η, we find it useful to impose that the excitation of each nth overtone be proportional to η^n.

Gathering all of these ideas, we propose that, for ψ_4 QNM excitations, Equation (100) generalizes to

$$\begin{aligned} A_{lmn} \;&=\; \tilde{\omega}^2_{nlm}\, \delta_m(\mathrm{m}_1, \mathrm{m}_2)\, \eta^{1+n} \sum_{u=0} a_u\, \eta^u \\ &=\; e^{-i\phi_{lmn}}\, |A_{lmn}| \end{aligned} \tag{102}$$

where

$$\phi_{lmn} \;\equiv\; \vartheta_{lmn} \;+\; 2\,\varphi_{lmn} \tag{103}$$

and

$$a_u = |a_u| e^{i\alpha_u} \; . \tag{104}$$

While we have chosen to encapsulate the intrinsic α_u contribution (Equation (104)) within ϑ_{lmn}, one might also expect additional extrinsic contributions to ϑ_{lmn} from the

[18] nonspinning, non-precessing, quasicircular compact binaries.

construction of each simulation (e.g. initial binary separation) [111]. Our approach to these dependencies is outlined in Sec.5.4.1.

We also notice that our Post-Newtonian inspired model has the immediate advantage of constraining the QNM amplitudes to be zero in the extreme mass-ratio limit, $\eta \to 0$, while imposing that only even m QNMs are excited in the equal-mass case where $\delta_m = 0$. As a more phenomenological point, we have chosen to model the overtone dependence as an increasing proportionality in η to better fit the Numerical Relativity data.

With these conceptual tools at hand, we may now apply Equation (102) to Numerical Relativity ringdown by constructing a fit for the complex valued A_{lmn}, as a function of η.

5.4.1 Constructing a fit for A_{lmn} on η

In order to accurately model ringdown according to Equation (81), both $|A_{lmn}|$ and the overall phase, ϕ_{lmn} must be represented. To do so, let us start by focusing on the aspects of Equation (102) not given by perturbation theory. First, we rearrange Equation (102) to define

$$\begin{aligned} C_{lmn} &\equiv \frac{A_{lmn}}{\eta^{1+n}\ \tilde{\omega}_{lmn}^2\ \delta_m(\mathrm{m}_1, \mathrm{m}_2)} \\ &= \sum_{u=0} a_u\, \eta^u\ . \\ &= |C_{lmn}|\ e^{i\,\vartheta_{lmn}} \end{aligned} \tag{105}$$

As we expect C_{lmn} to be a polynomial with complex coefficients, it might be well captured by standard least-squares fitting methods; however, we are wary that this approach will be ineffective if ϑ_{lmn} is not dominated by the phase of the polynomial sum[19].

[19]For simplicity, we will not separate the Kerr eigenvalues (e.g. the excitation factors [120]) out from the net QNM excitation, A_{lmn}. The result is that the polynomial in question approximates the product of two functions. One, the excitation factor, is independent on the initial parameters. The other is entirely dependent on the initial parameters.

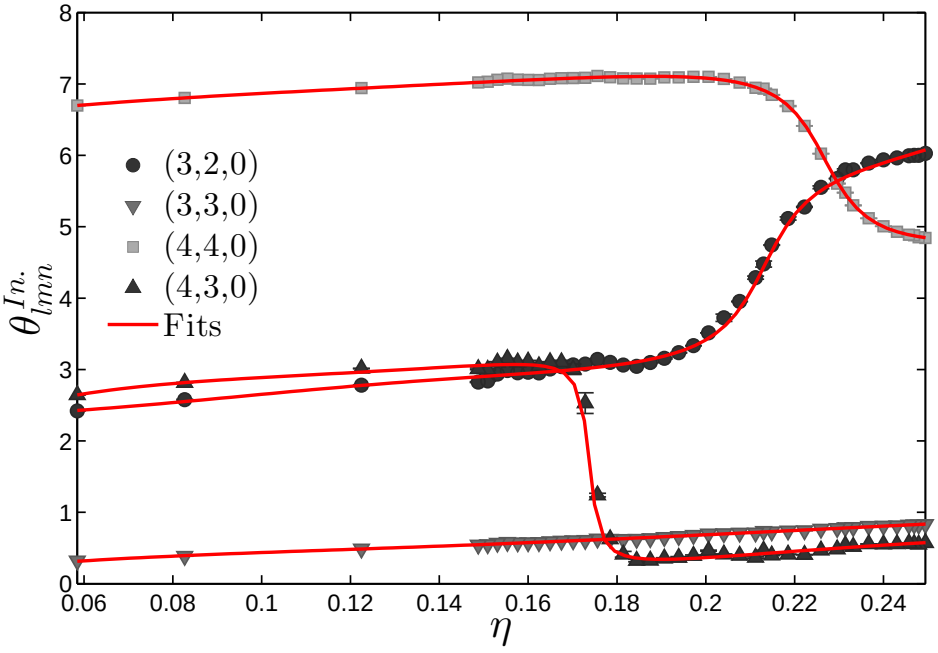

Figure 17: Examples of phases relative to $m\phi_{22}/2$.

With this in mind, if we refer to the intrinsic polynomial phase as $\vartheta^{In.}_{lmn}$, and the additional extrinsic contribution as $\vartheta^{Ex.}_{lmn}$, then

$$\vartheta_{lmn} \;=\; \vartheta^{Ex.}_{lmn} \;+\; \vartheta^{In.}_{lmn}\;. \tag{106}$$

Physically, if there is a preferred azimuthal direction postmerger, then one might expect it to dominate $\vartheta^{Ex.}_{lmn}$.

In practice, we find this preferred direction is set by the kick velocity. For the simulations considered here, the kick velocity is always within the orbital plane of the initial binary, giving $\vec{v}_{kick} = v_x\hat{x} + v_y\hat{y}$. The direction of the kick velocity with respect to the simulation frame is then $\phi_{kick} = \tan^{-1}(v_y/v_x)$. In this sense, we find that the extrinsic part of C_{lmn}'s complex phase is given by

$$\vartheta^{Ex.}_{lmn} \;=\; m\,(\phi_{kick} + \phi_0)\;. \tag{107}$$

Together with Equation (106) and Equation (103), we now have that

$$\phi_{lmn} \;=\; \vartheta^{In.}_{lmn} \;+\; m\,(\phi_{kick} + \phi_0) \;+\; 2\,\varphi_{lmn}\;. \tag{108}$$

Note that changes in the line of sight about the black hole's final spin direction affect ϕ_{lmn} and $m\,\phi_{kick}$ in the same way. Put differently, redefining Equation (80)'s to be $\phi = \phi' - \delta\phi$ effectively adds $m\delta\phi$ to both sides of Equation (108). This leaves Equation (108)'s ϕ_0 as an orientation independent quantity (e.g. independent of the observer's location in the initial binaries orbital plane).

However, ϕ_0 is not purely intrinsic. As we have written it in Equation (108), ϕ_0 not only encapsulates the difference between the final kick orientation and QNM phase, but also how each QNM's phase has evolved up to the start of the fitting region , $t_* = T_0$. This is discussed further in Sec. 5.5.1.

Using the $(l, m, n) = (2, 2, 0)$ QNM, we find that

$$\phi_0 \equiv \frac{\vartheta^{Ex.}_{lmn}}{m} - \phi_{kick} \approx \frac{\phi_{220}}{2} - \phi_{kick} \; . \tag{109}$$

This gives $\phi_0 = -2.39 \pm 0.10 \; rad.$ The regularity of approximation across different mass-ratios is briefly discussed in Sec. 5.5.3.

Together, Eqs. (103)-(109) reveal the intrinsic polynomial phase to be

$$\begin{aligned} \vartheta^{In.}_{lmn} &\approx \phi_{lmn} \; - \; (2\varphi_{lmn} + m(\phi_{kick} + \phi_0)) \\ &\approx \phi_{lmn} - \; (2\varphi_{lmn} + m\frac{\phi_{220}}{2}) \; . \end{aligned} \tag{110}$$

We may therefore construct C_{lmn} by evaluating Equation (110), and applying it to the magnitude of $|C_{lmn}|$ given by Equation (105). This allows for the *simultaneous* least-squares fitting of C_{lmn}'s magnitude and phase. Here we have used `MATLAB`'s polyfit.m. By increasing the order of the polynomial fit until the residual error (Equation 88) changes by less than 10%, we find that C_{lmn} are well fit by polynomials of order $\ell - 1$ for the considered range of η. Figure 16 displays the broad effectiveness of our fitting C_{lmn}, and then transforming back to A_{lmn} to calculate $|A_{lmn}|$. Similarly, Figure (17) displays the corresponding intrinsic phases and their fits.

For each local minimum in Figure (16), there is a corresponding *phase transition* in Figure (17). In an approximate sense, this suggests that each C_{lmn} may be more appropriately represented as a polynomial function of $(\eta - \eta_0)$, which would force $\eta = \eta_0$ to be a local

minimum. However, for simplicity, we have tabulated all fitting coefficients according to Equation (105).

All fitting coefficients are given in Appendix A.

5.4.2 Beyond the fundamentals: overtones & second order modes

Figure 18 displays estimates for the QNM amplitudes of overtones (top panel) and second order modes (bottom panel) as recovered by the *greedy-OLS* algorithm. While their existence has been discussed in previous studies (e.g [85, 94, 95, 96, 97, 82, 86, 80, 87]), we present for the first time their characterization with symmetric mass ratio.

The fitting polynomials for the overtones were found to be of order $l-1$ in η. The $(l,m,n)=(4,4,1)$ case is a clear exception, requiring at least an eighth order fit. While we find that many of our estimates of $|A_{lmn}|$ display a localized increase between $0.18 \geq \eta \geq 0.17$, $|A_{441}|$ displays a significant decrease which makes its η dependence possibly inconsistent with Equation (102). As discussed in Sec.5.5.1, this is likely due to the definition of ringdown start time in terms of the initial rather than final mass scale.

Given the limitations of our Numerical Relativity runs, we consider these oscillations to be numerical, rather than physical. A similar oscillating trend is observed in the apparent $(l_1,m_1,n_1)(l_2,m_2,n_2) = (2,2,0)(2,2,0)$ excitation (Figure 18). We discuss the likely source for these oscillations in the next section (Sec. 5.5.3).

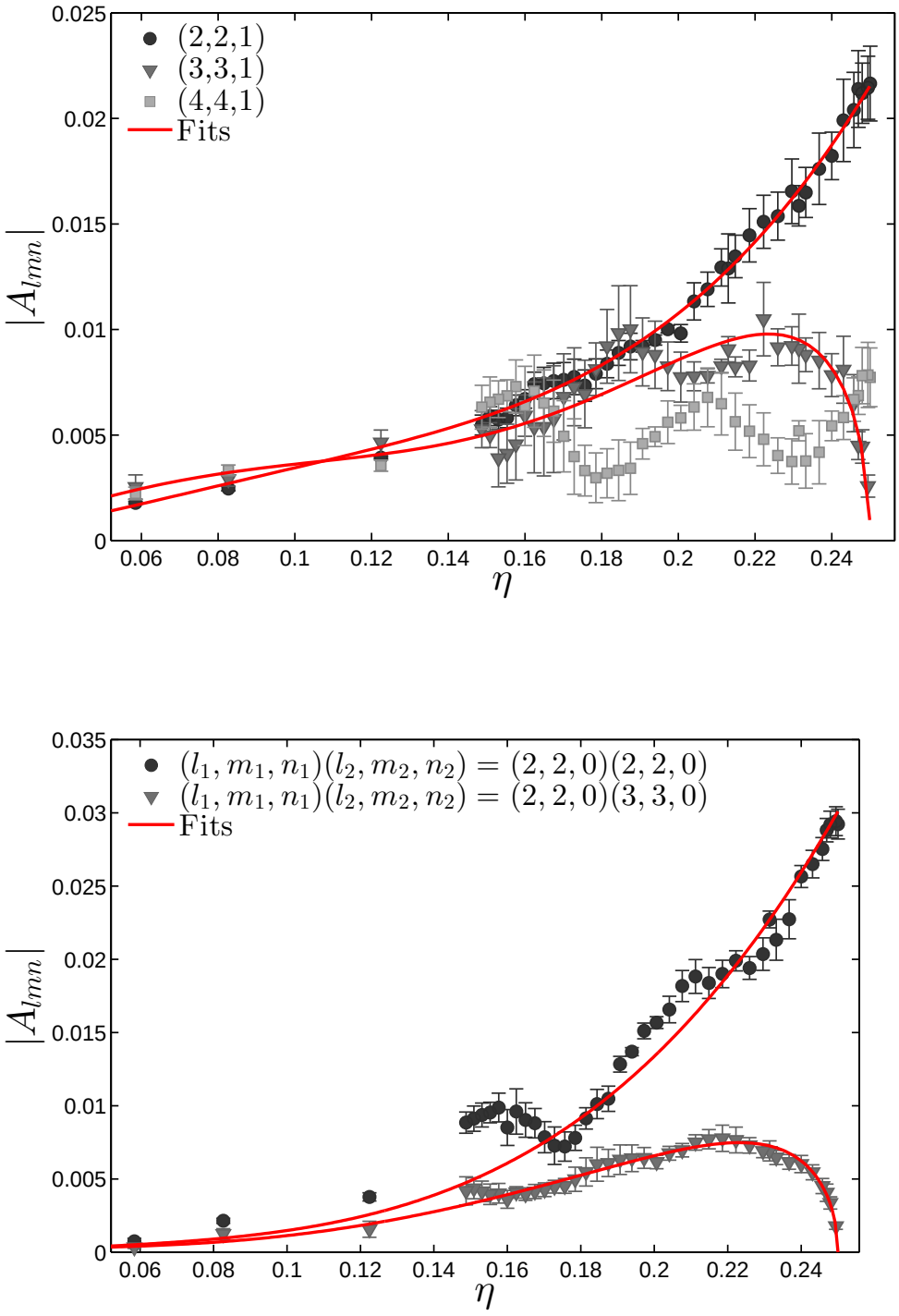

Figure 18: Estimated overtone (Top) and second order (Bottom) excitation amplitudes via multimode fitting. The error bars were calculated as described in Sec. 5.3.1- f.

While the overtones decay faster (e.g. Figure 15), their functional form largely mirrors their $n = 0$ counterparts (Figure 16). Similarly, the functional form of the second order modes appears consistent with the notion that each second order mode is largely driven by products of two first order modes [95]. Quantitatively, we expect that each $A_{(l_1m_1n_1)(l_2m_2n_2)}$ should be proportional to the product of some $A_{l_1m_1n_1}$ and $A_{l_2m_2n_2}$

$$A_{(l_1m_1n_1)(l_2m_2n_2)} \propto A_{l_1m_1n_1} A_{l_2m_2n_2} \quad . \tag{111}$$

Under this caveat, we model the second order modes according to

$$\begin{aligned} A_{(l_1m_1n_1)(l_2m_2n_2)} &= \mu_{(l_1m_1n_1)(l_2m_2n_2)} \\ &\times A_{l_1m_1n_1} \ A_{l_2m_2n_2} \ , \end{aligned} \tag{112}$$

where, given $A_{l_1m_1n_1}$ and $A_{l_2m_2n_2}$ from the first order fits, $\mu_{(l_1m_1n_1)(l_2m_2n_2)}$ is the only undetermined parameter.

Upon using a standard root finding algorithm to solve for $\mu_{(l_1m_1n_1)(l_2m_2n_2)}$, we find qualitatively good agreement between our raw estimates for $A_{(l_1m_1n_1)(l_2m_2n_2)}$ and Equation (112). While Figure (18) displays $(l_1m_1n_1)(l_2m_2n_2) = (2,2,0)(2,2,0)$ and $(2,2,0)(3,3,0)$ cases, other less dominant and poorly resolved candidates were detected.

All fitting coefficients are given in Appendix A.

5.5 Consistency with Perturbation Theory and Result Limitations

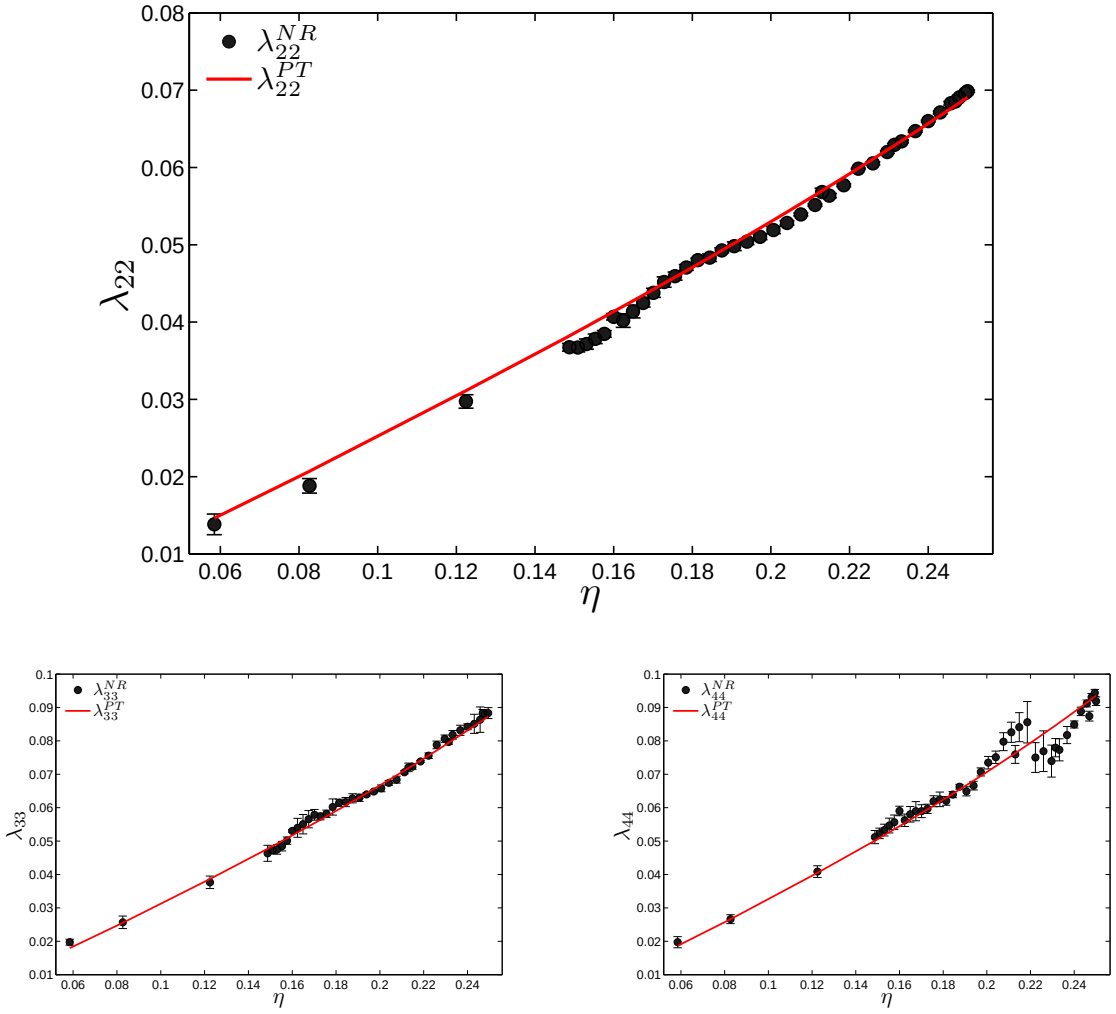

Figure 19: Top, bottom left, right: Ratio of inner-products between spherical and spheroidal harmonics estimated via multimode fitting and direct calculation. The error bars were calculated as described in Sec. 5.3.1- f.

While we have developed a method for the estimation of QNM excitation coefficients, this alone does not guarantee the consistency of our results with perturbation theory. This is primarily due to the fact that the QNMs and their related functions are not complete

(e.g. [121]). In particular, the decaying sinusoids are overcomplete, making it, in principle, possible to achieve an arbitrarily good fit to Equation (83) with many different combinations of decaying sinusoids. However, the effectiveness of the *greedy-OLS* method described in Sec. 5.3 hinges not on the completeness of the QNMs, but on the uniqueness of the Fourier transform (Equation 95), which the algorithm seeks to approximate up to numerical accuracy by focusing only on the sparse QNM frequencies suggested by perturbation theory[20].

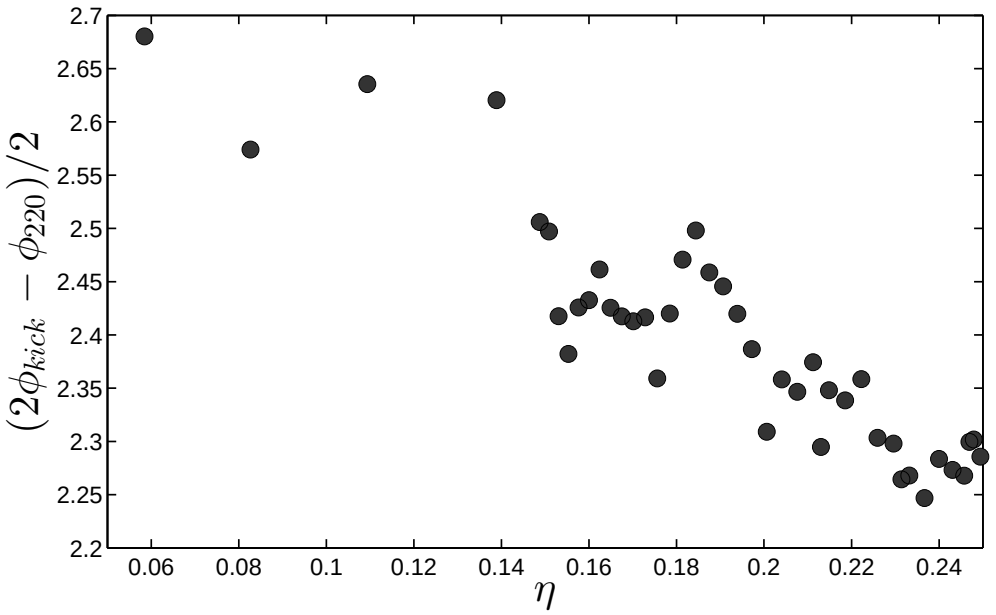

Figure 20: Difference between phase of $(l, m, n) = (2, 2, 0)$ QNM excitation ($10\,M$ after the peak luminosity in $\psi_{22}^{\rm NR}$) and the scaled kick direction, $m\phi_{kick}$ (Sec.5.4).

Even so, results for A_{lmn} may be intrinsically biased if the data are not actually dominated by QNMs. This is the case if the fitting region is chosen either too close to the merger regime, or so far away that irregular numerical noise dominates. For this reason, independent measures of the $|A_{lmn}|$'s consistency with perturbation theory are needed. In

[20] The *greedy-OLS* algorithm uses only a handful of frequencies to estimate the Fourier Transform at *all* frequencies. We find that applying the *greedy-OLS* algorithm with the QNM frequencies corresponding to a different physical spin does not yield good fits.

this section we consider two such measures, and discuss the limitations of our results.

5.5.1 Fitting region effects

The first estimate of consistency is mentioned at the end of Sec. 5.3.1-f: the effect of ringdown start time, T_0, on A_{lmn}. Here we will discuss the effect of T_0 on A_{lmn} from two perspectives.

Changing Scales.— On one hand, we may ask why defining T_0 relative to the peak luminosity of $\psi_{22}^{\rm NR}$ has been found to yield well-behaved maps between initial binary parameters and QNM excitations. For example, if one defines T_0 relative to the peak of $\psi_{22}^{\rm NR}$ rather than its luminosity, then seemingly irregular oscillations are introduced into the dependence of each fundamental mode's A_{lmn} on symmetric mass-ratio. This suggests that there is something about the peak luminosity that serves as a consistent reference for how the system is evolving in the ringdown regime. This postulate is supported by our analysis of each A_{lmn} phase in Sec. 5.4, where we found that when using the peak luminosity as a reference point, the complex phase of each A_{lmn} was dependent on m time the systems final kick direction with an offset of $m\phi_0$ that is largely independent of initial parameters (Equation 110). This means that the phase evolution of each ringdown waveform, relative to the time of the peak luminosity, is approximate for the systems considered here. In other words, the choice to measure time relative to the peak luminosity appears to be approximately the same as choosing T_0 such that ϕ_0 is constant.

However, there is a discrepancy here: we have chosen $T_0 = 10M$ in units of the system's Arnowitt-Deser-Misner (ADM) mass [98], not the final black hole mass M_f, meaning that while the physical scale of the system(M_f) changes, our reference length T_0 stays fixed. This along with the dependence of each QNM frequency on the final system state, $\{M_f, j_f\}$, should contribute to a systematically varying ϕ_0. The systematic dependence of ϕ_0 is shown in Figure (20) against η (η is proportional to j_f).

As with choosing the peak of $\psi_{22}^{\rm NR}$ rather than its luminosity as a reference point, we might expect seemingly irregular oscillations to appear in the dependence of some $|A_{lmn}|(\eta)$.

In particular, while further study is needed, the above argument is a likely explanation for the fluctuations of some modes around $\eta = 0.18$ (e.g. $|A_{320}|$ and $|A_{210}|$ in Figure (16), and the modes in Figure (18)).

Different Start Times.— On the other hand, different fitting regions incur different amounts of numerical noise which may bias results. Therefore we have chosen to quantify this measurement error by considering different fitting regions, and then rescaling our results to be relative to $T_0 = 10\,M$ after the peak in $\psi_{22}^{\rm NR}$'s luminosity. This measure of consistency answers the question "How much does the recovered QNM behave like a damped sinusoid?" and may be quantified by rescaling $A_{lmn}|_{T_0}$ according to its complex QNM frequency

$$A_{lmn}|_{T_0} \;\approx\; A_{lmn}|_{T_0'}\, e^{i\tilde{\omega}_{lmn}\,(T_0 - T_0')}\,. \tag{113}$$

In the ideal case, where the estimated A_{lmn} behaves exactly as a decaying sinusoid from T_0 to T_0', Equation (113) becomes an equality. This method was utilized to make the error bars throughout this chapter.

While we find that the effects of choosing different T_0 are inherently systematic[21], they are also indicative of an optimal start of ringdown that is generally about $10M$ after the peak luminosity in $\psi_{22}^{\rm NR}$ (Appendix B); however, in some cases the effective ringdown fitting may be performed up to $2M$ after the peak luminosity. An expanded description of fitting region effects is given in Appendix B.

5.5.2 Inner-product ratios

An additional consistency test may be performed by taking advantage of Equation (83) for different $\psi_{lm}^{\rm NR}$ [83]. Noting that any QNM may be found within multiple $\psi_{lm}^{\rm NR}$ of the same m, it follows that the ratio of their mixing coefficients may be estimated from fitting results, and then compared to analytic calculations via Equation (84).

For example, in the case of $\psi_{33}^{\rm NR}$ and $\psi_{43}^{\rm NR}$, Equation (83) gives that

$$\psi_{33}^{\rm NR}(t) \;=\; A_{330}\,\sigma_{3330}\,e^{i\tilde{\omega}_{330}t} \;+\; ...$$

[21] To the left of ringdown is the nonlinear merger, and to the right is numerical noise.

and

$$\psi_{43}^{\rm NR}(t) \;=\; A_{330}\,\sigma_{4330}\,e^{i\tilde{\omega}_{330}t} + A_{430}\,\sigma_{4430}\,e^{i\tilde{\omega}_{430}t} \;+\; ...$$

By comparing terms, and recalling that the *greedy-OLS* algorithm gives a measure for terms in the above sum via Equation (94)

$$\beta_{l'lmn} \;=\; A^{Est.}_{lmn}\,\sigma^{Est.}_{l'lmn}\,,$$

we see that the ratio, $\sigma_{l'lmn}/\sigma_{llmn}$ may be estimated directly from the results of multimode fitting. For brevity, we shall limit our discussion to the fundamental modes. For clarity, we will make a distinction between the perturbation theory result derived from Equation (84)

$$\lambda^{\rm PT}_{l'm} \;= \frac{\sigma_{l'lm0}}{\sigma_{llm0}}\,, \tag{114}$$

and the multimode fitting estimate

$$\begin{aligned}\lambda^{\rm NR}_{l'm} \;&= \frac{\beta_{l'lm0}}{\beta_{llm0}} \\ &= \frac{\sigma^{Est.}_{l'lm0}\,A^{Est.}_{lm0}}{\sigma^{Est.}_{llm0}\,A^{Est.}_{lm0}}\quad.\end{aligned} \tag{115}$$

The three panels of Figure (19) compare $\lambda^{\rm NR}_{lm}$ to $\lambda^{\rm PT}_{lm}$ for $l = m = \{2, 3, 4\}$. Because $\lambda^{\rm NR}_{lm}$ is insensitive to waveform phase, we have included results for three waveforms with lower symmetric mass-ratios.

While consistency between perturbation theory and our numerical results is seen in all cases, our estimate $\lambda^{\rm NR}_{44}$ does systematically deviate from $\lambda^{\rm PT}_{lm}$ by roughly 10% on $0.20 < \eta < 0.25$. As suggested by our discussion in Sec. 5.2.3, we consider this deviation to be the result of $|A_{440}|$ approaching the magnitude of numerical noise. Moreover, this deviation was found to be exacerbated by the addition of mirror modes(Sec. 5.1.2), the removal of the second order modes, or both.

5.5.3 Limitations of results

While finite spatial and temporal Numerical Relativity resolution limits the frequencies and multipoles that we are able to consider, we find that our results are stable with respect

to the resolutions discussed in Sec. 5.2.3. This also suggests that gauge and near-field effects are not significantly manifested for the majority of our results[22]. However our consideration of the apparent second order modes carries a more basic limitation: we currently lack detailed knowledge about their structure. Moreover, our lacking many simulations in the very unequal mass-ratio regime presents another limitation.

Second Order Modes.— As analytic calculations of second order Kerr QNMs are lacking, there exists a tension in the existing literature.

On one hand, analytic studies such as that of Ioka and Nakano [95] suggest that second order perturbations result in QNMs proportional by products of two first order modes. On the other hand, Pazos *et al* [96] found that, for spherically symmetric initial data, scalar wave scattering off of a Schwarzschild black hole results in second order excitations whose frequencies are *the same* as those of first order modes.

[22] See [83] for an expanded discussion.

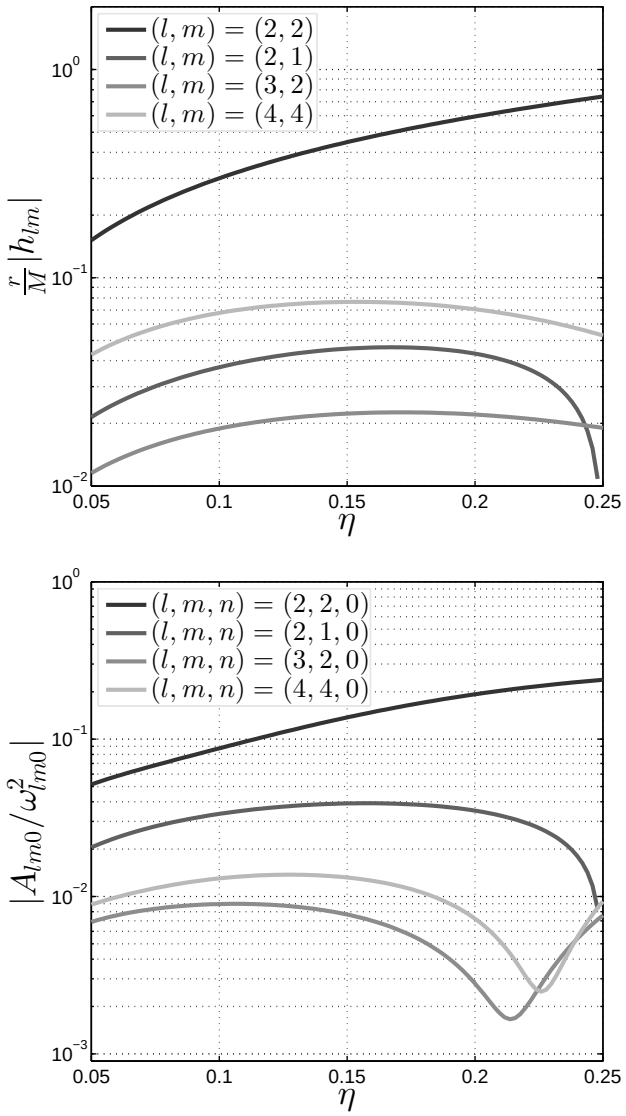

Figure 21: Comparison of the Post–Newtonian strain amplitudes with QNM amplitudes. Top: Amplitude of dimensionless Post-Newtonian strain for a selection of (ℓ, m) spherical multipoles. Values were calculated at $M\omega = 0.18$ using reference [11]. Bottom: Amplitude only fits for fundamental QNM excitations.

In this study (Sec. 5.4.2) we find second order excitations that appear to be largely driven by two first order QNMs, with frequencies that are sums of two first order frequencies. However, as our analysis approach has been designed to only extract spheroidal information

post-merger, it cannot directly untangle mode coupling effects that would be consistent with [96]. Therefore, our findings may indeed be consistent with both [96] and [95]. We expect that an analytic study, analogous to Leaver's work [40], but for second order Kerr perturbations [38], may elucidate the matter.

Among the subtleties that should be addressed, we expect the degeneracy of the sum and difference tone spectrum to play an important role: when considering the entire set of possible second order modes, one quickly finds exact or near degeneracies between QNM frequencies with $l_1 \neq l_2$ and $m_1 \neq m_2$. Here, the second order modes with the lowest $l = m$ indices, such as (2,2,0)(2,2,0) and (2,2,0)(3,3,0), are not only free from degeneracy at this level, but appear to be the most prominent.

On a more rudimentary note, we do caution that, for the apparent second order modes discussed in Sec. 5.4.2, the overall proportionality constants (see Appendix A) are surely biased by the numerical limitations discussed in this and previous sections.

Very unequal mass-ratios.— Lastly, in regards to our fits for QNM excitation on symmetric mass-ratio, a more basic limitation is the inability to include many points in the very unequal mass-ratio regime ($\eta < 0.15$). Therefore, while the fits presented in Sec. 5.4 have been constructed to adhere to the extreme mass-ratio limit, they are, conservatively, only valid within the presented range of η.

5.6 Discussion of Results

In this section, we comment on the potential relevance of subdominant QNMs to ringdown templates and the relevance of our results to perturbation theory.

5.6.1 Perturbation theory comments

Pending an analytic description of QNM excitation for initially nonspinning, quasicircular binary black hole merger, akin to [101], and a better understanding of the higher order Kerr spectrum, akin to [122], we have found that a Post-Newtonian-like prescription

effectively models QNM excitation for the systems studied. The success of this model suggests that a well-defined analytic description exists, and that its predictions may be directly compared to the fitting coefficients in Tables 4 and 5. When directly compared to its Post-Newtonian counterparts, our model also illuminates the qualitative differences between the inspiral regime, where Post-Newtonian is valid, and the postmerger ringdown regime.

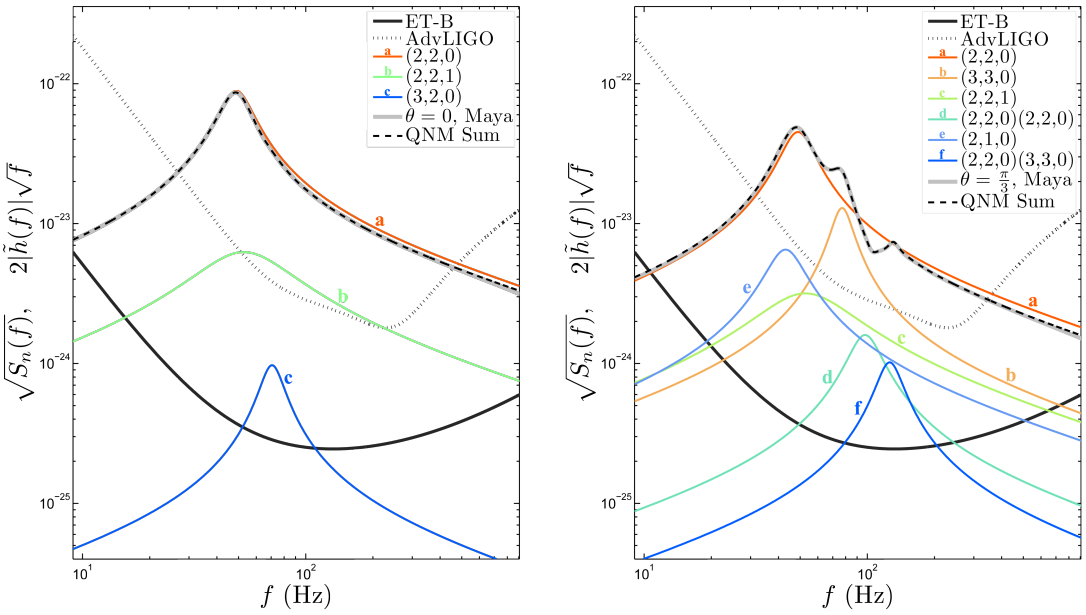

Figure 22: Frequency domain envelopes of strain and fitted QNM amplitudes for a 2:1 mass-ratio system ($\eta = 0.22$) of 350 $M_\odot$, at a distance of 100 Mpc. Left: Signal for line of sight along final spin direction (e.g. $(\theta, \phi) = (0, 0)$). Right: Line of sight $\pi/3$ *rad* with respect to final spin direction, $(\theta, \phi) = (\pi/3, 0)$. Noise curves for the Einstein Telescope and Adv. LIGO are shown for reference. For each panel, the color of each quasinormal mode curve, along with its relative position, label the mode's contribution to total signal to noise ratio. In each case, the $(l, m, n) = (2, 2, 0)$ mode is the most dominant.

In particular, Figure (21) shows the qualitative differences between the spherical multipolar gravitational wave emission predicted by Post-Newtonian (top panel), and the fundamental spheroidal emission (bottom panel) presented here. On one hand, similarities

between the $(l, m, n) = \{(2, 2, 0), (2, 1, 0)\}$ QNMs and their Post-Newtonian counterparts may suggest that they are connected by a largely linear process. On the other hand, the clear differences between Post-Newtonian predictions, and the $(l, m, n) = (3, 2, 0)$ and $(4, 4, 0)$ QNMs may suggest a region of nonlinear response between $\eta = 0.1$ and $\eta = 0.24$. Further study is needed to precisely clarify whether or not this is the case.

Despite our current limited understanding of the underlying physics, the local minima seen in Figure (21) suggest that the $(l, m, n) = (3, 2, 0)$ and $(4, 4, 0)$ QNMs are less likely to be relevant for detection in the $\sim$2:1 mass-ratio ($\eta \approx 0.22$) regime. This point, in addition to our descriptions of the overtones and second order modes (Sec. 5.4), allows us to make qualitative comments on the relevance of QNMs to template accuracy and mode detectability.

5.6.2 Template comments

While template accuracy and mode detectability are topics whose full treatment is beyond the current work, we are able to briefly comment on the impact of subdominant QNMs on the SNR of ringdown signals. To do so, we will reconsider the 2:1 mass-ratio binary discussed in the introduction (Figure (10)).

Specifically, let us contemplate an idealized scenario where a ringdown-only template is being used to search for a potential signal as observed by either the Einstein Telescope (ET), or Adv. LIGO. For simplicity we will assume that either detector is equally sensitive over the solid angle, and that there are no glitches in detector sensitivities as presented in Refs. [21, 20]. To completely constrain our example, we will consider only templates made with binary parameters identical to that of the signal: final mass 350 $M_{\odot}$, at a distance of 100 Mpc, initially nonspinning, $\eta = 0.22$, and quasicircular. We are only interested in the effect of subdominant QNMs on the estimated SNR.

If the signal, $\tilde{s}(f)$, is the frequency domain counterpart of Figure (10)'s waveform, and the template, $\tilde{h}(f)$, is composed of some superposition of QNMs according to the Fourier

transform of Equation (81), then the SNR is given by

$$\rho \;=\; \frac{(\tilde{s}(f)|\tilde{h}(f))}{\sqrt{(\tilde{h}(f)|\tilde{h}(f))}} \tag{116}$$

where

$$(a(f)|b(f)) \;\equiv\; 2\int_{-\infty}^{\infty} \frac{a^*(f)\,b(f)}{S_n(f)}\mathrm{d}f \tag{117}$$

and S_n is the power spectral density (PSD) of the detected noise [123, 21, 20].

In the best case scenario, where the signal and template are identical, ρ takes on its maximal value, ρ_{max}. Table 2 lists the values of ρ_{max} for the orientations shown in Figure (10).

Table 2: Maximal SNR values, ρ_{max}, for ET and Advanced LIGO (Adv. LIGO) detectors at two different orientations with respect to the final black hole's spin direction: $(\theta, \phi) = \{(0,0), (\pi/3, 0)\}$. Final mass 350 $M_\odot$, distance 100 Mpc, initially nonspinning, $\eta = 0.\overline{22}$, quasicircular.

(θ, ϕ)	ρ_{max}	
	Adv. LIGO	ET
$(0, 0)$	10.58	160.79
$(\pi/3, 0)$	6.20	94.29

We now ask which QNMs contribute the most to the total SNR for each of the cases above. To answer this question, we sequentially determine which N-mode template recovers the largest percent of ρ_{max}. For example, if we denote the recovered SNR of each N-mode template to be ρ_*, then in the case of Adv. LIGO, the 1-mode template that recovers the largest percentage of ρ_{max} contains only the $(l, m, n) = (2, 2, 0)$ QNM. This is the case for $\theta = 0$, where $\rho_* = 0.9986\rho_{max}$, and for $\theta = \pi/3$, where $\rho_* = 0.9749\rho_{max}$. If we ask which additional QNM results in the largest ρ_* at $\theta = \pi/3$, then $(3, 3, 0)$ proves to be the next most important, with $\rho_* = 0.9837\rho_{max}$. Taking another step forward, we find that the

best 3-mode template for Adv. LIGO at $\theta = \pi/3$ includes the $(2,2,0)$, $(3,3,0)$ and $(2,2,1)$ QNMs, with an SNR of $\rho_* = 0.9902\rho_{max}$.

Table 3: Recovered QNMs and estimated fractional SNR values for Advanced LIGO (Adv. LIGO) and the Einstein Telescope. Under each detector heading, values for the SNR found using only one mode, ρ_1, and values for using many modes, ρ_*, are shown. In the case of ρ_*, the number of QNMs used in the template increases from top to bottom. This may be seen in the first row of each case, where $\rho_* = \rho_1$.

(θ, ϕ)	Mode	Adv. LIGO		ET	
	(l, m, n)	ρ_1 (%)	ρ_* (%)	ρ_1 (%)	ρ_* (%)
$(0, 0)$	$(2,2,0)$	99.865	99.865	99.880	99.880
	$(2,2,1)$	89.461	99.986	86.956	99.989
	$(3,2,0)$	62.561	99.997	59.026	99.998
$(\frac{\pi}{3}, 0)$	$(2,2,0)$	97.494	97.494	98.348	98.348
	$(3,3,0)$	63.946	98.365	60.932	98.801
	$(2,2,1)$	86.457	99.023	85.537	99.349
	$(2,1,0)$	41.464	99.558	92.670	99.685
	$(2,2,0)(2,2,0)$	92.069	99.795	40.896	99.886
	$(2,2,0)(3,3,0)$	30.870	99.934	27.192	99.957

Table 3 lists the percentages of ρ_{max} recovered up to the 6-mode template for $\theta = \pi/3$ and up to the 3-mode template for $\theta = 0$. Figure 22 is a graphical representation of Table 3, and displays each frequency domain QNM against the ET and Adv. LIGO PSDs.

This simple numerical experiment suggests that the greater the angle between the detector's line of sight and the black hole's final spin direction, the more QNM information is needed to model the signal up to 99% of ρ_{max}. While the orientation dependence and impact of multipoles with $l > 2$ on detectability is a topic of active interest [118, 124, 125],

and previous studies of adding fundamental QNMs of $\ell > 2$ to ringdown-only templates have suggested a significant effect on event loss [93, 91], our example demonstrates that the $(l, m, n) = (2, 2, 1)$ overtone may play a meaningful role. Further study, similar to [93], is needed to better quantify its significance.

Intriguingly, although Table 3 shows that the second order QNMs may only add a minuscule amount to the total SNR, their contribution to the frequency domain features in Figure (22) raises the possibility of their being identified postdetection.

Finally, in light of the QNM amplitude and phase results presented in Sec. 5.3.2, our toy example also allows us to consider what information about the remnant black hole may be learned. It is well known that the scaling of QNM frequencies with remnant mass means that the detection of at least two QNM frequencies is required to estimate the final mass and spin of the system [90, 93, 89, 98, 126]. This information, along with the relative amplitudes may also yield information about the initial binary, and perhaps even final spin orientation [9, 98]. Of the current study, if two QNM frequencies are detected, allowing for the identification of each frequency's (l, m, n), then a rearrangement of Equation (109) suggests that information about the recoil angle relative to the line of sight may also be estimated via

$$\phi_{kick} \approx \frac{\phi_{220}}{2} - \phi_0 \, . \tag{118}$$

The applicability of this potential measure is the subject of a future study.

5.7 Conclusion

Our in-depth analysis of Numerical Relativity entrance into ringdown has provided us with a wealth of information about the excitation of QNMs. We have found evidence for nonfundamental spheroidal QNM excitations within the residuals of single-mode QNM fits (Sec. 5.2.2). By developing a method to estimate these spheroidal components (Sec. 5.3.1), we have presented a review of QNM excitations including and beyond the fundamentals, and we have discovered that the phase of these excitations is affected by the remnant black hole's final kick direction (Sec. 5.4.1).

QNM excitations are well modeled by a Post-Newtonian-like expansion (Sec. 5.4), and that our estimates for the excitation amplitudes are largely consistent with perturbation theory, within the limits of knowledge and numerical accuracy available at the time of this study (Sec. 5.5).

To make our results available for the construction of ringdown related gravitational wave templates, we have tabulated related fitting coefficients in Appendix A.

We studied the relevance of our results for gravitational wave detection with the ringdown of a 2:1 mass-ratio system of initially nonspinning black holes. For this case, we find that the $l = m = 2$, $n = 1$ overtone is the most dominant, and that that it is the second most significant QNM when the remnant black hole is observed along its final spin axis (Figure (22) left panel). This case also demonstrates that the apparent $l = m = 2$ second mode, while minuscule in comparison to its first counterpart, may be more significant than higher l QNMs at similar frequencies (Figure (22) right panel). Moreover, this case is consistent with the expectation that as the line of sight deviates from the final black hole spin direction, more QNMs are needed to accurately represent the signal (Table 3).

But as informative as our example 2:1 mass-ratio system may be, its shortcoming are clear. It demonstrates that when modeling ringdown the $(l, m, n) = (2, 2, 1)$ can play a role comparable to that of the higher fundamental QNMs (Table 3), but to solidify this statement, and it's relevance to high mass templates, a full orientation study is needed. We have also seen that apparent second order QNMs might contribute to ringdown's frequency domain features (Figure (22)), but the full extent to which these modes are relevant cannot be assessed without more accurate Numerical Relativity simulation, and a better understanding of the second order structure of Kerr perturbations. Intriguingly, we have also seen that QNM phase carries information of how the remnant black hole is oriented relative to its recoil velocity. While our example system demonstrates that this might allow for an estimation of the recoil direction relative to the line of sight, the scope of the estimation as presented here is only a first step. We look forward to the exploration of this possibility in future work.

Chapter VI

VERY BRIEFLY ON THE NEED FOR PRECESSING GRAVITATIONAL WAVE TEMPLATES

While preponderance of binary black hole Numerical Relativity work has focused on the relatively simple nonprecessing cases, nature has no intrinsic bias towards these systems [127]. Instead, although population estimates are rather uncertain, there is reason to expect precessing binary black hole systems in future detection scenarios [18, 127, 128, 19, 20]. In this chapter we very briefly describe a previously-unknown "precession" of the peak emission direction with time, both before and after the merger, about the total angular momentum direction. We demonstrate the gravitational wave polarization encodes the orientation of this direction to the line of sight. And we present contribute evidence that non-precessing templates are insufficient to extract precessing gravitational wave signals from noise using matched filtering. These results highlight the need for accurate models of precessing gravitational wave signals from compact object coalescence. This work was contributed to reference [129].

6.1 Precession During Merger

Here we describe the tenuous configuration of precessing systems. Specifically, for two gravitationally bound compact objects (*e.g.* binary black holes), with spins $\{\vec{S}_1, \vec{S}_2\}$ and angular momentum vectors $\{\vec{L}_1, \vec{L}_2\}$, it is possible for the orientation of any of these axes of ration to change in time. In particular, if $\vec{S}_1$ is not parallel with $\vec{S}_2$ *or* $\vec{S}_1 + \vec{S}_2$ is not parallel with $\vec{L}_1 + \vec{L}_2$, then the system will experience precession, where the direction of $\vec{S}_1$ and $\vec{S}_2$ vary with time *and* the orbital plane wobbles throughout the evolution of the system. Broadly put, the effect of precession on gravitational wave morphology is to modulate the gravitational wave amplitude and frequencies, thus posing a significant increase in signal complexity [129]. However, there have been proposed effective means by which we may "look

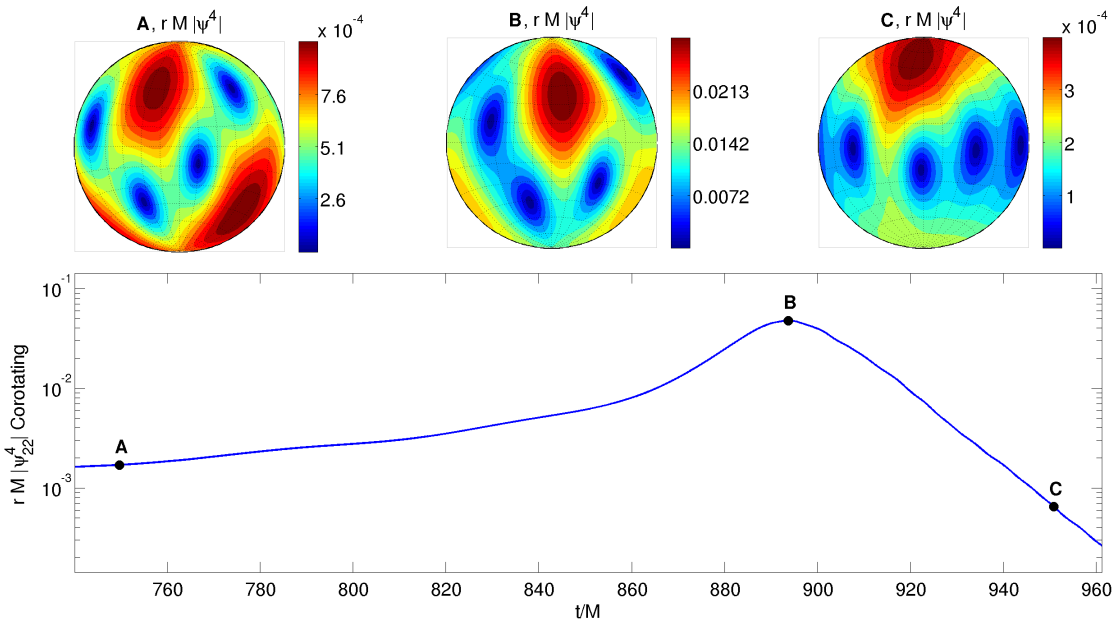

Figure 23: Three snapshots of $|\psi_4|$ (top panel) for a $m_1/m_2 = 4$, $|\vec{S}_1/{m_1}^2| = |\vec{S}_2/{m_2}^2 = 0.6|$,where the angle between $\vec{S}_1$ and $\vec{S}_2$ is $\pi/2$, bracketing the time of peak amplitude and demonstrating that the polarization content changes significantly during the merger event. For aesthetic reasons, we only show the contributions from all $l = 2$ modes. The top panels show the relative scale, with red indicating the largest $|\psi_4|$ at that time. For comparison, the bottom panel panel illustrates when these snapshots occur, using a plot of $|\psi_{22}|$ versus time.

at" precessing systems in a way that makes them appear to be, as much as possible, non-precessing [130, 131, 129, 123]. In effect, this is accomplished by defining the decomposition frame's z-direction to always be along the direction of peak gravitational wave emission. This is the so-called "co-rotating frame" (See Appendix (D), and reference [131] for a full discussion). For example, the top three panels of Figure (23) display the magnitude of ψ_4 over the solid angle. In the case of nonprecessing system, the red regions would always be localized at the north and south poles; however, in precession, these regions drift with time. The Bottom panel demonstrates that, upon choosing the co-rotating a frame, the magnitude of ψ_{22} looks qualitatively like a nonprecessing waveform (e.g. 7), and tracks the peak emission region. In this sense, the primary appeal of this so called co-rotating frame is that it simplifies the morphology of the gravitational wave emission, and therefore make modeling easier. That is, the original problem's complexity is compartmentalized: one now

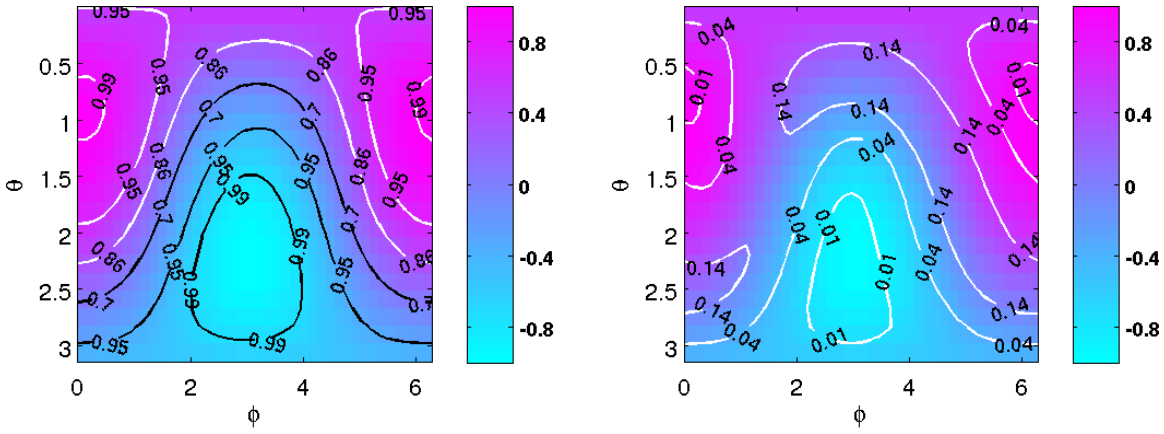

Figure 24: Nonprecessing approximation omits signal power: Comparison of corotating $(2, \pm 2)$ subspace with the sum of all $l = 2$ modes along each line of sight, for the same simulation used previously simulation and $M = 100 M_{\odot}$. Top left panel:Contours of normalized matches $|(R, \hat{\psi}_R)|$ (white) and $|(L, \hat{\psi}_L)|$ (black) for the initial LIGO noise curve at 100Mpc. For comparison, the colors indicate proximity to the direction of peak emission near merger. Top right panel: Contour plot shows the fraction of SNR lost in a nonprecessing approximation. In directions nearly perpendicular to the preferred direction, a nonprecessing approximation fails to capture all available signal information.

has to model the co-rotating frame waveform, as well as the spatial rotations needed to represent how the physical waveform would appear in any frame.

6.2 Effect on Signal Detectability

One motivation for the systematic modeling of precessing systems is the high likelihood that nonprecessing templates are not sufficiently like their precessing counterparts to allow optimal extraction of gravitational wave signals from noise. This point may be illustrated by comparing match estimates for a mock precessing template (*i.e.* a Numerical Relativity simulation in the co-rotating frame) with its non co-rotating frame counterpart. The result is displayed in Figure (24). Specifically, in the left panel, we imagine that one is able to model the co-rotating frame waveform, then apply the appropriate non corotating rotations to the model, then use the model as a gravitational wave template that accounts for precessing morphology. This yields very high matches for all lines of sight. In contrast, as shown in Figure (24)'s right panel, the using a nonprecessing template causes significant (greater than 3%) losses in the signal's fractional SNR, thus signaling a decrease in detection rate.

6.3 Chapter Summary

These, as well as other results [128, 123] accentuate the practical need for effective precessing gravitational wave models. However, at the level of Numerical Relativity, one limiting factor is our inability to place simulation in a way that guarantees sufficient coverage of all interesting regions of parameter space. In this context, a significant portion of the author's current and future work is directed towards the placement and modeling of precessing binary black hole systems.

Chapter VII

MODELING VIA UNSUPERVISED MACHINE LEARNING

While Numerical Relativity codes can simulate astrophysical systems across a highly dimensional space of initial parameters, the high computational cost of each simulation means that simulation placement within initial parameter space must be chosen with care. Here we outline a machine learning approach for simulation placement with the aim of optimizing waveform modeling while minimizing the necessary number of new Numerical Relativity simulations. The procedure presented here has no dependency on analytic or effective one body models that are tuned to numerical relativity and therefore incur some of is limitations. For example, Effective One Body (EOB) effectiveness is know to diminish in regions of increasingly unequal mass ratios where Numerical Relativity simulations are sparse [54]. Here, principle component analysis is used to build accurate waveform models directly from Numerical Relativity waveforms without the use of an intermediate model. While an example is presented for the placement of initially nonspinning binary black holes in mass ratio space, the principle of the procedure is applicable to the simulation placement and related modeling of *all* gravitational waveforms from astrophysical sources.

7.1 Motivations

While the graviational wave community awaits first detection, our ability to detect and learn from gravitational wave signals hinges on our understanding of gravitational wave morphology across a highly dimensional space of system parameters. In the case of binary black hole systems, with their 14 dimensional parameter space, the majority of computational focus to date has been on the subset of this parameter space that corresponds to nonprecessing binary black hole systems. However, as nature has no *a prior* bias to nonprecessing binary systems, there is an ongoing need to efficiently and systematically generate precessing waveforms with the aim of informing detection and modeling efforts.

More broadly, while this work focuses on binary black hole systems simulated in Numerical Relativity, there are similar needs in regards to binary neutron star and black hole neutron star systems.

Concurrently, the astrophysics community seeks effective models for observables associated with these systems. While, in general, it may not be possible to analytically model every signal of interest, the utility of accurate models that can be quickly evaluated remains of general interest. For the special cases of nonspinning, and spin aligned binary black hole systems (both nonprecessing), analytic and semi-analytic phenomenological models such as PhenB and EOB currently prevail [62, 56, 57]. However, the complexity of precessing systems has thus far balked a fully robust model for the related gravitational waveforms [130]. Therefore a strategy for the simulation evaluation and modeling of the related gravitational waveforms is of significant practical interest[1].

7.2 Literature Review

Recently, there has been notable effort to develop semi-analytic *reduced order model (ROM)* waveform models based upon basis representations of waveform time series: $h(t) = \sum_{k=0}^{k_{\rm max}} \mu_k \, \hat{e}_k(t)$. Here, $h(t)$ is the observable gravitational wave strain. The coefficients μ_k are conceived to smoothly map to initial binary parameters, and can typically be modeled with polynomial functions. The basis vectors, $\hat{e}_k(t)$, are orthogonal with respect to the inner product $\langle \hat{e}_j, \hat{e}_k \rangle = \int_{-\infty}^{\infty} \hat{e}_j^*(t) \, \hat{e}_k(t) \, {\rm d}t = \delta_{jk}$, and can be constructed in a variety of ways, including Gram-Schmidt othogonalization and Singular Value Decomposition (SVD) (or equivalently. principle component analysis (PCA)). For a smooth and continuous initial parameter space, $\mathbf{\Lambda}$, the model is defined by knowing both the basis vector, $\hat{e}_k$, as well as its coefficient, $\mu_k(\boldsymbol{\lambda})$, where $\boldsymbol{\lambda} \in \mathbf{\Lambda}$. The model is considered *reduced* as the summation terminates at some finite $k_{max} = N$ that is typically less than the number of input waveforms used to construct the set of basis vectors.

While each basis vector $\hat{e}_k(t)$ may, in principle, be developed directly from the results

[1] It is actually one of the author's primary tasks in his upcoming post-doctoral position at Cardiff University.

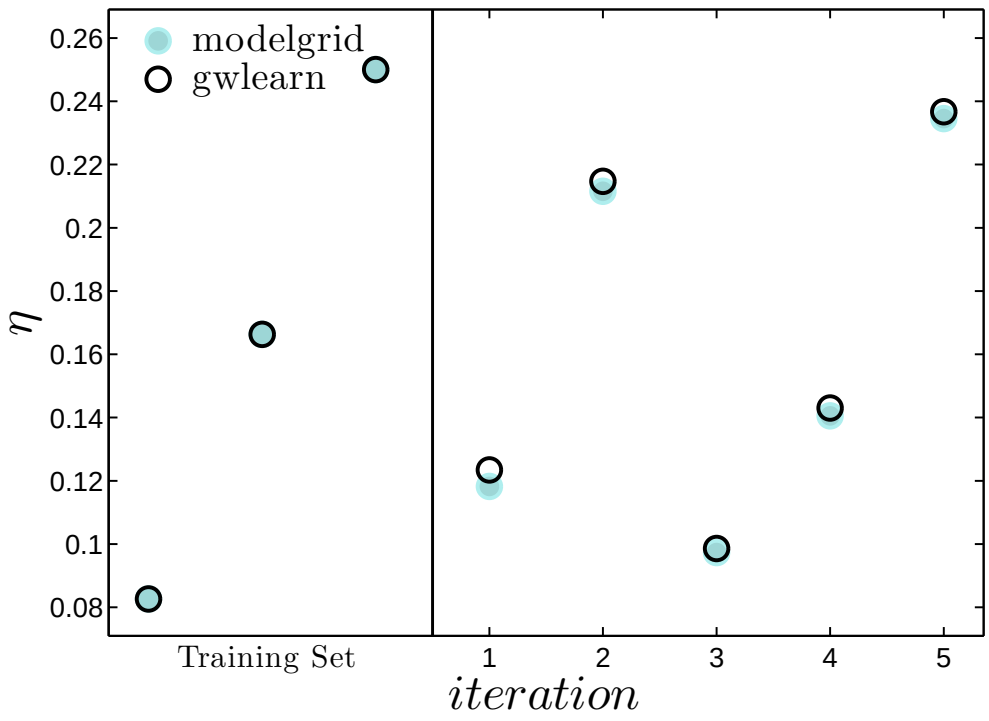

Figure 25: A comparison of the mass ratio parameters selected by this work's adaptive regression algorithm *gwlearn*, and those parameters selected by the reduced basis method, *modelgrid*, each starting with the same training set, and model tolerance.

of Numerical Relativity simulation, via methods such as gram-schmidt, or SVD, exorbitant computation costs have mostly limited ROMs to utilizing phenomenological waveform models in place of Numerical Relativity waveforms.

A recent exception is the work of Blackman *et al.* [68], which uses graham-schmidt orthogonalization to calculate $\hat{e}_k(t)$ directly from a small set Numerical Relativity waveforms (nonspinning, variable mass ratio). However, the placement of Numerical Relativity waveforms used was first informed by many evaluations an EOB model.

Specifically, to determine which Numerical Relativity simulations should be evaluated, a waveform of arbitrary mass ratio was chosen as the first basis vector $\hat{e}_1 = h_1(t)/||h_1(t)||$, and subsequent basis vectors where chosen to maximize $||h_{k+1} - P_k(h_{k+1})||$, where $P_k(h_{k+1}) = \sum_{j=1}^{k} \langle \hat{e}_j, h_{k+1} \rangle \, \hat{e}_j$, and the set $\{\hat{e}_j\}_{j=1}^{k}$ is calculated via a Gram-Schmidt procedure [73]. To perform the maximization, an EOB model served as an efficient stand-in for the computationally prohibitive Numerical Relativity waveforms.

While this approach allows for the effective prediction of where to run Numerical Relativity simulations in order to create an effective waveform model, it is still underpinned by an intermediate model developed from prior Numerical Relativity simulations.

In this work, we present an unsupervised learning approach to gravitational wave modeling that uses *adaptive regression* to develop models directly from Numerical Relativity simulations with no prior input from an intermediate waveform model.

7.3 Adaptive Regression

We consider the case were a small set of full Numerical Relativity simulations, $\{h_k\}_{k=1}^n$, can be computed across the parameter range of interest, $\{\boldsymbol{\lambda}_k\}_{k=1}^n$. Starting with this sparse *training set*, a PCA model may be constructed, and iteratively used to predict desired placement of new Numerical Relativity simulations in the manner of the reduced basis method [73]:

1. Generate an affordable catalog, C_1, of Numerical Relativity waveforms that ranges the parameter domain, $\{\vec{\mu}\}$, of interest:

   $$\mathrm{C}_1 = \{h_1, h_2, ...h_n\} \ .$$

   In the example that follows, the original catalog contains only three Numerical Relativity waveforms.

2. Perform PCA on the catalog to obtain the principle components, p_k.

3. Construct an intermediate waveform model, $\mathcal{M}_1$, using the principle components as basis vectors, $h_k = p_k$.

4. Determine the number of principle components needed to account for the desired percentage of the variance within the current catalog: N. The corresponding principle component, h_N, will be referred to as the *critical principle component*.

5. Use this intermediate model to finely evaluate the coordinate values, c_N. In this step, more waveforms are generated from the intermediate model than were used in the initial catalog.

6. Estimate whether the points in the current catalog sufficiently populate the regions in parameter space where c_N has large curvature. These are the locations in initial parameter space where more waveforms are needed to resolve the features in c_N. If c_N is determined to be poorly resolved with the current waveform catalog C_1, find the single additional point in parameter space that yields the largest decrease in the interpolation of c_N: $\vec{\mu}_1$. Otherwise, stop.

7. Generate a Numerical Relativity simulation at $\vec{\mu}_1$, and add this simulation to the catalog: $\mathrm{C}_2 = \mathrm{C}_1 \bigcup h(\vec{\mu}_1)$.

8. Return to step #2.

7.4 Discussion on a First Test Case: the Gravitational Waves of NonSpinning Binary Black Hole Systems

To test the above algorithm, we consider the placement and modeling of nonspinning binary black hole systems with variable mass ratio. As only mass ratio is changing between simulations, this is a 1-dimensional parameter space. Moreover, in place of running new simulations, a we use a reduced order PCA model that has been verified to be accurate between mass ratios of 1:1 and 1:15. Specifically, the model has been verified to accurately represent the training space (12 waveforms) as well many simulations outside of the training space (46 waveforms). With this tool in hand, we apply 7.3 to an initial training set consisting of only 3 waveforms. Here, we briefly describe our initial results.

Figure (25) displays the results of the test case. The waveform locations are plotted on the y-axis using the symmetric mass ratio $\eta = m_1 m_2/(m_1 + m_2)^2$. This plotting choice is motivated by *eta*'s known role as a nearly optimal variable for mass-ratio. This knowledge is consistent with the result of our algorithm: when choosing η as a modeling variable, simulations should be placed according to simple bisection in order to yield a ROM that is the most effective over the continuous parameter range of interest. Here in lies a subtle, but important point: the algorithm, having no inherent information about the optimality of η was capable of extracting that information from the waveforms. This is an instance

of optimal variable deduction [72]. Moreover, in proceeding from iteration 1 to iteration 5, the ability of the model to present the entire parameter space increased exponentially, such that upon termination, only 0.01% of the variance within the given parameter range was not accounted for. Unfortunately, it is beyond the constraints of the current document to expand upon this, and other aspects of our test case. However, author looks forward to rigorously vetting and expanding upon the given results.

Chapter VIII

CONCLUDING REMARKS

This brief thesis catalogs the author's current and humble contributions to gravitational wave science. In Part (I), we reviewed the foundations of General Relativity, and paid particular focus to the development of gravitational wave theory by incrementally discussing the inspiral, merger and ringdown phases of binary black hole coalescence. In Part (II), we connected our almost entirely theory based discussion with ongoing experimental efforts to detect gravitational wave from compact object coalescence. Particular attention was given to matched-filtering, and its central roll in motivating gravitational wave modeling. A similar amount of focus was placed on a formal definition of modeling, and examples were given of representative modeling and linear regression modeling.

Subsequently, in Part (III), the cumulative information of the preceding chapters was utilized to present this thesis' core results. In Chapter (5), it was demonstrated that by interfacing Numerical Relativity, black hole perturbation theory, representative modeling, and linear modeling, new information about the final moments of binary black hole merger may be learned: overtones, possible nonlinear modes, and a possible new observable – the black hole recoil direction. While these results are limited to nonspinning (nonprecessing) binary black hole systems, in Chapter (6), we motivated the need for models of precessing gravitational wave signals by discussing what will likely be a central modeling tool (the co-rotating frame), and its promise for increasing the detection rate of astrophysical precessing systems. Lastly, in Chapter (7) we discussed the author's ongoing work aimed at simultaneously addressing simulation placement and gravitational wave modeling. Currently, is it one of the authors immediate goals to refine this work, and apply it to the modeling of precessing gravitational waveforms.

In closing, the author would like to communicate an important aspect of his personal science that has supported, and at times been the sole motivation for, his progress to date.

Put simply, the author find it extremely motivating, rewarding and useful to do science for fun, even if the science is not directly related to his core research. While it is not appropriate here to expand on this claim in detail, the author is confident that his willingness to cultivate peripheral interests give needed practice to solving new problems, learning new techniques, and asking relevant questions beyond the funnel of his academic community. While this quality is surely not without risk, it is also the lesson of history that so much of truly good science happens in our spare time.

Appendix A

FIT COEFFICIENTS FOR QNM EXCITATIONS

For convenience, here we have collected all fitting formulas and related coefficients. In particular, if one is interested in the QNM excitations from initially nonspinning, quasicircular binary black hole coalescence, then we present the following algorithmic description to apply the model presented in Sec. 5.4.

The primary inputs of our model are the binary's component masses, m_1 and m_2. The primary output of our model is the ringdown portion $\psi_4(t)$, starting 10 (M) after the peak luminosity in the $l = m = 2$ spherical multipole. Therefore, throughout what follows, $t = 0$ corresponds to 10 (M) after the $l = m = 2$ spherical multipole, and values of $t < 0$ are to generally be considered outside of the fit's domain of applicability.

Table 4: Magnitude of fitting coefficients for C_{lmn}.

(l, m, n)	$\|a_0\|$	$\|a_1\|$	$\|a_2\|$	$\|a_3\|$	$\|a_4\|$
$(2, 1, 0)$	0.2045	0.3554	1.034	0	0
$(2, 2, 0)$	0.184	0.1	5.088	0	0
$(2, 2, 1)$	0.8904	6.304	19.4	0	0
$(2, 2, 2)$	1.626	15.3	40.65	0	0
$(3, 2, 0)$	0.06907	0.4579	0.7754	2.476	0
$(3, 3, 0)$	0.07896	0.9093	5.345	20.66	0
$(3, 3, 1)$	0.7784	7.641	25.73	10.29	0
$(4, 3, 0)$	0.03099	0.3174	1.544	6.013	16.33
$(4, 4, 0)$	0.05596	0.7825	7.74	41.32	82.02
$(5, 4, 0)$	0.01222	0.1674	1.834	8.804	16.32
$(5, 5, 0)$	0.03257	0.4652	4.876	28.71	64.31

Table 5: Phase of C_{lmn} fitting coefficients.

(l,m,n)	α_0	α_1	α_2	α_3	α_4
$(2,1,0)$	2.417	-2.647	-2.042	0	0
$(2,2,0)$	0.05992	-2.208	0.2412	0	0
$(2,2,1)$	-2.936	0.129	2.961	0	0
$(2,2,2)$	0.2528	-2.928	0.08554	0	0
$(3,2,0)$	-0.7712	1.71	-2.036	-2.553	0
$(3,3,0)$	-0.1153	1.528	-1.131	1.747	0
$(3,3,1)$	-2.726	0.3594	-2.938	-1.683	0
$(4,3,0)$	2.285	-1.541	1.39	-1.077	1.897
$(4,4,0)$	0.008012	2.588	-0.4417	2.729	-0.5777
$(5,4,0)$	2.077	-2.134	0.1512	2.731	-0.8791
$(5,5,0)$	3.123	-0.5147	2.841	-0.1611	2.886

First, given m_1 and m_2, one may calculate the symmetric mass-ratio via

$$\eta = \frac{\mathrm{m}_1 \mathrm{m}_2}{\mathrm{m}_1 + \mathrm{m}_2} \,.$$

With the symmetric mass-ratio, one may use a phenomenological fitting formula to quickly estimate the remnant black hole's final mass, M, and dimensionless spin, $j = S/M^2$. While we present fitting formulas in Appendix C, an alternative formula may be found in [132].

Now with the final black hole's parameters at hand, individual QNM frequencies,

$$\tilde{\omega}_{lmn} = \omega_{lmn} + i/\tau_{lmn} \,,$$

may be most readily obtained by using the fitting formulas presented in [89]. Alternatively one may use the tabulated values for $M\omega_{lmn}$ available at [133].

We have that estimates for the complex QNM excitation factors, A_{lmn}, may be found by evaluating the following series of equations:

$$\delta_m(\mathrm{m}_1, \mathrm{m}_2) \equiv \frac{|\mathrm{m}_1 + (-1)^m \mathrm{m}_2|}{\mathrm{m}_1 + \mathrm{m}_2} \tag{119}$$

$$A_{lmn} = \tilde{\omega}_{nlm}^2 \, \delta_m(\mathrm{m}_1, \mathrm{m}_2) \, \eta^{1+n} \sum_{u=0} |a_u| e^{i\alpha_u} \, \eta^u \tag{120}$$

Values for $|a_u|$ are listed in Table 4. Values for α_u are listed in Table 5.

For the second order QNMs discussed in Sec. 5.4.2, we have that

$$A_{(l_1,m_1,n_1)(l_2,m_2,n_2)} = \mu_{(l_1,m_1,n_1)(l_2,m_2,n_2)} A_{l_1,m_1,n_1} A_{l_2,m_2,n_2} \, ,$$

where for the (2,2,0)(2,2,0) mode we find that

$$\mu_{(2,2,0)(2,2,0)} = 5.3956 \, ,$$

and for the (2,2,0)(3,3,0) mode,

$$\mu_{(2,2,0)(3,3,0)} = 4.6354 \, .$$

Keeping in mind that all tabulated coefficients correspond to $T_0 = 10$ (M), the full time domain ringdown waveform may be calculated by first evaluating the spheroidal harmonics, ${}_{-2}S_{lm}(j\tilde{\omega}_{lmn}, \theta, \phi)$ (via [40]), then evaluating

$$\psi_4(t, \theta, \phi) = \frac{1}{r} \sum_{l,m,n} \psi_{lmn}^{\mathrm{PT}}(t) \, [{}_{-2}S_{lm}(j\tilde{\omega}_{lmn}, \theta, \phi)]$$

where

$$\psi_{lmn}^{\mathrm{PT}}(t) = A_{lmn} \, e^{i\tilde{\omega}_{lmn} t} \, .$$

Alternatively, one may calculate the spherical multipole moments by evaluating

$$\psi_{l'm}^{\mathrm{NR}}(t) = \sum_{n,l} A_{lmn} \, \sigma_{l'lmn} \, e^{i\tilde{\omega}_{lmn} t}$$

where

$$\sigma_{l'lmn} \equiv \int_\Omega {}_{-2}S_{lm}(j\tilde{\omega}_{lmn}, \theta, \phi) \, {}_{-2}\bar{Y}_{l'm}(\theta, \phi) \, \mathrm{d}\Omega \, .$$

While we have suppressed the second order notation for simplicity, one may again impose the notion that each full second order QNM corresponds to products of two first order modes. With the two expressions for $\psi^{\rm NR}_{l'm}(t)$ and $\psi^{\rm PT}_{lmn}(t)$ above, we have completed our algorithmic description for calculating ringdown waveforms using the initial binary's component masses.

While our discussion thus far has been limited to first and fundamental overtones, $n = 0$ and $n = 1$, it should also be noted that consistent evidence for the $n = 2$, $l = m = 2$, overtone may be readily observed by considering fitting regions closer to the $\psi^{\rm NR}_{lm}$ luminosity. Figure 26 displays this overtone scaled relative to $T_0 = 10$ (M). Though the general trend is reminiscent of the $n = 0$ and $n = 1$ overtones, the $n = 2$ mode's faster decay rate corresponds to larger variation with fitting region (e.g. larger error bars).

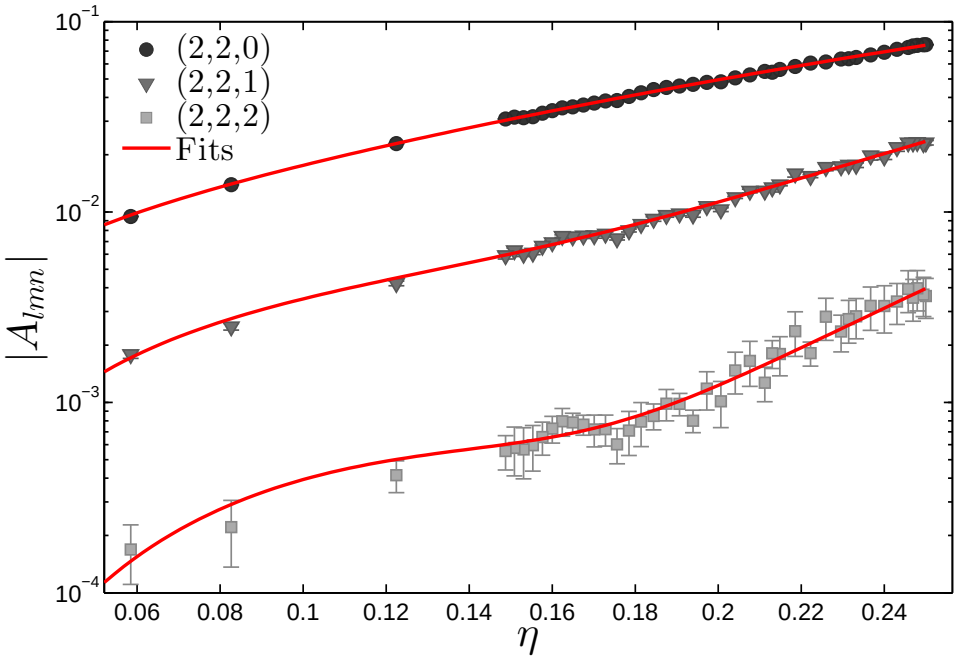

Figure 26: The $n = 0, 1$ and 2 overtones of the $l = m = 2$ QNM excitation recovered from Numerical Relativity ringdown if initially nonspinning unequal mass-ratio black hole binaries. The error bars were calculated as described in Sec. 5.3.1- f.

Appendix B

THE START OF RINGDOWN

While it is not possible to define an absolute start of ringdown, we may make a practical definition by asking which potential ringdown region is best modeled by QNMs only. This

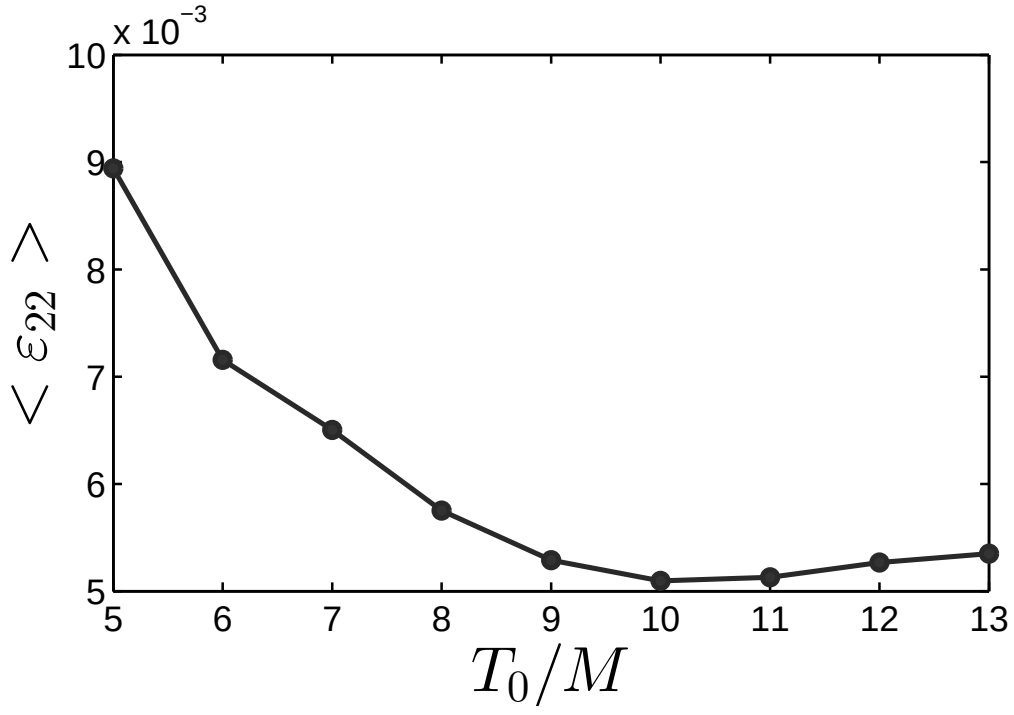

Figure 27: Mean fractional root-mean-square error (Equation (88)) for the $l = m = 2$ multipole with respect to the fitting region start time, T_0. Here the *greedy-OLS* (Sec. 5.3.1) algorithm was used to used to perform a multimode fit for each fitting region.

question may be addressed by finding a local minimum in residual error with respect to fitting region start time. To this end let us consider the multipole which is least effected by numerical errors: $\psi_{22}^{\rm NR}$. Figure 27 shows its residual error [Equation (88)] on symmetric mass-ratio. The trend observed here is inherently systematic as, when moving towards the peak in radiation, the data are no longer dominated by QNMs, while, when moving away

from the peak, numerical noise eventually dominates.

Consequently, although there is a visible minimum at $T_0 = 10\ (M)$, it is not the global minimum, as ε_{22} fluctuates in the numerical noise following $T_0 = 13\ (M)$. However, 10 (M) nevertheless gives us a practical starting point within which the majority of $\psi_{lm}^{\rm NR}$ is above the numerical noise floor.

Table 6: Fitting coefficients for $M_f(\eta)$ (Equation (122)) and $j_f(\eta)$ (Equation (121)).

	t_0	t_1	t_2	t_3	t_4	t_5
M	1	−0.046297	−0.71006	1.5028	−4.0124	−0.28448
j	0	3.4339	−3.7988	5.7733	−6.378	0

Appendix C

FINAL MASS AND SPIN

As noted in [132], the final mass and spin dependence on initial binary symmetric mass-ratio may be well fit by a polynomial in η. Alternatively, the more recent study, Ref. [88], shows that the final black hole parameters may also be well modeled as a power series in $m_1 - m_2$. Here, we present a methodologically different fit than that presented in [132] and [88], while maintaining the η parametrization of [132]. Specifically, when fitting final dimensionless spin, j_f, we choose to directly impose the boundary condition that as $\eta \to 0$, $j_f \to 0$. In particular, we fit

$$j_f(\eta) = \eta \sum_{k=1} t_k \, \eta^{k-1} \tag{121}$$

Similarly, when fitting final mass, M_f, we choose to directly impose the boundary condition that as $\eta \to 0$, $M_f \to 1$. In particular, we fit

$$M_f(\eta) = 1 - \eta \sum_{k=1} t'_k \, \eta^{k-1}. \tag{122}$$

The fitting result for $j_f(\eta)$ is shown in Figure (11). Fitting coefficients are tabulated in Table 6. While the fitting results here are consistent with [132] and [88] within their fit's domain of applicability (deviations are within 1% of the values reported), we expect that the forms given in 121 and 122 bias the fit towards the physically correct solution outside of the fitting domain.

Consistency with multimode Fit.— The numerical values used to make the above fits (Table 6) were calculated using the isolated horizon formalism [8]. However, final black hole mass and spin may also be estimated using ringdown fitting (e.g. [111, 93]). For the numerical runs considered here, we find that single mode fitting recovers the horizon estimate to within $\sim 5\%$, while multimode fitting recovers the horizon estimate to within

$\sim$ 0.5%. This level of agreement is within the numerical error of the isolated horizon estimate.

Appendix D

PRECESSING BLACK HOLE BINARIES: EXTRACTING THE COROTATING WAVEFORM

For ease of reference, the author has included a description of co-rotating frame extraction.

D.1 *Excerpt from reference [123]*:

Particularly early in the inspiral, the gravitational wave signal from merging binaries can be approximated by the emission from instantaneously nonprecessing binaries, slowly rotated with time as the orbital plane precesses. At late times, the gravitational wave signal will reflect perturbations of a single black hole with a well-identified spin axis. In both cases and in between, a well-chosen instantaneous or global frame can dramatically simplify the decomposition of $\psi_4(\hat{n},t)$ in terms of spin-weighted harmonic functions $\psi_{4l,m}(t)$. These simplifications make it easier to distinguish physically relevant from superfluous modulations; to model emission and generate hybrids; and to formulate tests of general relativity itself.

In this paper, we adopt a preferred direction $\hat{V}$ aligned with the principal axes of $\left\langle \mathcal{L}_{(a}\mathcal{L}_{b)}\right\rangle$. The tensor $\left\langle \mathcal{L}_{(a}\mathcal{L}_{b)}\right\rangle$ is defined by the following angular integral, acting on a symmetric tensor constructed from the rotation group generators $\mathcal{L}_a$ acting on the asymptotic Weyl scalar:

$$\begin{aligned} \left\langle \mathcal{L}_{(a}\mathcal{L}_{b)}\right\rangle &\equiv \frac{\int d\Omega {\psi_4}^*(t)\mathcal{L}_{(a}\mathcal{L}_{b)}\psi_4(t)}{\int d\Omega|\psi_4|^2} \\ &= \frac{\sum_{lmm'}\psi^*_{4lm'}\psi_{4lm}\left\langle lm'\left|\mathcal{L}_{(a}\mathcal{L}_{b)}\right|lm\right\rangle}{\int d\Omega|\psi_4|^2} \end{aligned} \tag{123}$$

where in the second line we expand $\psi_4 = \sum_{lm}\psi_{4lm}(t)Y^{(-2)}_{lm}(\theta,\phi)$ and perform the angular integral. The action of the rotation group generators $\mathcal{L}_a$ on basis states $|lm\rangle$ is

well-understood, allowing us to re-express the tensor $\left\langle \mathcal{L}_{(a}\mathcal{L}_{b)} \right\rangle$ as:

$$\begin{aligned} I_2 &\equiv \frac{1}{2}\left(\psi, L_+ L_+ \psi\right) \\ &= \frac{1}{2}\sum_{l,m} c_{l,m} c_{l,m+1} \psi^*_{l,m+2} \psi_{l,m} \qquad (124a) \\ I_1 &\equiv \left(\psi, L_+ (L_z + 1/2)\psi\right) \\ &= \sum_{l,m} c_{l,m}(m+1/2)\psi^*_{l,m+1}\psi_{l,m} \qquad (124b) \\ I_0 &\equiv \frac{1}{2}\left(\psi | L^2 - L_z^2 | \psi\right) \\ &= \frac{1}{2}\sum_{l,m}[l(l+1) - m^2]|\psi_{l,m}|^2 \qquad (124c) \\ I_{zz} &\equiv \left(\psi, L_z L_z \psi\right) = \sum_{l,m} m^2 |\psi_{l,m}|^2 \qquad (124d) \end{aligned}$$

where $c_{l,m} = \sqrt{l(l+1) - m(m+1)}$. In terms of these expressions, the orientation-averaged tensor is

$$\left\langle \mathcal{L}_{(a}\mathcal{L}_{b)} \right\rangle = \frac{1}{\sum_{l,m}|\psi_{l,m}|^2} \begin{bmatrix} I_0 + \mathrm{Re}(I_2) & \mathrm{Im}I_2 & \mathrm{Re}I_1 \\ & I_0 - \mathrm{Re}(I_2) & \mathrm{Im}I_1 \\ & & I_{zz} \end{bmatrix} \qquad (124e)$$

The dominant eigendirection $\hat{V}$ of this tensor specifies two of the three Euler angles needed to specify a frame:

$$\hat{V} = (\cos\alpha \sin\beta, \sin\alpha\sin\beta, \cos\beta)\ . \qquad (125)$$

To determine the remaining Euler angle (γ), we self-consistently adjoin a rotation in the plane transverse to this orientation, to account for the gradual buildup of transverse phase due to precession:

$$\gamma(t) = -\int_0^t \cos\beta \frac{d\alpha}{dt} dt \qquad (126)$$

Having specified the three Euler angles that define a new frame, we rotate the simulation-frame $Y^{(-2)}_{l,m}$ coefficients of ψ_4 to the new, time-dependent frame:

$$\begin{aligned} \psi_{4\,l,m}^{ROT} &= \sum_{\bar{m}} D^l_{m\bar{m}}(R(\alpha,\beta,\gamma)^{-1})\psi_{4 l\bar{m}} \qquad (127) \\ &= \sum_{\bar{m}} e^{i\bar{m}\gamma} d_{\bar{m}m}(\beta) e^{im\alpha}\psi_{4 l\bar{m}} \qquad (128) \end{aligned}$$

where $R(\alpha, \beta, \gamma)$ carries the $\hat{z}$ axis to $\hat{V}$, plus a rotation transverse to that direction by γ.

All simulations of the same physical system (with the same tetrad normalization) will agree on $\psi_4(t, \hat{n})$. The choice of frame at future infinity reparameterizes the same results. While our choice for the preferred frame continues to precess during and after merger, to the extent our simulations have so far resolved, some future choice for the preferred frame could conceivably converge to a fixed frame, aligned with the final total angular momentum direction $\hat{J}_f$. The choice of corotating frame depends on convention. As a result, the corotating-frame waveforms we describe below can differ from those extracted using other conventions, with differences increasing at late times. For the purposes of this paper – comparison with nonprecessing binaries, principally of the leading-order mode – we anticipate these differences are small.

REFERENCES

[1] M. Hannam, S. Husa, B. Bruegmann, and A. Gopakumar, "Comparison between numerical-relativity and post-Newtonian waveforms from spinning binaries: The Orbital hang-up case," Phys.Rev., vol. D78, p. 104007, 2008.

[2] `Maya` makes use of the openly available `Einstein Toolkit` [4], which is based on the `CACTUS` [5] code structure and `CARPET` [6] mesh refinement. Related subroutines have been generated by the `Kranc` [7] library.

[3] J. Clark, L. Cadonati, J. Healy, I. S. Heng, J. Logue, et al., "Investigating Binary Black Hole Mergers with Principal Component Analysis," Astrophys.Space Sci.Proc., vol. 40, pp. 281–287, 2015.

[4] Einstein Toolkit home page:
TThttp://www.einsteintoolkit.org.

[5] Cactus Computational Toolkit home page:TThttp://www.cactuscode.org.

[6] E. Schnetter, S. H. Hawley, and I. Hawke, "Evolutions in 3D numerical relativity using fixed mesh refinement," Class. Quant. Grav., vol. 21, pp. 1465–1488, 21 March 2004.

[7] S. Husa, I. Hinder, and C. Lechner, "Kranc: a mathematica application to generate numerical codes for tensorial evolution equations," Computer Physics Communications, vol. 174, pp. 983–1004, June 2006.

[8] J. Frauendiener, "Miguel Alcubierre: Introduction to 3 + 1 numerical relativity," Gen.Rel.Grav., vol. 43, pp. 2931–2933, 2011.

[9] I. Kamaretsos, "From black holes to their progenitors: A full population study in measuring black hole binary parameters from ringdown signals," J.Phys.Conf.Ser., vol. 363, p. 012047, 2012.

[10] J. Meidam, M. Agathos, C. Van Den Broeck, J. Veitch, and B. Sathyaprakash, "TIGER's tail: Testing the no-hair theorem with black hole ringdowns," 2014.

[11] L. Blanchet, G. Faye, B. R. Iyer, and S. Sinha, "The Third post-Newtonian gravitational wave polarisations and associated spherical harmonic modes for inspiralling compact binaries in quasi-circular orbits," Class.Quant.Grav., vol. 25, p. 165003, 2008.

[12] A. Einstein, "Approximate integration of the field equations of gravitation," Annalen Phys., vol. 49, pp. 693–696, 1916.

[13] R. O'Shaughnessy, J. Healy, L. London, Z. Meeks, and D. Shoemaker, "Is J enough? Comparison of gravitational waves emitted along the total angular momentum direction with other preferred orientations," Phys.Rev., vol. D85, no. 6, p. 084003, 2012.

[14] B. Schutz, A First Course in General Relativity. Cambridge University Press, 2nd ed., June 2009.

[15] M. Maggiore, "Gravitational waves. Volume 1: Theory and experiments," Gen.Rel.Grav., vol. 41, pp. 1667–1669, 2009.

[16] S. Carroll, Spacetime and Geometry: An Introduction to General Relativity. Benjamin Cummings, Sept. 2003.

[17] K. S. Thorne, "Gravitational radiation: A New window onto the universe," 1997.

[18] J. Abadie et al., "Predictions for the Rates of Compact Binary Coalescences Observable by Ground-based Gravitational-wave Detectors," Class.Quant.Grav., vol. 27, p. 173001, 2010.

[19] K. Belczynski, M. Dominik, T. Bulik, R. O'Shaughnessy, C. Fryer, et al., "The effect of metallicity on the detection prospects for gravitational waves," 2010.

[20] C. K. Mishra, K. Arun, B. R. Iyer, and B. Sathyaprakash, "Parametrized tests of post-Newtonian theory using Advanced LIGO and Einstein Telescope," Phys.Rev., vol. D82, p. 064010, 2010.

[21] P. Ajith and S. Bose, "Estimating the parameters of non-spinning binary black holes using ground-based gravitational-wave detectors: Statistical errors," Phys.Rev., vol. D79, p. 084032, 2009.

[22] J. Franklin, Classical Electromagnetism. Addison-Wesley, 2005.

[23] L. Blanchet, G. Faye, B. R. Iyer, and S. Sinha, "The Third post-Newtonian gravitational wave polarisations and associated spherical harmonic modes for inspiralling compact binaries in quasi-circular orbits," Class.Quant.Grav., vol. 25, p. 165003, 2008.

[24] K. S. Thorne, "Multipole expansions of gravitational radiation," Rev. Mod. Phys., vol. 52, pp. 299–339, Apr 1980.

[25] L. E. Kidder, "Using full information when computing modes of post-Newtonian waveforms from inspiralling compact binaries in circular orbit," Phys.Rev., vol. D77, p. 044016, 2008.

[26] T. Dray, "The Relationship Between Monopole Harmonics and Spin Weighted Spherical Harmonics," J.Math.Phys., vol. 26, p. 1030, 1985.

[27] L. Blanchet, "Post-Newtonian theory and the two-body problem," July 2009.

[28] J. Pullin, "Living Reviews in Relativity: Numerical Relativity," Nov. 2012.

[29] T. W. Baumgarte and S. L. Shapiro, "Numerical Relativity and Compact Binaries," Nov. 2002.

[30] P. Grandclement and J. Novak, "Spectral Methods for Numerical Relativity," ArXiv e-prints, vol. 706, June 2007.

[31] C. Bona and C. Palenzuela-Luque, Elements of Numerical Relativity: From Einstein's Equations to I Springer, 1 ed., Aug. 2005.

[32] J. M. Centrella, J. G. Baker, B. J. Kelly, and J. R. van Meter, "Black-hole binaries, gravitational waves, and numerical relativity," Oct. 2010.

[33] I. Hinder, "The current status of binary black hole simulations in numerical relativity," Classical and Quantum Gravity, vol. 27, no. 11, p. 114004, 2010.

[34] R. L. Arnowitt, S. Deser, and C. W. Misner, "The Dynamics of general relativity," Gen.Rel.Grav., vol. 40, pp. 1997–2027, 2008.

[35] M. Shibata and T. Nakamura, "Evolution of three-dimensional gravitational waves: Harmonic slicing case," Phys.Rev.D, vol. 52, pp. 5428–5444, Nov. 1995.

[36] G. Cook, "Initial Data for Numerical Relativity," Living Reviews in Relativity, vol. 3, p. 5, Dec. 2000.

[37] A. Nerozzi, "Scalar functions for wave extraction in numerical relativity," Phys.Rev.D, vol. 75, p. 104002, May 2007.

[38] M. Campanelli and C. O. Lousto, "Second order gauge invariant gravitational perturbations of a Kerr black hole," Phys.Rev., vol. D59, p. 124022, 1999.

[39] E. Newman and R. Penrose, "An Approach to gravitational radiation by a method of spin coefficients," J.Math.Phys., vol. 3, pp. 566–578, 1962.

[40] E. Leaver, "An Analytic representation for the quasi normal modes of Kerr black holes," Proc.Roy.Soc.Lond., vol. A402, pp. 285–298, 1985.

[41] C. V. Vishveshwara, "Stability of the schwarzschild metric," Phys. Rev. D, vol. 1, pp. 2870–2879, May 1970.

[42] F. Pretorius, "Evolution of binary black hole spacetimes," Phys.Rev.Lett., vol. 95, p. 121101, 2005.

[43] M. Campanelli, C. Lousto, P. Marronetti, and Y. Zlochower, "Accurate evolutions of orbiting black-hole binaries without excision," Phys.Rev.Lett., vol. 96, p. 111101, 2006.

[44] J. G. Baker, J. Centrella, D.-I. Choi, M. Koppitz, and J. van Meter, "Gravitational wave extraction from an inspiraling configuration of merging black holes," Phys.Rev.Lett., vol. 96, p. 111102, 2006.

[45] P. Ajith, M. Boyle, D. A. Brown, B. Brgmann, L. T. Buchman, et al., "The NINJA-2 catalog of hybrid post-Newtonian/numerical-relativity waveforms for non-precessing black-hole binaries," Class.Quant.Grav., vol. 29, p. 124001, 2012.

[46] M. Boyle, D. A. Brown, and L. Pekowsky, "Comparison of high-accuracy numerical simulations of black-hole binaries with stationary phase post-Newtonian template waveforms for Initial and Advanced LIGO," Class.Quant.Grav., vol. 26, p. 114006, 2009.

[47] I. Hinder, A. Buonanno, M. Boyle, Z. B. Etienne, J. Healy, et al., "Error-analysis and comparison to analytical models of numerical waveforms produced by the NRAR Collaboration," Class.Quant.Grav., vol. 31, p. 025012, 2014.

[48] S. A. Teukolsky, "Perturbations of a rotating black hole. i. fundamental equations for gravitational, electromagnetic, and neutrino-field perturbations," Astrophysical Journal, vol. 185, pp. 635–648, 1973.

[49] C. Reisswig and D. Pollney, "Notes on the integration of numerical relativity waveforms," Class.Quant.Grav., vol. 28, p. 195015, 2011.

[50] P. Ajith, S. Babak, Y. Chen, M. Hewitson, B. Krishnan, et al., "A Template bank for gravitational waveforms from coalescing binary black holes. I. Non-spinning binaries," Phys.Rev., vol. D77, p. 104017, 2008.

[51] A. Ghosh, W. Del Pozzo, and P. Ajith, "Estimating parameters of binary black holes from gravitational-wave observations of their inspiral, merger and ringdown," 2015.

[52] C. V. D. Broeck, "Gravitational wave searches with Advanced LIGO and Advanced Virgo," 2015.

[53] B. J. Owen and B. Sathyaprakash, "Matched filtering of gravitational waves from inspiraling compact binaries: Computational cost and template placement," Phys.Rev., vol. D60, p. 022002, 1999.

[54] M. Prrer, "Frequency domain reduced order models for gravitational waves from aligned-spin compact binaries," Class.Quant.Grav., vol. 31, no. 19, p. 195010, 2014.

[55] M. Kesden, D. Gerosa, R. OShaughnessy, E. Berti, and U. Sperhake, "Effective potentials and morphological transitions for binary black-hole spin precession," Phys.Rev.Lett., vol. 114, no. 8, p. 081103, 2015.

[56] T. Damour, A. Nagar, E. N. Dorband, D. Pollney, and L. Rezzolla, "Faithful Effective-One-Body waveforms of equal-mass coalescing black-hole binaries," Phys.Rev., vol. D77, p. 084017, 2008.

[57] Y. Pan, A. Buonanno, M. Boyle, L. T. Buchman, L. E. Kidder, et al., "Inspiral-merger-ringdown multipolar waveforms of nonspinning black-hole binaries using the effective-one-body formalism," Phys.Rev., vol. D84, p. 124052, 2011.

[58] M. Boyle, "Uncertainty in hybrid gravitational waveforms: Optimizing initial orbital frequencies for binary black-hole simulations," Phys.Rev., vol. D84, p. 064013, 2011.

[59] R. Sturani, S. Fischetti, L. Cadonati, G. Guidi, J. Healy, et al., "Complete phenomenological gravitational waveforms from spinning coalescing binaries," J.Phys.Conf.Ser., vol. 243, p. 012007, 2010.

[60] M. A. Scheel, M. Boyle, T. Chu, L. E. Kidder, K. D. Matthews, et al., "High-accuracy waveforms for binary black hole inspiral, merger, and ringdown," Phys.Rev., vol. D79, p. 024003, 2009.

[61] M. Boyle, A. Buonanno, L. E. Kidder, A. H. Mroue, Y. Pan, et al., "High-accuracy numerical simulation of black-hole binaries: Computation of the gravitational-wave energy flux and comparisons with post-Newtonian approximants," Phys.Rev., vol. D78, p. 104020, 2008.

[62] L. Santamaria, F. Ohme, P. Ajith, B. Bruegmann, N. Dorband, et al., "Matching post-Newtonian and numerical relativity waveforms: systematic errors and a new phenomenological model for non-precessing black hole binaries," Phys.Rev., vol. D82, p. 064016, 2010.

[63] M. Hannam, S. Husa, F. Ohme, and P. Ajith, "Length requirements for numerical-relativity waveforms," Phys.Rev., vol. D82, p. 124052, 2010.

[64] I. MacDonald, S. Nissanke, H. P. Pfeiffer, and H. P. Pfeiffer, "Suitability of post-Newtonian/numerical-relativity hybrid waveforms for gravitational wave detectors," Class.Quant.Grav., vol. 28, p. 134002, 2011.

[65] F. Ohme, M. Hannam, and S. Husa, "Reliability of complete gravitational waveform models for compact binary coalescences," Phys.Rev., vol. D84, p. 064029, 2011.

[66] J. C. Bustillo, A. Boh, S. Husa, A. M. Sintes, M. Hannam, et al., "Comparison of subdominant gravitational wave harmonics between post-Newtonian and numerical relativity calculations and construction of multi-mode hybrids," 2015.

[67] P. Canizares, S. E. Field, J. Gair, V. Raymond, R. Smith, et al., "Accelerated gravitational-wave parameter estimation with reduced order modeling," Phys.Rev.Lett., vol. 114, no. 7, p. 071104, 2015.

[68] J. Blackman, S. E. Field, C. R. Galley, B. Szilagyi, M. A. Scheel, et al., "Fast and accurate prediction of numerical relativity waveforms from binary black hole mergers using surrogate models," 2015.

[69] P. Ajith, M. Hannam, S. Husa, Y. Chen, B. Bruegmann, et al., "Inspiral-merger-ringdown waveforms for black-hole binaries with non-precessing spins," Phys.Rev.Lett., vol. 106, p. 241101, 2011.

[70] P. Ajith, S. Babak, Y. Chen, M. Hewitson, B. Krishnan, et al., "Phenomenological template family for black-hole coalescence waveforms," Class.Quant.Grav., vol. 24, pp. S689–S700, 2007.

[71] E. W. Leaver, "Solutions to a generalized spheroidal wave equation: Teukolsky's equations in general relativity, and the two-center problem in molecular quantum mechanics," vol. 27, pp. 1238–1265, May 1986.

[72] T. Hastie, R. Tibshirani, and J. Friedman, The Elements of Statistical Learning. Springer Series in Statistics, New York, NY, USA: Springer New York Inc., 2001.

[73] S. E. Field, C. R. Galley, F. Herrmann, J. S. Hesthaven, E. Ochsner, et al., "Reduced basis catalogs for gravitational wave templates," Phys.Rev.Lett., vol. 106, p. 221102, 2011.

[74] . Bjrck, "Numerics of gram-schmidt orthogonalization," Linear Algebra and its Applications, vol. 197198, no. 0, pp. 297 – 316, 1994.

[75] M. Ruiz, M. Alcubierre, D. Núñez, and R. Takahashi, "Multiple expansions for energy and momenta carried by gravitational waves," General Relativity and Gravitation, vol. 40, pp. 1705–1729, 2008.

[76] The LIGO Scientific Collaboration, the Virgo Collaboration, J. Aasi, B. P. Abbott, R. Abbott, T. Abbott, M. R. Abernathy, F. Acernese, K. Ackley, C. Adams, and et al., "Narrow-band search of continuous gravitational-wave signals from Crab and Vela pulsars in Virgo VSR4 data," ArXiv e-prints, Oct. 2014.

[77] W. H. Press and S. A. Teukolsky, "Perturbations of a rotating black hole. ii. dynamical stability of the kerr metric," Astrophysical Journal, vol. 185, pp. 649–674, 1973.

[78] E. Berti, V. Cardoso, J. A. Gonzalez, U. Sperhake, M. Hannam, S. Husa, and B. Brügmann, "Inspiral, merger, and ringdown of unequal mass black hole binaries: A multipolar analysis," Phys. Rev. D, vol. 76, p. 064034, Sep 2007.

[79] I. Kamaretsos, M. Hannam, S. Husa, and B. Sathyaprakash, "Black-hole hair loss: learning about binary progenitors from ringdown signals," Phys.Rev., vol. D85, p. 024018, 2012.

[80] A. Taracchini, A. Buonanno, Y. Pan, T. Hinderer, M. Boyle, et al., "Effective-one-body model for black-hole binaries with generic mass ratios and spins," 2013.

[81] T. Damour and A. Nagar, "An Improved analytical description of inspiralling and coalescing black-hole binaries," Phys.Rev., vol. D79, p. 081503, 2009.

[82] Y. Pan, A. Buonanno, L. T. Buchman, T. Chu, L. E. Kidder, et al., "Effective-one-body waveforms calibrated to numerical relativity simulations: coalescence of non-precessing, spinning, equal-mass black holes," Phys.Rev., vol. D81, p. 084041, 2010.

[83] B. J. Kelly and J. G. Baker, "Decoding mode mixing in black-hole merger ringdown," Phys.Rev., vol. D87, p. 084004, 2013.

[84] E. N. Dorband, E. Berti, P. Diener, E. Schnetter, and M. Tiglio, "A Numerical study of the quasinormal mode excitation of Kerr black holes," Phys.Rev., vol. D74, p. 084028, 2006.

[85] S. Okuzumi, K. Ioka, and M.-a. Sakagami, "Possible Discovery of Nonlinear Tail and Quasinormal Modes in Black Hole Ringdown," Phys.Rev., vol. D77, p. 124018, 2008.

[86] J. D. Schnittman, A. Buonanno, J. R. van Meter, J. G. Baker, W. D. Boggs, et al., "Anatomy of the binary black hole recoil: A multipolar analysis," Phys.Rev., vol. D77, p. 044031, 2008.

[87] A. Buonanno, G. B. Cook, and F. Pretorius, "Inspiral, merger and ring-down of equal-mass black-hole binaries," Phys.Rev., vol. D75, p. 124018, 2007.

[88] J. Healy, C. O. Lousto, and Y. Zlochower, "Remnant mass, spin, and recoil from spin aligned black-hole binaries," 2014.

[89] E. Berti, V. Cardoso, and C. M. Will, "On gravitational-wave spectroscopy of massive black holes with the space interferometer LISA," Phys.Rev., vol. D73, p. 064030, 2006.

[90] E. Berti, V. Cardoso, and A. O. Starinets, "Quasinormal modes of black holes and black branes," Class.Quant.Grav., vol. 26, p. 163001, 2009.

[91] S. Caudill, S. E. Field, C. R. Galley, F. Herrmann, and M. Tiglio, "Reduced Basis representations of multi-mode black hole ringdown gravitational waves," Class.Quant.Grav., vol. 29, p. 095016, 2012.

[92] K. D. Kokkotas and B. G. Schmidt, "Quasi-normal modes of stars and black holes," Living Review in Relativity, vol. 2, 1999.

[93] E. Berti, J. Cardoso, V. Cardoso, and M. Cavaglia, "Matched-filtering and parameter estimation of ringdown waveforms," Phys.Rev.D, vol. 76, p. 104044, 2007.

[94] H. Nakano and K. Ioka, "Second Order Quasi-Normal Mode of the Schwarzschild Black Hole," Phys.Rev., vol. D76, p. 084007, 2007.

[95] K. Ioka and H. Nakano, "Second and higher-order quasi-normal modes in binary black hole mergers," Phys.Rev., vol. D76, p. 061503, 2007.

[96] E. Pazos, D. Brizuela, J. M. Martin-Garcia, and M. Tiglio, "Mode coupling of Schwarzschild perturbations: Ringdown frequencies," Phys.Rev., vol. D82, p. 104028, 2010.

[97] Y. Zlochower, R. Gomez, S. Husa, L. Lehner, and J. Winicour, "Mode coupling in the nonlinear response of black holes," Phys.Rev., vol. D68, p. 084014, 2003.

[98] I. Kamaretsos, M. Hannam, and B. Sathyaprakash, "Is black-hole ringdown a memory of its progenitor?," Phys.Rev.Lett., vol. 109, p. 141102, 2012.

[99] E. W. Leaver, "Spectral decomposition of the perturbation response of the Schwarzschild geometry," Phys.Rev., vol. D34, pp. 384–408, 1986.

[100] E. Berti, V. Cardoso, and M. Casals, "Eigenvalues and eigenfunctions of spin-weighted spheroidal harmonics in four and higher dimensions," Phys. Rev. D, vol. 73, p. 024013, Jan 2006.

[101] Z. Zhang, E. Berti, and V. Cardoso, "Quasinormal ringing of Kerr black holes. II. Excitation by particles falling radially with arbitrary energy," 2013.

[102] R. H. Price, "Nonspherical Perturbations of Relativistic Gravitational Collapse. II. Integer-Spin, Zero-Rest-Mass Fields," Phys.Rev., vol. D5, pp. 2439–2454, 1972.

[103] W. Krivan, P. Laguna, and P. Papadopoulos, "Dynamics of scalar fields in the background of rotating black holes," Phys. Rev. D, vol. 54, pp. 4728–4734, Oct 1996.

[104] S. A. Teukolsky, "Rotating black holes: Separable wave equations for gravitational and electromagnetic perturbations," Phys. Rev. Lett., vol. 29, pp. 1114–1118, Oct 1972.

[105] E. Mitsou, "Gravitational radiation from radial infall of a particle into a Schwarzschild black hole. A numerical study of the spectra, quasi-normal modes and power-law tails," Phys.Rev., vol. D83, p. 044039, 2011.

[106] M. A. Scheel, A. L. Erickcek, L. M. Burko, L. E. Kidder, H. P. Pfeiffer, et al., "3-D simulations of linearized scalar fields in Kerr space-time," Phys.Rev., vol. D69, p. 104006, 2004.

[107] E. Harms, S. Bernuzzi, and B. Brgmann, "Numerical solution of the 2+1 Teukolsky equation on a hyperboloidal and horizon penetrating foliation of Kerr and application to late-time decays," Class.Quant.Grav., vol. 30, p. 115013, 2013.

[108] J. Stewart, "Stability of Kerr's spacetime," Proc.Roy.Soc.Lond., vol. A344, pp. 65–79, 1975.

[109] E. Berti, V. Cardoso, J. A. Gonzalez, and U. Sperhake, "Mining information from binary black hole mergers: a comparison of estimation methods for complex exponentials in noise," Phys.Rev.D, vol. 75, p. 124017, 2007.

[110] E. N. Dorband, E. Berti, P. Diener, E. Schnetter, and M. Tiglio, "A numerical study of the quasinormal mode excitation of kerr black holes," Phys.Rev.D, vol. 74, no. LSU-REL-081806, p. 084028, 2006.

[111] M. Hannam, S. Husa, F. Ohme, D. Muller, and B. Bruegmann, "Simulations of black-hole binaries with unequal masses or nonprecessing spins: Accuracy, physical properties, and comparison with post-Newtonian results," Phys.Rev., vol. D82, p. 124008, 2010.

[112] J. D. Schnittman, A. Buonanno, J. R. van Meter, J. G. Baker, W. D. Boggs, J. Centrella, B. J. Kelly, and S. T. McWilliams, "Anatomy of the binary black hole recoil: A multipolar analysis," Phys.Rev.D, vol. 77, p. 044031, 2008.

[113] M. R. Osborne and G. K. Smyth, "A modified prony algorithm for exponential function fitting," SIAM Journal of Scientific Computing, vol. 16, pp. 119–138, 1995.

[114] T. H. Cormen, C. E. Leiserson, R. L. Rivest, and C. Stein, Introduction to Algorithms. The MIT Press, 2 ed., 2001.

[115] O. P. F. Piedra and J. de Oliveira, "Fermion perturbations in string theory black holes," Classical and Quantum Gravity, vol. 28, no. 8, p. 085023, 2011.

[116] G. Smyth, "http://www.statsci.org/matlab/mprony.html,"

[117] D. W. Marquardt, "An algorithm for least-squares estimation of nonlinear parameters," SIAM Journal on Applied Mathematics, vol. 11, no. 2, pp. 431–441, 1963.

[118] J. Healy, P. Laguna, L. Pekowsky, and D. Shoemaker, "Template Mode Hierarchies for Binary Black Hole Mergers," Phys.Rev., vol. D88, p. 024034, 2013.

[119] S. Foffa, "Gravitating binaries at 5PN in the post-Minkowskian approximation," 2013.

[120] E. Berti and V. Cardoso, "Quasinormal ringing of Kerr black holes. I. The Excitation factors," Phys.Rev., vol. D74, p. 104020, 2006.

[121] H.-P. Nollert and R. H. Price, "Quantifying excitations of quasinormal mode systems," J.Math.Phys., vol. 40, pp. 980–1010, 1999.

[122] A. Zimmerman, H. Yang, Z. Mark, Y. Chen, and L. Lehner, "Quasinormal Modes Beyond Kerr," 2014.

[123] L. Pekowsky, R. O'Shaughnessy, J. Healy, and D. Shoemaker, "Comparing gravitational waves from nonprecessing and precessing black hole binaries in the corotating frame," Phys.Rev., vol. D88, p. 024040, 2013.

[124] L. Pekowsky, J. Healy, D. Shoemaker, and P. Laguna, "Impact of Higher-order Modes on the Detection of Binary Black Hole Coalescences," Phys.Rev., vol. D87, p. 084008, 2013.

[125] C. Capano, Y. Pan, and A. Buonanno, "Impact of Higher Harmonics in Searching for Gravitational Waves from Non-Spinning Binary Black Holes," 2013.

[126] S. Gossan, J. Veitch, and B. Sathyaprakash, "Bayesian model selection for testing the no-hair theorem with black hole ringdowns," Phys.Rev., vol. D85, p. 124056, 2012.

[127] E. Berti, E. Barausse, V. Cardoso, L. Gualtieri, P. Pani, et al., "Testing General Relativity with Present and Future Astrophysical Observations," 2015.

[128] P. Schmidt, F. Ohme, and M. Hannam, "Towards models of gravitational waveforms from generic binaries II: Modelling precession effects with a single effective precession parameter," Phys.Rev., vol. D91, no. 2, p. 024043, 2015.

[129] R. O'Shaughnessy, L. London, J. Healy, and D. Shoemaker, "Precession during merger: Strong polarization changes are observationally accessible features of strong-field gravity during binary black hole merger," Phys.Rev., vol. D87, no. 4, p. 044038, 2013.

[130] P. Schmidt, M. Hannam, S. Husa, and P. Ajith, "Tracking the precession of compact binaries from their gravitational-wave signal," Phys.Rev., vol. D84, p. 024046, 2011.

[131] M. Boyle, R. Owen, and H. P. Pfeiffer, "A geometric approach to the precession of compact binaries," Phys.Rev., vol. D84, p. 124011, 2011.

[132] L. Rezzolla, P. Diener, E. N. Dorband, D. Pollney, C. Reisswig, et al., "The Final spin from the coalescence of aligned-spin black-hole binaries," Astrophys.J., vol. 674, pp. L29–L32, 2008.

[133] E. Berti, "http://www.phy.olemiss.edu/ berti/qnms.html,"